Politecnico di Torino

Politecnico di Torino
Master in Physics of Complex Systems
A.a. 2023/2024
Sessione di Laurea Ottobre 2024

Electric potential structure formation in the divertor region

Investigating the mechanisms governing the electric potential in the divertor region of a magnetic confinement device employing a first-principles, flux-driven turbulence code

Supervisors
Politecnico di Torino:
prof. Francesco Porcelli
Swiss Plasma Center:
prof. Paolo Ricci
Louis Stenger

Candidate
Maria Isabel Muzio

EPFL

Abstract

Modelling the exhaust power in future Tokamak reactors remains an open issue in fusion research, as the change in scale from ITER to power plants suggest that heat fluxes in the latter could exceed manageable material limits on the target plates. A potential solution to the exhaust problem is the development of so-called "alternative divertors configurations", whose aim is to widen the plasma-wetted area to reduce the heat load at the targets by altering the magnetic geometry in the divertor area. This is achieved by increasing the flux expansion (X-divertor), sometimes in combination of placing the outer strike point at a larger radial location (super-X divertor), or increasing the number of strike points. Amongst this last class of solutions there are the so-called "Snowflake" divertors, which provides a secondary X-point and thus two additional magnetic field legs along which the heat flux might be dissipated. Experimental investigation of Snowflake divertors have shown a reduction of the peak heat flux at the targets compared to conventional Single Null geometries. In particular, it has been highlighted that the change in power distribution in the former cannot be explained by the modification of the magnetic geometry alone, which suggests additional cross-field transport mechanisms are at play. Numerical investigations using the Global Braginskii Solver (GBS) code have highlighted that drift-related transport may play a significant role in determining the output power profiles, and especially found an enhanced $E \times B$-drift convective pattern around the X-point of reversed field configurations . In this thesis the GBS simulation data is used to determine which mechanisms are at play in setting the electrostatic potential (and the observed drift patterns) around the X-point, comparing it to previous models. A description of the profile along the outer divertor leg is found in terms of the density, and a scaling relation is recovered in terms of the parallel coordinate in the case of simplified density profiles.

To my grandparents, the legal, the blood, and the emotional ones, for choosing me each time.
My successes are also yours.

Contents

Contents

Introduction:
A brief overview of magnetic confinement devices

One exquisitely human ability is that of creating problems that would not be found spontaneously in nature. One such problem would be that of flight: a fish would not look at the birds and wonder what it would feel like to be able to follow them into the sky; rather, it would look for the best strategy to divert their attention in order not to be captured. Another one is that of transport: a cheetah is only interested in speed as far as capturing prey goes, but would not give any further thought to efficiency than that of its own muscles. Humans have the rather unique ability to create new needs that would not arise naturally, but become fundamental as a self-fulfilling prophecy built often on pure social structures. Along with the ability to create problems humans have the proficiency in finding solutions through imitation of nature itself: Leonardo da Vinci found inspiration for his flying machines in bird anatomy; more recently, computer scientists found the solution to the challenge of teaching artificial machines how to learn from experience in the structure of the human brain. As time went by, humans got more ambitious and the problems grew in scale; accordingly, the solutions required higher leaps of imagination. The energy problem falls within this category: the need to transition from a fossil fuel-based energy production system to renewable sources is an entirely man-made issue as not only is climate change largely understood to be anthropogenic, but the issue of energy consumption itself only concerns the human kind. In an interconnected world that requires more and more energy per capita to operate each year because of the technological advancements, the current means of production are not enough to guarantee a safe passage from fossil fuels to renewable energies which can provide for the demand of entire countries. One of the solutions humanity found to this matter was to raise its eyes to the sky and try to harness the power of the stars. That is what controlled fusion is at its core: a way to produce energy exploiting similar mechanisms to those which power celestial bodies.

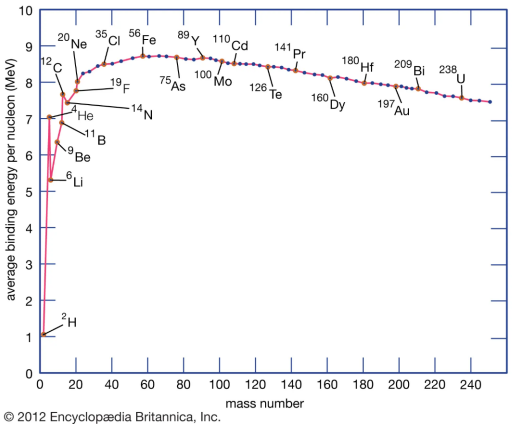

Figure 1: Nuclear binding energy
Average binding energy per nucleon, as a function of the nuclear mass number. Figure taken from Ref. [1]

The reaction that we are trying to exploit is that of *nuclear fusion*, which is a nuclear reaction that causes two light atoms to combine together to form a heavier one, where a substantial amount of energy is liberated. This energy surplus is associated to the nuclear mass defect of the product. Nuclear reactions aim to maximise nuclear binding energy (the energy required to dissociate atoms into its constituent particles, see Fig. 1), as it is associated to more stable atoms. For heavier atoms the binding energy is maximised by splitting the atom into lighter ones, which is the case for uranium in a nuclear *fission* reaction; in the case of hydrogen isotopes, such as deuterium (D) and tritium (T), the gain is obtained by fusing the lighter atoms together to obtain helium (He) instead. D-T fusion reactions have a cross-section which peaks at at approximately 100 keV, which corresponds to 1.16 billion °C [2]: at these temperatures matter is found in a state denoted as *plasma*, that is an ionised gas whose behaviour is governed by electromagnetic forces. At these temperatures, the interatomic collisions become sufficiently violent that electrons become detached from the atoms; however, the electromagnetic fields have a longer interaction range than elastic Coulomb collisions, and so plasma motion is determined not only by its local state but also by these long-range forces [3]. At macroscopic length scales, this implies that the two oppositely charged fluids, which are strongly coupled electrostatically, tend to neutralise, as a local accumulation of charge would yield huge electric fields that would be unfeasible to maintain in the presence of equal numbers of both charges [4]. Plasma is thus normally considered to be *quasi-neutral*, and exhibits *collective behaviour*, making it the perfect example of *complex system*.

It was mentioned earlier that this mean of producing energy is meant to imitate the stars: of course it is a far from trivial feat to do so, as reproducing the exact conditions of pressure and gravity that are present at the core of the Sun would be unfeasible on Earth; nevertheless, a creative solution was to employ magnetic fields to counteract this structural impediment. This is the principle on which are built magnetic confinement devices.

We are used to associating confinement with material walls, but at the temperatures mentioned before any solid container would melt, if directly in contact with the fuel (which, in turn, would recombine into the wall at the density regimes expected in these devices): that is why very strong magnetic fields are employed to confine the plasma, as charged particles would gyrate in tight helices around the magnetic field lines due to the Lorentz force. Having magnetic fields with purely open topologies (that is, which intersect the material walls), however, would lead inevitably to end losses, as the particles would still be free to move in the parallel direction (the Lorentz force has no effect along that direction): closed geometries can help in avoiding such losses. Out of the many possible topologies, the torus is the simplest closed 3D configuration allowing for the magnetic field B to

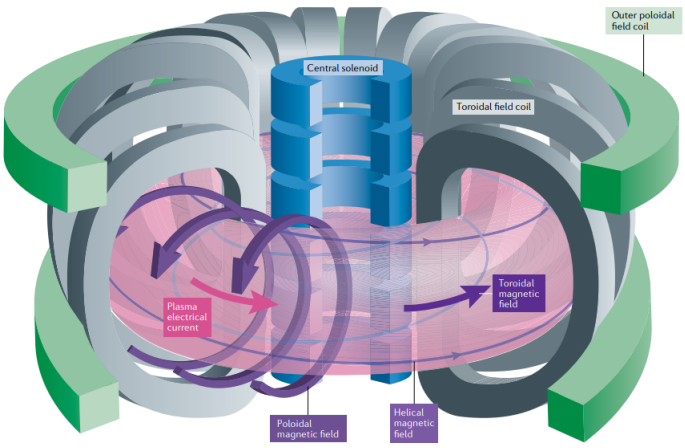

Figure 2: Tokamak
Schematic representation of a tokamak device. Figure taken from Ref. [5]

remain finite at every point (*hairy ball* theorem [6]), a fundamental characteristic as magnetic field nulls are associated with the loss of confinement. A strong toroidal field is thus required and is usually obtained through the use of coils (see Fig. 2). The toroidal component alone is however not sufficient to guarantee complete confinement, as particle drifts would arise due to the curvature of the magnetic field in two opposite directions for the oppositely charged fluids, leading to a separation of charges and the subsequent creation a vertical polarisation; this, in turn, would generate a secondary drift, the $E \times B$ drift, pointing outwards for both particle species, destroying particle confinement. This issue is resolved by generating a poloidal magnetic field, which forces the magnetic field lines to wrap around both the major and the minor axis of the torus. In the case of tokamaks, that is axisymmetric toroidal magnetic confinement devices, this is achieved through the induction of a current through the plasma, which would result in nested flux surfaces, improving plasma particle and energy confinement. To do so, a central solenoid is used and additional toroidal coils control the magnetic geometry of the magnetic field's poloidal component (Fig. 2).

The specific mention of poloidal magnetic field geometry is far from casual: one of the fundamental obstacles of the feasibility of (controlled) fusion power plants is that of the plasma exhaust. Magnetic fusion devices are open thermodynamic systems: at the steady state one expects that all the power that is injected into the system or generated within the fusion reaction has to be expelled in some way. The more fusion energy a reactor produces, the larger the power flux that will be exhausted and that could potentially damage the walls of the device [6]. The plasma exhaust problem is a delicate balance between many opposing needs: walls have to be armoured where they are in contact with plasma discharges to protect the material surfaces, but one would wish for as much non-armoured area as possible to be able to exploit the expelled neutrals to breed tritium, as the fuel is expected to be produced *in situ* [2]; the goal is to increase fusion power by maximising the plasma volume while exploiting the highest magnetic field strength achievable with conventional superconductors, but this comes at the cost of high expenses and engineering challenges.

We want to focus on one of the main solutions that is presented to this conundrum, that is the case of *diverted configurations*. The details of this solution will be illustrated later, but the key idea is that they modify the magnetic poloidal field in such a way that the heat flux is directed towards specifically armored regions called *target plates*, that are thus able to withstand the immense strain discussed earlier. The most elementary of these geometries is called *Single Null* (Fig. 3) and will be discussed at length in a separate chapter: what is important is that this configuration entails the presence of two targets. Research in the field of boundary plasma physics and divertor engineering have improved upon this elementary configuration exploiting many different mechanisms to maximise the area in order to reduce the heat load at the target plates. Amongst these there is the creation and activation of two additional targets, which would expand the plasma-wetted area efficiently: this is the so-called *Snowflake* configuration, the one we will focus on in the present thesis. *Activation* is the keyword here, as the mere existence of the new targets does not ensure that particle and heat discharges will be able to reach them, being topologically disconnected from the upstream (i.e., where the turbulent plasma exhaust is expected); however, their activation has been observed both in simulations [7] and in experiments [8], thus requires further investigation. The complex geometries in place would require for cross-field (i.e. which extends in the direction perpendicular to the magnetic flux surfaces) transport in order to make the new target plates accessible to the plasma, as they would be located in a region magnetically disconnected from it, called *Private Flux Region* (in Fig. 3 it would correspond to the region below the two "legs" which intersect the wall).

The simple dynamics that have so far been described in the general tokamak configurations are not enough to explain this type of cross-field transport of heat and particles, thus one has to look for mechanisms specific to divertors in order to explain the activation of the additional target plates. Amidst those the one that is addressed in the present thesis is that of the *convective cell*, which is theorised to be the mechanism allowing for the required cross-field transport exploiting properties of the specific magnetic geometry. It would do so by enhancing the transport associated to $E \times B$ drift

in the vicinity of the null of the poloidal component of the magnetic field, denoted as *X-point* (the point at the intersection of the white line in Fig. 3). One of the required conditions for this to be allowed is that of a specific electric potential structure formation in this region.

The present thesis focuses on this very last topic, building a theoretical description of the electric potential structure in the region of interest. It does so by starting from a general model used to describe boundary plasma dynamics, that is the *drift-reduced Braginskii equations*, comparing at each step the results to simulation data obtained using the GBS (*Global Braginskii Solver*) code, a first-principles, 3D, flux-driven, turbulence simulation code. The modelling focuses on an axisymmetric, static case for which a 2D description is sufficient, that is for which toroidally and time-averaged profiles are taken in exam. In particular, the focus will be on a specific region defined *divertor leg* (it can be thought of as the poloidal projection of the section of the magnetic flux surface associated to the poloidal magnetic field null which connects the X-point to the wall), thus the final model will be a one-dimensional description of the field of interest (which will be shown to be sufficient).

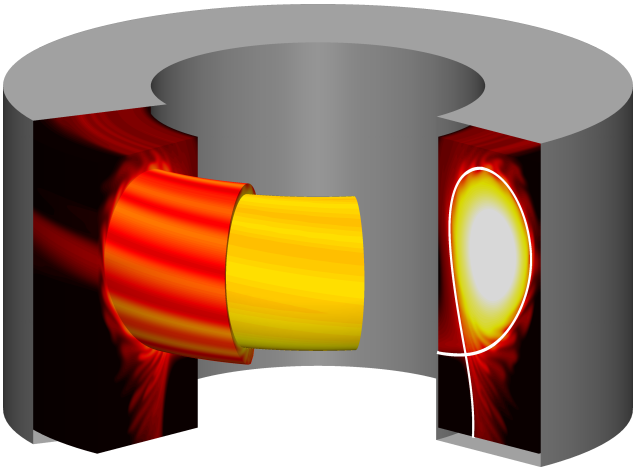

Figure 3: TCV simulation obtained using GBS code (Ref. [9]).

The discussion will be structured in the following way: the first two chapters will introduce the theoretical and numerical tools required to perform the analysis, while the following three chapters will illustrate the main results of the work. The first chapter will in particular start by going into the details of the diverted configurations mentioned above and describe the specific mechanisms which take place in the convective cell that allow for the activation of the additional targets; additionally, it will rigorously illustrate the physical model, the drift-reduced Braginskii equations, which constitute the starting point of the theory. The second chapter will then focus on the practical tools, starting by describing the GBS code employed to obtain the simulation data; it will later go on to describe the data itself and its main parameters to discuss the regime of interest; finally, it will briefly explain the main notation conventions used in the discussion, and in particular define the parametrisation of the divertor leg which will allow to account for the magnetic geometry. The third chapter will introduce the problem at hand in detail, illustrating an important previous result in the description of the electric potential along the divertor leg, which will represent a recurring comparison throughout the thesis: an initial description of the potential will be obtained through an equation setting the potential profile (generalised Ohm's law), for which the main components will be put under scrutiny to find a simplified description in terms of the fundamental observables of the system; a closure will be found for one of the components, which will allow for the equation to be rewritten in terms of electron temperature and density (and corresponding derivatives) alone. The fourth chapter will focus on the modelling of the new fields of interest, whose evolutions will be found to be intrinsically interwoven together in the region of interest. In particular an approximation will be introduced, the *refined two-point model*, which will be an evolution of a model widely used to describe profiles along the divertor

leg, that will allow to simplify the dynamics perpendicular to flux surfaces: this will let one recover a unique equation describing the required profiles. The fifth and final chapter will then collect all the approximations and the corresponding equations into a system, denoted as density-potential system, which will fully describe the potential as a function of the density. Notably, by considering simplified density profiles this will allow for the recovery of scaling laws for the potential along the divertor leg using certain approximations directly comparable to previous results found in similar regimes. The final part of the chapter is devoted to the numerical integration of the full system: at first an error estimate is defined for the simplified density profile ansatz in terms of the current model, with the possibility to build fixed-point iterative methods to describe the profiles for generalised cases; then the full system is discussed, along with the numerical instabilities that could be associated to its specific form.

Chapter 1

The physical model

The first thing to be defined is the physical model from which we will start the discussion, as it will constitute the background for most of the present thesis.

The aim of this chapter is to introduce the fundamental framework in the following way: first diverted configurations will be outlined in detail (in particular the Snowflake configuration, as our analysis will focus on this case); then the specific phenomenon we are interested in, the convective cell, will be introduced and previous results obtained for its description will briefly illustrated; lastly, the fundamental equations employed to describe the phenomena will be derived in the specific regime of interest.

1.1 The Snowflake divertor

1.1.1 Diverted configurations

One of the fundamental concepts in the discussion of the plasma exhaust problem is that of the divertor.

Given the fact that all equilibrium quantities are assumed to be axisymmetric in tokamak devices [10], one can introduce a cylindrical coordinate system describing a tokamak device (R, φ, Z), where R is the distance from the axis of symmetry of the torus, Z is the vertical coordinate, and φ is the toroidal angle. Thus the magnetic field can be decomposed in its components:

$$\mathbf{B} = B_R \mathbf{e}_R + B_Z \mathbf{e}_Z + B_\varphi \mathbf{e}_\varphi = \mathbf{B}_p + B_\varphi \mathbf{e}_\varphi$$

where $\mathbf{B}_p := \mathbf{B} = B_R \mathbf{e}_R + B_Z \mathbf{e}_Z$ is called the *poloidal magnetic field* corresponding to the specific $R-Z$ plane defining the poloidal cross-section of the plasma. The toroidal magnetic field, $\mathbf{B}_t := B_\varphi \mathbf{e}_\varphi$, is almost completely generated by the external coils. In particular one denotes as *Reversed* configurations those with a positive (in (R, φ, Z) coordinates) toroidal magnetic field at the magnetic axis and as *Forward* those with a negative B_t (Fig. 1.1).

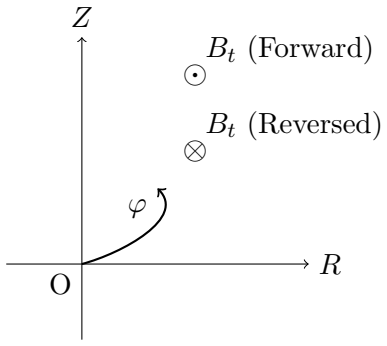

Figure 1.1: Frame of reference and toroidal magnetic field direction
The (R, φ, Z) coordinate system is schematically represented, where the tokamak axis is assumed to be to the left of the poloidal cross-section. The B_t configurations are labelled; the reversed configuration is sometimes also denoted as *unfavourable* as it is unfavourable for H-mode access (correspondingly, the forward one is labelled as *favourable*) in the case of lower Single Nulls.

The *diverted* configurations (Fig. 1.2) are those characterised by the presence of a second null in the poloidal magnetic field other than the magnetic axis, which partitions the domain into two magnetically separated regions: one in which magnetic flux surfaces are closed, denoted as *core* (or *confinement zone*), and one in which the flux surfaces intersect the walls of the device, the *Scrape-Off Layer* (SOL). The boundary between the two regions, the *Last Closed Flux Surface* (LCFS), is also called *separatrix* for this same reason. Lying directly against it one finds the *edge*, which is a thin layer in the closed field line region where steep gradients between core and SOL form. The null of the poloidal magnetic field is named *X-point* after the characteristic shape of the separatrix in its proximity. Each separatrix creates divertor legs, channeling the SOL from the X-point to the divertor targets, where the plasma interacts with the machine wall. The plasma exhaust is thus directed to these targets, also called *strike points*, where impurities are released from the surface and plasma is recycled. The entire region below the X-point constitutes the *divertor* (hence the name of the type of magnetic geometry).

This type of structure constitutes an alternative to *limited* configurations, in which the separation between the core and SOL is obtained by inserting a protruding structure called *limiter* (Fig. 1.2).

The SOL in diverted tokamaks is further partioned into many topological regions depending on the shape of the magnetic flux surfaces:

- the *main SOL*, that is the part of the plasma that is outside the separatrix magnetically connected to the divertor;
- the *wall shadow*, the region in which the flux surfaces intersect the wall rather than the divertor;
- the *Private Flux Region* (PFR), which is the region extending below the X-point and in between the divertor legs, topologically separated from the rest of the SOL

where by *magnetically connected* we refer to the fact that the trajectories of the particles in the plasma lie mostly along the flux surfaces, as cross-field transport is much slower than the parallel one.

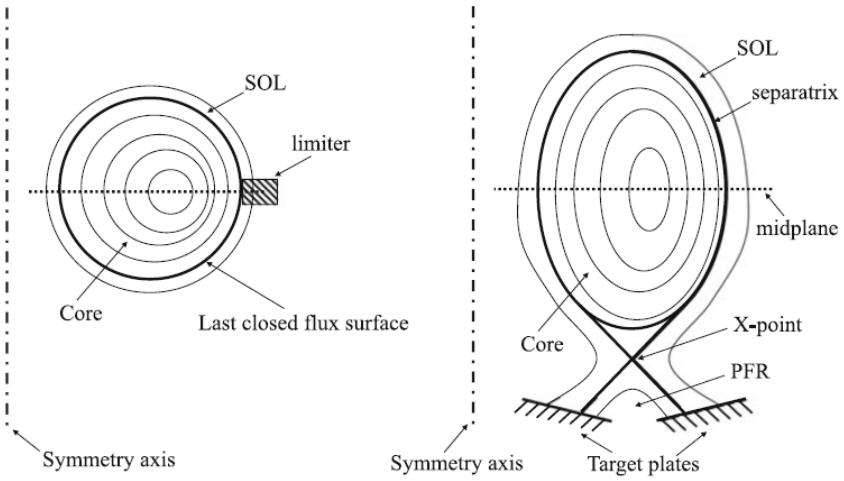

Figure 1.2: Limited vs Diverted configurations
The midplane is defined as the horizontal surface that passes through the magnetic axis of the tokamak (Ref. [6]).

The one illustrated above is, in general, the simplest type of diverted configuration one could find and is generally denoted as *Single Null* to indicate the presence of a unique, first-order null of the poloidal magnetic field, generated by the presence of a current in a poloidal field coil below the bottom of the machine.

The change in scale from ITER to power plants suggest that heat fluxes in the latter could exceed manageable material limits on the target plates were we to consider this type of divertor, as heat loads at the strike points in this case would be too large for the target plates to withstand. Amongst the solutions to the heat load problem one that is being investigated is the employment of the so-called Alternative Divertor Configurations (ADCs): the aim would be to improve upon the Single Null configuration by modifying the magnetic geometry to increase the plasma-wetted area at the strike points (either widening the area at the targets or introducing a higher number of strike points [6, 10]), thus reducing the heat flux at the plates significantly. Each of these solutions presents its unique engineering challenges, therefore there is a delicate balance between the advantages gained in terms of performance, and the engineering feasibility of the different configurations.

1.1.2 The Snowflake divertor

One such solution is that of the *Snowflake* (SF) configuration, introduced in 2007 by Ryutov [11]: the idea is to induce a higher order null at the X-point, so that the separatrix splits the poloidal plane into six sectors instead of four (Fig. 1.3), forming close to the null the characteristic six-branched shape reminiscent of a snowflake (hence the name).

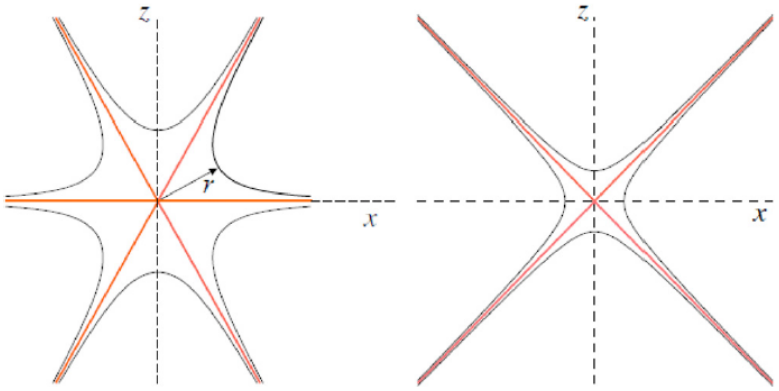

Figure 1.3: Snowflake vs Single Null
The shape of separatrix in the vicinity of the B_{pol} null for the Snowflake divertor (left) and standard divertor (right). Shown by a bold red line is a separatrix; thin line represents an adjacent flux surface (Ref. [12]).

In order to describe this configuration let us consider a poloidal cross-section with the X-point situated at the origin ($R = Z = 0$). Let a be the distance between the null and the plasma coils, set at the $R = 0$ axis, and d be the distance between the symmetrically-situated divertor conductors, which are found at a vertical distance of b below the the $Z = 0$ axis (Fig. 1.4). Denoting by I and I_d the currents passing in the plasma and divertor coils respectively, and neglecting the toroidicity, one finds the following relations to be a necessary and sufficient condition to obtain a second order null at the origin:

1. condition for the zero at the origin: $I_d = I\left(b + \frac{d^2}{4b}\right)$
2. condition for the second order null (null linear terms): $d = 2b\sqrt{\frac{a+b}{a-b}}$

In Fig. (1.4) one can find the visual representation of the shape of the separatrix (bold) and of two nearby flux surfaces(lighter lines) for $b = 0.3a$.

One can notice immediately how pronounced the flux expansion (that is, the broadening of the distance between adjacent flux surfaces) becomes close to the X-point due to the second order null. In particular in this case the modulus of the poloidal magnetic field will scale as $B_{pol} \sim r^2$, where r

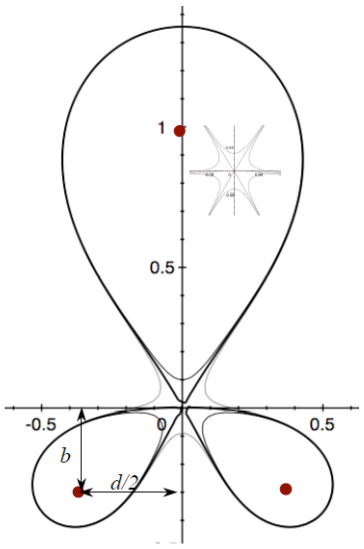

Figure 1.4: Snowflake configuration Schematic representation of the Snowflake configurations with the full associated field lines (Ref. [11]). The thick line represents the separatrix; thin lines outside andinside the separatrix represent flux surfaces whose distance is $0.002a$ from the separatrix in the equatorial plane (i.e., 1 cm for the device with $a = 5$ m). At the scale of the figure, the 1 cm of distance in the main SOL is too small to be resolved, whereas the distance of the outer flux surface from the null-point is approximately 80 cm.

is the distance from the X-point, as opposed to the standard case in which $B_{pol} \sim r$ (Single Null). Thus, the connection length is greatly increased with respect to the standard Single Null, as does the magnetic field shearing near the null point [11]. Lastly, the existence of four strike points (Fig. 1.6) increases the plasma-wetted area assuming uniform activation.

SF configurations are obtained experimentally by generating two first-order X-points close to each other. When the two X-points coincide, a second-order null point is obtained. However, in practice, the two X-points never coincide perfectly: the X-point associated with the separatrix that encloses the plasma is denoted as primary, while the other, the secondary X-point, lays either in the private flux region of the primary X-point or in the main SOL. The first configuration is denoted as the SF plus ($SF+$), the latter as SF minus ($SF-$), while the configuration with the two X-points coinciding is usually referred to as the ideal SF (Fig. 1.5). All these configurations have been experimentally investigated in the TCV [13], NSTX [14], and DIII-D [15] tokamaks.

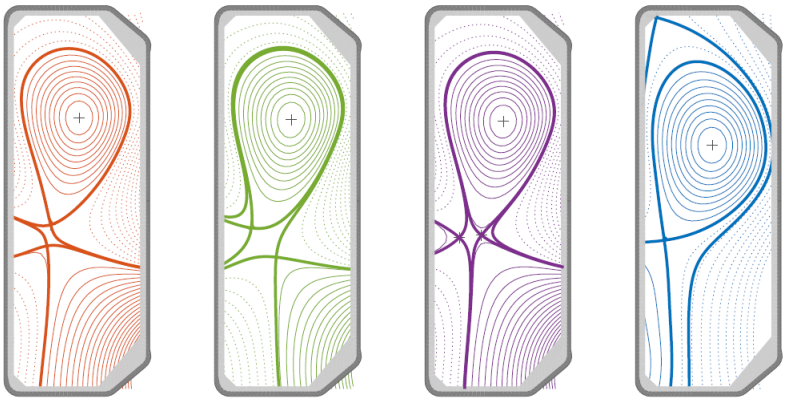

Figure 1.5: 2D poloidal cross-section of a rectangular tokamak vacuum vessel (TCV), demonstrating the (a) SF+, (b) SF-LFS, (c) SF-HFS and (d) SN magnetic field configurations in the poloidal plane (Ref. [2]).

All the characteristics we have mentioned contribute to make this configuration of particular interest for the exhaust problem, as flux expansion is theorised to have an impact on local dynamics. Amongst the mechanisms that arise, we want to focus in our analysis on the convective cell.

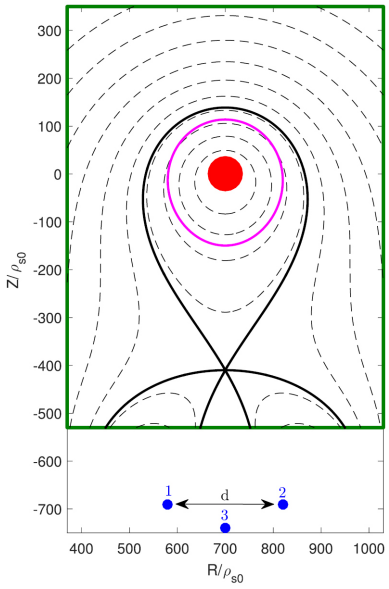

Figure 1.6: Snowflake configuration
Turbulent code simulation of a Snowflake configuration (Ref. [7]). Contour plot of the poloidal flux function, in the ideal SF configuration implemented in simulations (black dashed line). The separatrix is shown as a solid black line. The boundary domain is indicated by a solid green line. The three blue circles represent the position of the current filaments, located outside the simulation domain, responsible of creating the SF configuration, while the red circle represents the center of the plasma current.

1.2 The convective cell

One of the main advantages that the Snowflake configuration introduces with respect to the Single Null is the presence of the additional strike points, which enlarges the exposed area and thus reduces the heat flux at the plates. Experimental measurements in TCV have shown a reduction in the peak heat fluxes compared to similar Single Null cases [8].

As previously mentioned, though, this is conditional on the *activation* of the two additional strike points: they are situated within the private flux region, and as such they would be magnetically isolated with respect to the main SOL were there no perpendicular transport. The natural conclusion is that one should try to investigate the mechanisms which induce the cross-field transport needed for the activation of the secondary strike points.

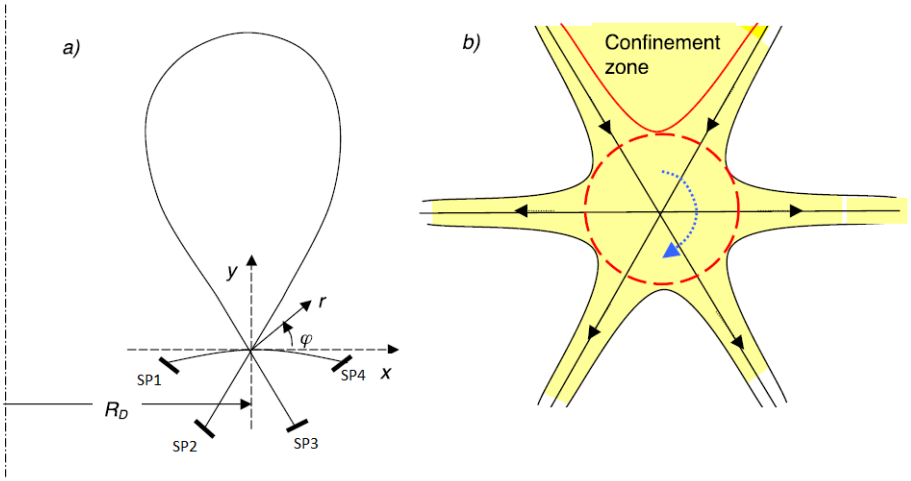

Figure 1.7: The convection zone
(a) Schematic representation of a Snowflake divertor, with the separatrix indicated as a solid black line and the four strike points labelled from 1 to 4. **(b)** The structure of the weak poloidal field zone near the null; black arrows indicate the direction of the plasma flow; dashed red circle encloses the convection zone with blue dashed arrow indicating the initial direction of rotation; solid red line inside the confinement zone shows the boundary of a layer inside the separatrix affected by convection.

The first solution proposed was the so-called "churning mode" ([16, 12]). It theorised the presence of an electromagnetic instability caused by the weak B_{pol} zone in the vicinity of the X-point, which in turn would cause convection to emerge in the area, driven by the toroidal curvature of the magnetic field lines coupled with a vertical pressure gradient. This would cause a poloidal rotation (*churning* motion) around the null without perturbing the toroidal field, thus allowing the plasma to flow into the additional divertor legs. The effect would be present in first-order nulls as well, where the main difference is the size of the convection zone, which is associated to the weak-poloidal-field zone and as such is more larger in the Snowflake case compared to the Single Null.

The proposed model was however not sufficient, as the same effect was found in simulations which neglected electromagnetic fluctuations. In particular it was found that in first-principles global turbulent simulations run using the GBS code ([7]), where the turbulence and equilibrium cross-field transport are evolved self-consistently, one could observe the activation of the inner legs (Fig. 1.8) for different types of Snowflake configurations in reversed B_t configurations.

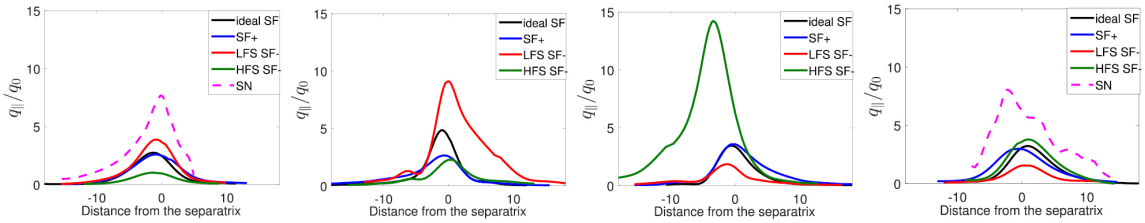

(a) *SP1* **(b)** *SP2* **(c)** *SP3* **(d)** *SP4*

Figure 1.8: Equilibrium parallel heat flux at the target plates
Equilibrium parallel heat flux at the target plates, normalised to the reference value q_0, as a function of the distance from the separatrix, which is evaluated at the midplane and normalised to ρ_{s0}, for different types of SF configurations (labels of the strike-points are in the same order as Fig. 1.7). For comparison equivalent SN values are depicted at the outer legs (Ref. [7]).

The effect is found to be due to a convective cell around the poloidal field null, induced by equilibrium $E \times B$ drift. Indeed, the area interested by this phenomenon showed enhanced cross-field transport (Fig. 1.9), which allowed the plasma in the main SOL to be transported into the PFR and be thus able to reach the secondary target plates SP2 and SP3 (Fig. 1.7).

Moreover, a specific type of potential structure is required to obtain such a convective motion, as one would need a potential well to be formed at the X-point. The immediate consequence is that in order to fully understand the convective cell one should investigate first of all what sets the potential in the divertor area.

1.2.1 Potential structures around the X-point

The formation of a potential structure (well in reversed cases, hill in forward ones) around the X-point has been observed both in experimental devices, such as DIII-D [17], and more recently in TCV [18], and in simulations (XGC [19], SOLPS-ITER [20] and GBS).

It is in particular from 2D simulations run using SOLPS-ITER that *Wensing et al.* obtained a simplified model describing this mechanism in [20], comparing it to TCV experimental data [18]. A scaling relation involving the values of density, temperature and potential at the target and at the X-point was obtained by applying some simplifying assumptions (as for example a simplified geometry and constant flux expansion along the leg). We will go into the details of this specific model later on, but what is vital to highlight here is that a description of the potential hill/well formation phenomenon was proposed already for the simplest case (the Single Null). Both experimental data [8] and other simulation data obtained with codes that better accounted for drift effects [7], however, highlighted how the size of the convective cell was affected by flux expansion, which makes it much more prominent in Snowflake configurations.

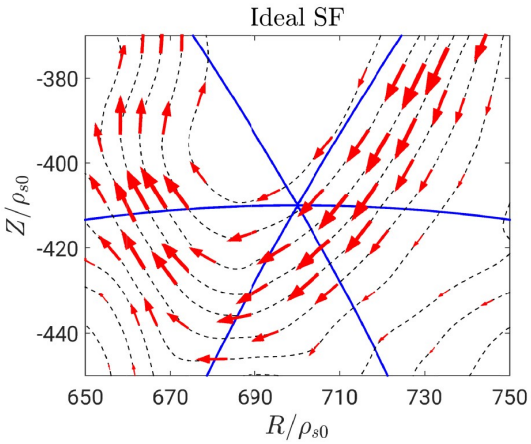

(a) *Ideal SF*

Figure 1.9: The convective cell
Equilibrium $E \times B$ heat flux in the null-point region for the ideal SF configuration. The size of the arrows is proportional to the intensity of the heat flux. Black dashed lines indicate contour levels of the electrostatic potential while the solid blue line indicates the separatrix.

The aim of the present thesis would be to expand on this results, by including drift and flux expansion effects and only considering quantities measured at the target, which are easier to obtain experimentally.

Now, before going into the details of the computational apparatus employed to obtain and analyse the data required for our model, one needs to properly define the theoretical infrastructure to describe it. It is a model widely employed as the physical background of turbulent code simulations: the Drift-Reduced Braginskii Equations.

1.3 The plasma model: Drift-Reduced Braginskii equations

1.3.1 The Braginskii equations

In 1965 Braginskii derived a model to describe the dynamics of a highly collisional plasma: the Braginskii equations [21]. He started from a full kinetic description of the different particle species of the plasma, from which using some specific hypotheses then evolution equations for the macroscopic observables of interest were recovered. In the original model only a single ion species and electrons were considered, but it was later extended to include neutrals and general multi-species plasma.

One starts from a kinetic description of a single-ion species plasma, in terms of a system of Boltzmann equations:

$$\frac{\partial f_n}{\partial t} + \mathbf{v} \cdot \frac{\partial f_n}{\partial \mathbf{x}} = C(f_n, f_i) + C(f_n, f_e) \tag{1.1}$$

$$\frac{\partial f_i}{\partial t} + \mathbf{v} \cdot \frac{\partial f_i}{\partial \mathbf{x}} + q_i \left(\frac{\mathbf{E} + \mathbf{v} \times \mathbf{B}}{m_i} \right) \cdot \frac{\partial f_i}{\partial \mathbf{v}} = C_i\left(f_i, f_e\right) + C(f_i, f_n) \tag{1.2}$$

$$\frac{\partial f_e}{\partial t} + \mathbf{v} \cdot \frac{\partial f_e}{\partial \mathbf{x}} - e \left(\frac{\mathbf{E} + \mathbf{v} \times \mathbf{B}}{m_e} \right) \cdot \frac{\partial f_e}{\partial \mathbf{v}} = C_e\left(f_e, f_i\right) + C(f_e, f_n) \tag{1.3}$$

for $f_a(t, \mathbf{x}, \mathbf{v})$, $a = i, e$ the single particle distribution function for each species, m_e are the ion and electron masses, q_i is the ion charge, e is the elementary charge, and $C(f_a, f_b)$ are the collision operators for the different species.

Here the neutral model is included as they are present in the final system of equations required for the code described in the next chapter, but we will not discuss it as it is not of interest for the

current derivation and was not present in the original Braginskii model (refer to [9] for the details):

$$C(f_n, f_i) + C(f_n, f_e) = -\nu_{iz} f_n - \nu_{cx}\left(f_n - \frac{n_n}{n_i} f_i\right) + \nu_{rec} f_i \tag{1.4}$$

$$C(f_i, f_n) = -\nu_{\rm cx}\left(\frac{n_{\rm n}}{n_i} f_i - f_n\right) + \nu_{\rm iz} f_n - \nu_{\rm rec} f_i + s_i \tag{1.5}$$

$$C(f_e, f_n) = \nu_{\rm iz} n_{\rm n}\left[2\Phi_e\left(\mathbf{V}_{\rm n}, T_{e,\rm iz}\right) - \frac{f_e}{n_e}\right] - \nu_{\rm rec} f_e + \nu_{\rm en} n_{\rm n}\left[\Phi_e\left(\mathbf{V}_n, T_{e,\rm en}\right) - \frac{f_e}{n_e}\right] + s_e \tag{1.6}$$

where $\mathbf{V}_{\rm n} = \int \mathbf{v} f_{\rm n} {\rm d}\mathbf{v}/n_{\rm n}$ is the neutral mean velocity, $\Phi_e(\mathbf{v}, T)$ is a Maxwellian velocity distribution function, and s_i and s_e are external sources of particles and heat. The electron/ion collisions are described through the use of Krook operators with collision frequencies given by:

$$\nu_{\rm ev} = n_e \left\langle v_{e,i} \sigma_{\rm ev}\left(v_{e,i}\right)\right\rangle_{v_{e,i}}, \quad {\rm ev} \in \{\rm iz,\ cx,\ en\}$$

(respectively, *ionization, charge-exchange, electron-neutral elastic collision*).

From these one could define the quantities of interest through the introduction of the first momenta of the respective distribution functions:

$$n_a(t, \mathbf{x}) = \int f_a(t, \mathbf{x}, \mathbf{v}) {\rm d}\mathbf{v} \tag{1.7}$$

$$\mathbf{V}_a(t, \mathbf{x}) = \frac{1}{n_a}\int \mathbf{v} f_a(t, \mathbf{x}, \mathbf{v}) {\rm d}\mathbf{v} = \langle \mathbf{v} \rangle_a \tag{1.8}$$

$$T_a(t, \mathbf{x}) = \frac{1}{n_a}\int \frac{m}{3}\left(\mathbf{v} - \mathbf{V}_a\right)^2 f_a(t, \mathbf{x}, \mathbf{v}) {\rm d}\mathbf{v} = \frac{m}{3}\left\langle \left(\mathbf{v} - \mathbf{V}_a\right)^2 \right\rangle_a \tag{1.9}$$

for $a = i, e$, and by extracting the corresponding momenta of the kinetic equations (1.1 - 1.3) one recovers the evolution equations:

$$\frac{\partial n_e}{\partial t} + \nabla \cdot \left(n_e \mathbf{V}_e\right) = n_{\rm n}\nu_{\rm iz} - n_i \nu_{\rm rec} + s_n \tag{1.10}$$

$$\frac{\partial n_i}{\partial t} + \nabla \cdot \left(n_i \mathbf{V}_i\right) = n_{\rm n}\nu_{\rm iz} - n_i \nu_{\rm rec} + s_n \tag{1.11}$$

$$m_e n_e \frac{{\rm d}_e \mathbf{V}_e}{{\rm d}t} = -\nabla p_e - \nabla \cdot \pi_e - e n_e\left(\mathbf{E} + \mathbf{V}_e \times \mathbf{B}\right) + \mathbf{R}_e + m_e n_{\rm n}\left(\nu_{\rm en} + 2\nu_{\rm iz}\right)\left(\mathbf{V}_{\rm n} - \mathbf{V}_e\right) \tag{1.12}$$

$$m_i n_i \frac{{\rm d}_i \mathbf{V}_i}{{\rm d}t} = -\nabla p_i - \nabla \cdot \pi_i + Z e n_i\left(\mathbf{E} + \mathbf{V}_i \times \mathbf{B}\right) + \mathbf{R}_i + m_i n_{\rm n}\left(\nu_{\rm iz} + \nu_{\rm cx}\right)\left(\mathbf{V}_{\rm n} - \mathbf{V}_i\right) \tag{1.13}$$

$$\begin{aligned}\frac{3}{2} n_e \frac{{\rm d}_e T_e}{{\rm d}t} + p_e \nabla \cdot \mathbf{V}_e = &-\nabla \cdot \mathbf{q}_e - \pi_e : \nabla \mathbf{V}_e + Q_e + n_{\rm n}\nu_{\rm iz}\left[-E_{\rm iz} - \frac{3}{2}T_e + \frac{3}{2} m_e \mathbf{V}_e \cdot \left(\mathbf{V}_e - \frac{4}{3}\mathbf{V}_{\rm n}\right)\right] \\ &- n_{\rm n}\nu_{\rm en} m_e \mathbf{V}_e \cdot \left(\mathbf{V}_{\rm n} - \mathbf{V}_e\right) + n_e s_{T_e}\end{aligned} \tag{1.14}$$

$$\frac{3}{2} n_i \frac{{\rm d}_i T_i}{{\rm d}t} + p_i \nabla \cdot \mathbf{V}_i = -\nabla \cdot \mathbf{q}_i - \pi_i : \nabla \mathbf{V}_i + Q_i + n_i s_{T_i} + n_{\rm n}\left(\nu_{\rm iz} + \nu_{\rm cx}\right)\left[\frac{3}{2}\left(T_{\rm n} - T_i\right) + \frac{m_i}{2}\left(\mathbf{V}_n - \mathbf{V}_i\right)^2\right] \tag{1.15}$$

where the ions have charge $q_i = Ze$ and:

$$\frac{{\rm d}_e}{{\rm d}t} = \frac{\partial}{\partial t} + \mathbf{V}_e \cdot \nabla$$

$$\frac{{\rm d}_i}{{\rm d}t} = \frac{\partial}{\partial t} + \mathbf{V}_i \cdot \nabla$$

are the total time derivatives (*substantial derivatives*, as they are called in [21]) for the electrons and the ions, respectively, and $p_e = n_e T_e$, $p_i = n_i T_i$ are the electron and ion plasma pressures.

For each species, the following quantities are defined:

- the pressure tensor $P_{\alpha\beta} = p_\alpha \delta_{\alpha\beta} + \pi_{\alpha\beta}$, whose entries are defined by:

$$p = nm \left\langle v'^2 \right\rangle /3$$
$$\pi_{\alpha\beta} = mn \left\langle v'_\alpha v'_\beta - v'^2/3\delta_{\alpha\beta} \right\rangle$$

- the change in momentum per time unit of the particles of a given species as a result of collisions with all other species:

$$\mathbf{R} = \int m\mathbf{v}' C \, \mathrm{d}\mathbf{v}$$

- the flux density of heat carried by particles of a given species:

$$\mathbf{q} = nm \left\langle \frac{v'^2}{2} \mathbf{v} \right\rangle$$

- the heat density generated as a consequence of the collisions with the other species in the plasma:

$$Q = \int \frac{mv'^2}{2} C \, \mathrm{d}\mathbf{v}$$

In his treatment, Braginskii proceeded to make some important assumptions on the underlying nature of the collisions in order to recover the evolution equations for such observables; in particular he assumed that:

1. the timescale of the system τ was much longer than than the time interval between two collisions:

$$\tau \gg \tau_{coll}$$

2. the length scale of variation of the system λ was much larger than the mean free path between any two collisions:

$$\lambda \gg \lambda_{m.f.p.}$$

which is indeed the case for highly collisional plasma. He could then employ linear response theory to approximate the solution of (1.2, 1.3) with a perturbed Maxwellian, which in turn entailed a proportionality relation between the quantities $\pi, \mathbf{R}, \mathbf{q}, Q$ and the first momenta $(f, \mathbf{V}, T)$ and their gradients. The proportionality coefficients are called transport coefficients. The transport coefficients in [21] are calculated by assuming a strongly magnetised plane, i.e. $\Omega_a \tau_a \gg 1$, where $\Omega_a = q_a B/m_a, a \in \{e, i\}$ are respectively the electron/ion cyclotron frequencies and

$$\tau_e = \frac{3\sqrt{m_e}}{4\sqrt{2\pi}} \frac{(4\pi\epsilon_0)^2}{Z^2 e^4} \frac{T_e^{3/2}}{n\Lambda}$$
$$\tau_i = \frac{3\sqrt{m_i}}{4\sqrt{2\pi}} \frac{(4\pi\epsilon_0)^2}{Z^4 e^4} \frac{T_i^{3/2}}{n\Lambda}$$

are the electron/ion collision times, with Λ the Coulomb logarithm.

In this approximation, it is shown that the momentum transfer between ions and electrons, $\mathbf{R} = \mathbf{R}_e = -\mathbf{R}_i$, consists of two terms: the friction force, $\mathbf{R}_u$, due to electron/ion collisions, and the thermal force, $\mathbf{R}_T$, due to the coexistence of a temperature gradient in the presence of electron/ion collisions.

By neglecting the friction in the direction perpendicular to the magnetic field and terms of order $1/(\Omega_e \tau_e)$, the friction and thermal forces become:

$$\mathbf{R}_u = e n_e \frac{j_\parallel}{\sigma_\parallel} \mathbf{b} \tag{1.16}$$

$$\mathbf{R}_T = -0.71 n_e \nabla_\parallel T_e \tag{1.17}$$

where $\mathbf{b}$ is the unit vector parallel to the magnetic field, $j_\parallel = e n_e \left(V_{\parallel i} - V_{\parallel e}\right)$ is the current in the direction parallel to $\mathbf{b}$, and $\sigma_\parallel$ is the parallel conductivity:

$$\sigma_\parallel = 1.96 \frac{e^2 n_e \tau_e}{m_e}$$

Within the same approximations, the electron and ion heat fluxes in (1.14, 1.15) are:

$$\mathbf{q}_e = -0.71 n_e T_e \frac{j_\parallel}{e} - \chi_{\parallel e} \mathbf{b} \nabla_\parallel T_e - \frac{5}{2} \frac{n_e T_e}{eB} \mathbf{b} \times \nabla T_e \tag{1.18}$$

$$\mathbf{q}_i = -\chi_{\parallel i} \mathbf{b} \nabla_\parallel T_i + \frac{5}{2} \frac{n_i T_i}{ZeB} \mathbf{b} \times \nabla T_i \tag{1.19}$$

where

$$\chi_{\parallel e} = 3.16 \frac{n_e T_e \tau_e}{m_e}, \qquad \chi_{\parallel i} = 3.9 \frac{n_i T_i \tau_i}{m_i}$$

are the parallel thermal conductivities.

The heat generation Q in (1.14, 1.15) consists of three separate components: the Joule heating due to friction between ions and electrons, which, for the typical timescales of turbulence in the plasma boundary, is negligible; the electron-ion heat transfer; and the term arising from the thermal force. The heat generation for electrons is thus given by:

$$Q_e = \frac{0.71}{e} j_\parallel \nabla T_e + 2 \frac{m_e}{m_i} \frac{n}{\tau_e} \left(T_i - T_e\right) \tag{1.20}$$

while for ions by:

$$Q_i = 2 \frac{m_e}{m_i} \frac{n}{\tau_e} \left(T_e - T_i\right) \tag{1.21}$$

Finally, by taking a frame of reference in which the z axis is aligned along the magnetic field direction, the components of the stress tensor π can be written as:

$$\begin{aligned}
\pi_{xx} &= -\frac{\eta_0}{2} \left(W_{xx} + W_{yy}\right) - \eta_3 W_{xy} \\
\pi_{yy} &= -\frac{\eta_0}{2} \left(W_{xx} + W_{yy}\right) + \eta_3 W_{xy} \\
\pi_{xy} &= \pi_{yx} = \frac{\eta_3}{2} \left(W_{xx} - W_{yy}\right) \\
\pi_{xz} &= \pi_{zx} = -2 \eta_3 W_{yz} \\
\pi_{yz} &= \pi_{zy} = +2 \eta_3 W_{yz} \\
\pi_{zz} &= -\eta_0 W_{zz}
\end{aligned}$$

where the rate-of-strain tensor W is given by:

$$W_{\alpha\beta} = \frac{\partial V_\alpha}{\partial x_\beta} + \frac{\partial V_\beta}{\partial x_\alpha} - \frac{2}{3} \delta_{\alpha\beta} \nabla \cdot \mathbf{V} \tag{1.22}$$

with the viscosities defined by:

$$\eta_{0i} = 0.96 n_i T_i \tau_i, \qquad \eta_{3i} = \frac{n_i T_i}{2\Omega_i} \tag{1.23}$$

$$\eta_{0e} = 0.73 n_e T_e \tau_e, \qquad \eta_{3e} = -\frac{n_e T_e}{2\Omega_e} \tag{1.24}$$

The Braginskii equations we have just obtained describe phenomena occurring in a wide range of time and spatial scales, ranging from the electron cyclotron frequency $\Omega_{ce} = eB/m_e \sim 10^{11}$ s^{-1} up to the energetic confinement timescale $\tau_{en} \sim 1$ s, and from the electron Larmor radius $\rho_e \sim 10^{-5}$ m, up to typical machine size $R_0 \sim 1$ m. At the same time, turbulent fluctuations in the plasma boundary occur at timescale of order 10^{-6} s, which is therefore much slower than the fast cyclotron motion, and on spatial scale of the order of the ion sound Larmor radius, $\rho_s = c_s/\Omega_{ci}$, with c_s the sound speed. Simulating the full model would be extremely numerically challenging, hence we would need a way to eliminate the faster timescales in order to make the model tractable from a numerical point of view. That is precisely where a new simplification, introduced by [22], comes into play: the Drift-Reduction.

1.3.2 Drift-ordering in the Braginskii model

In systems in which the ambient scale lengths are long compared to the characteristic Larmor radii of either ions or electrons $\rho_{e,i}$, instabilities driven by density or pressure gradients typically have characteristic time/space scales which are slower than the characteristic gyro-frequencies $\Omega_{e,i}$ and longer than the Larmor radii. In [22] an approximation is introduced, which allows to eliminate the cyclotron motion of the particles and thus describe only the low-frequency motion of the system. It consists in simplifying Eqs. (1.10 - 1.15) by applying a drift ordering:

$$\frac{\partial}{\partial t} \sim \mathbf{V}_E \cdot \nabla \sim \frac{\rho_s^2}{L_\perp^2}\Omega_{ci} \ll \Omega_{ci} \tag{1.25}$$

being ρ_s much smaller than the typical equilibrium scale length $L_\perp$, and $\mathbf{V}_E = \mathbf{b} \times \nabla\phi/B$ the $\mathbf{E} \times \mathbf{B}$ drift velocity. Moreover, since the plasma turbulence takes place on a spatial scale much larger than the Debye length, we assume the plasma to be quasi-neutral, i.e. $n_i = n_e \equiv n$.

Within this regime the particle velocities can be decomposed into their components parallel and perpendicular to the magnetic field. Defining the electron and ion diamagnetic drift velocities respectively as:

$$\mathbf{V}_{de} = -\frac{1}{enB}\mathbf{b} \times \nabla p_e$$
$$\mathbf{V}_{di} = \frac{1}{ZenB}\mathbf{b} \times \nabla p_i$$

one can derive the expressions for the perpendicular components of the particle velocities by performing the drift-ordering on (1.12, 1.13) and retaining the lowest orders in $\frac{\rho_s^2}{L_\perp^2}$:

$$\mathbf{V}_{\perp e} = \mathbf{V}_E + \mathbf{V}_{de} \tag{1.26}$$

$$\mathbf{V}_{\perp i} = \mathbf{V}_E + \mathbf{V}_{di} + \mathbf{V}_{pol} + \mathbf{V}_{in} \tag{1.27}$$

The zeroth order terms in both equations are given by the $\mathbf{E}\times\mathbf{B}$ and diamagnetic drift velocities, while the lowest order corrections to the ion perpendicular velocity are the polarisation drift, $\mathbf{V}_{\rm pol}$, and the drift arising from the ion-neutral friction due to charge exchange, $\mathbf{V}_{\rm in} = (n_{\rm n}/n)\,(\nu_{\rm cx}/\Omega_{ci})\,(\mathbf{V}_{\perp {\rm n}} - \mathbf{V}_{\perp i})\times \mathbf{b}$.

The ion polarization drift is obtained from (1.13) by neglecting parallel gradients and terms depending on the collisional time in the stress tensor, so that it can be rewritten into two contributions:

- the viscous part:

$$\pi_{vis} = \left(\mathbf{bb} - \frac{I}{3}G\right), \qquad G = -3\eta_0\left(\nabla_\parallel V_\parallel - \boldsymbol{\kappa}\cdot\mathbf{V} - \frac{1}{3}\nabla\cdot\mathbf{V}\right)$$

  with G the stress function and $\boldsymbol{\kappa} = \mathbf{b}\cdot\nabla\mathbf{b}$ the field line curvature;

- the finite Larmor radius (FLR) part:

$$\nabla\cdot\pi_{FLR} = -m_i n\mathbf{V}_{di}\cdot\nabla\mathbf{V}_i + p_i\left(\nabla\times\frac{\mathbf{b}}{\Omega_{ci}}\right)\cdot\nabla\mathbf{V}_i + \nabla_\perp\left(\frac{p_i}{2\Omega_{ci}}\nabla\cdot\mathbf{b}\times\mathbf{V}_i\right) + \mathbf{b}\times\nabla\left(\frac{p_i}{2\Omega_{ci}}\nabla_\perp\cdot\mathbf{V}_i\right)$$

Finally, the ion polarization drift can then be written as:

$$\begin{aligned}\mathbf{V}_{pol} =& \frac{\mathbf{b}}{\Omega_{ci}}\times\frac{\mathrm{d}}{\mathrm{d}t}\mathbf{V}_{\perp i0} + \frac{1}{nm_i\Omega_{ci}}\left\{\mathbf{b}\times\left[p_i\left(\nabla\times\frac{\mathbf{b}}{\Omega_{ci}}\right)\cdot\nabla\mathbf{V}_{\perp i0}\right] + \mathbf{b}\times\nabla_\perp\left(\frac{p_i}{2\Omega_{ci}}\nabla\cdot\mathbf{b}\times\mathbf{V}_{\perp i0}\right)\right.\\ &\left.-\nabla_\perp\left(\frac{p_i}{2\Omega_{ci}}\nabla_\perp\cdot\mathbf{V}_{\perp i0}\right)\right\} + \frac{1}{nm_i\Omega_{ci}}\mathbf{b}\times\left(G\boldsymbol{\kappa} - \frac{\nabla G}{3}\right)\end{aligned} \tag{1.28}$$

where in the substantial derivative we keep only the zeroth order terms after performing the drift-ordering: $\mathrm{d}/\mathrm{d}t = \partial/\partial t + \left(\mathbf{V}_E + V_{\parallel i}\mathbf{b}\right)\cdot\nabla$, being $\mathbf{V}_{\mathrm{pol}} \ll \frac{\rho_s^2}{L_\perp^2}$. The diamagnetic drift cancels out the first term of $\nabla\cdot\pi_{FLR}$.

The polarisation drift nevertheless appears in the convective derivative, despite being small in the drift ordering, because of energy conservation [22], and thus will enter the continuity equation in the form:

$$\nabla\cdot(n\mathbf{V}_{pol}) = \nabla_\perp\cdot\frac{nc}{B\Omega_{ci}}\frac{\mathrm{d}}{\mathrm{d}t}\left(\mathbf{E}_\perp - \frac{\nabla_\perp p_i}{en}\right) + \frac{1}{3m_i\Omega_{ci}}\mathbf{b}\times\boldsymbol{\kappa}\cdot\nabla G \tag{1.29}$$

The electron polarization drift and the drift arising from the electron-neutral interaction are negligible, as they would be a factor $\sqrt{m_e/m_i}$ smaller than the corresponding terms coming from the ion equation.

1.3.3 Semi-electrostatic limit

One last ingredient is needed to obtain the full system of reduced equations: the semi-electrostatic limit. As stated earlier, one has to remove fast oscillations from the model, which in the case of electromagnetic effects are associated to compressional Alfvén waves, as they are several orders of magnitude faster than the typical turbulent fluctuations in the plasma boundary. Similarily to [22], one can do so by introducing the so-called semi-electrostatic approximation, that is:

$$\mathbf{B} = \mathbf{B_0} + \delta\mathbf{B}_\perp$$

where $\mathbf{B_0}$ is the equilibrium magnetic field on top of which we consider small perturbations in the perpendicular direction $\delta\mathbf{B}_\perp$. As a consequence of quasi-neutrality [23], this in turn implies that the component of the vector potential perpendicular to the magnetic field are negligible: that is, given $\mathbf{B} = \nabla\times\mathbf{A}$:

$$\delta\mathbf{B}_\perp = -\nabla\times(\psi\mathbf{b_0}) \iff \delta A_\parallel \sim |\delta\mathbf{A}_\perp|\frac{L_\parallel}{L_\perp} \gg |\delta\mathbf{A}_\perp|$$

where $\mathbf{b_0}$ is the unit vector associated to the equilibrium field, ψ is a toroidally uniform scalar function and $L_\parallel$ is the chacteristic turbulent length scale for the direction parallel to the magnetic field (the last relation holds because of the strong magnetization plane assumption).

In the $\beta = 2\mu_0(p_e + p_i)/B^2 \ll 1$ regime, considering Ampère's law for the magnetic field in the Coulomb gauge and in the absence of displacement currents, we can recover the following expression for the fluctuations:

$$\mu_0 \delta\mathbf{j} = \nabla \times \delta\mathbf{B} = \nabla \times \nabla \times \delta\mathbf{A} = -\nabla^2 \delta\mathbf{A} + \nabla(\nabla \cdot \delta\mathbf{A}) = -\nabla^2 \delta\mathbf{A} = \nabla^2 \psi$$

where $\delta\mathbf{j} = \mathbf{j} - \bar{\mathbf{j}}$ and $\bar{\mathbf{j}}$ is again the equilibrium current on top of which we consider small-scale and small-amplitude perturbations. Within the same approximations, one also recovers the expression for the electric field:

$$\mathbf{E} = -\nabla\phi + \frac{\partial\psi}{\partial t}\mathbf{b}$$

In particular we have that the magnetic fluctuations affect the direction of the magnetic field, and therefore the parallel gradient:

$$\nabla_\parallel = (\mathbf{b} + \delta\mathbf{b}) \cdot \nabla = \mathbf{b} \cdot \nabla - \frac{\nabla \times \psi\mathbf{b}}{B} \cdot \nabla \simeq \mathbf{b} \cdot \nabla + \frac{\mathbf{b}}{B} \times \nabla_\perp \psi \cdot \nabla$$

where the second term is the contribution to the parallel derivative due to magnetic fluctuations.

1.3.4 Conservation laws in the drift-reduction approximation

From all the aformentioned approximations, one can now recover the full system of drift-reduced Braginskii equations.

Quasi-neutrality implies that both continuity equations (1.10, 1.11) should hold at the same time:

$$\frac{\partial n}{\partial t} + \nabla \cdot \left[n \left(\mathbf{V}_E + \mathbf{V}_{di} + \mathbf{V}_{pol} + V_{\parallel i}\mathbf{b} + \mathbf{V}_{\text{in}} \right) \right] = n_{\text{n}} \nu_{\text{iz}} - n\nu_{\text{rec}} + s_n \tag{1.30}$$

$$\frac{\partial n}{\partial t} + \nabla \cdot \left[n \left(\mathbf{V}_E + \mathbf{V}_{de} + V_{\parallel e}\mathbf{b} \right) \right] = n_{\text{n}} \nu_{\text{iz}} - n\nu_{\text{rec}} + s_n \tag{1.31}$$

Thus, subtracting one from the other, one obtains the added constraint:

$$\nabla \cdot (n\mathbf{V}_{pol}) + \frac{1}{e}\nabla_\parallel j_\parallel + \nabla \cdot \left[n \left(\mathbf{V}_{di} - \mathbf{V}_{de} \right) \right] + \nabla \cdot (n\mathbf{V}_{\text{in}}) = 0 \tag{1.32}$$

where the implicit assumption is that the modulus B of the magnetic field varies slowly along $\mathbf{b}$, i.e. $\nabla \cdot f\mathbf{b} \simeq \nabla_\parallel f$. The above relation is called the vorticity equation, and corresponds to the condition $\nabla \cdot \mathbf{j} = 0$. Replacing the explicit expression obtained for the polarization drift contribution in the equation obtains its final form:

$$\begin{aligned} \nabla_\perp \cdot \left[\frac{n}{B\Omega_{ci}} \frac{\mathrm{d}}{\mathrm{d}t} \left(\mathbf{E}_\perp - \frac{\nabla_\perp p_i}{en} \right) \right] + \frac{1}{3m_i\Omega_{ci}} \mathbf{b} \times \boldsymbol{\kappa} \cdot \nabla G + \frac{1}{e}\nabla_\parallel j_\parallel + \nabla \cdot \left[n \left(\mathbf{V}_{di} - \mathbf{V}_{de} \right) \right] \\ + \frac{n_{\text{n}}}{n} \nu_{\text{cx}} \nabla \cdot \left(n\mathbf{E}_\perp - \frac{1}{e}\nabla_\perp p_i \right) = 0 \end{aligned} \tag{1.33}$$

which in particular determines the time evolution of $\mathbf{E}_\perp$.

The ion and electron parallel momentum balance equations are recovered by projecting respectively (1.13) and (1.12) onto the parallel direction, that is:

$$m_e \frac{\mathrm{d}_e V_{\parallel e}}{\mathrm{d}t} = -\frac{1}{n}\nabla_\parallel p_e + e\nabla_\parallel \phi - e\frac{\partial\psi}{\partial t} + e\frac{j_\parallel}{\sigma_\parallel} - 0.71\nabla_\parallel T_e + m_e \frac{n_{\text{n}}}{n} \left(\nu_{en} + 2\nu_{\text{iz}} \right) \left(V_{\parallel n} - V_{\parallel e} \right) \tag{1.34}$$

$$m_i \frac{\mathrm{d}V_{\parallel i}}{\mathrm{d}t} = -\frac{1}{n}\nabla \left(p_i + p_e \right) - \frac{2}{3}\nabla_\parallel G_i + m_i \frac{n_{\text{n}}}{n} \left(\nu_{\text{iz}} + \nu_{\text{cx}} \right) \left(V_{\parallel n} - V_{\parallel i} \right) \tag{1.35}$$

where again we have used the fact that the modulus B of the magnetic field varies slowly along $\mathbf{b}$ to simplify the terms associated to $\nabla \cdot \pi_e$ and neglected terms of order m_e/m_i and $\sqrt{m_e/m_i}$ in the ion parallel momentum equation.

Lastly, the temperature equations are derived from (1.14, 1.15) by applying the drift-ordering. By neglecting the viscous heat losses, the frictional heating related to $\mathbf{R}_u$ and the electron-ion heat transfer, we obtain:

$$\begin{aligned}\frac{3}{2}n\frac{\mathrm{d}_e T_e}{\mathrm{d}t} + \frac{3}{2}n\mathbf{V}_{de}\cdot\nabla T_e + p_e\nabla\cdot\left(\mathbf{V}_E+\mathbf{V}_{de}+V_{\parallel e}\mathbf{b}\right) - 0.71\frac{T_e}{e}\nabla_\parallel j_\parallel - \nabla_\parallel\left(\chi_{\parallel e}\nabla_\parallel T_e\right)\\ - \frac{5e}{2}\nabla\cdot\left[p_e\left(\frac{\mathbf{b}}{B}\times\nabla T_e\right)\right] + 2\frac{m_e}{m_i}\frac{n}{\tau_e}\left(T_e-T_i\right) = s_{T_e}+S^{\mathrm{n}}_{T_e} \qquad (1.36)\\ \frac{3}{2}n\frac{\mathrm{d}T_i}{\mathrm{d}t} + \frac{3}{2}n\mathbf{V}_{di}\nabla T_i + p_i\nabla\cdot\left(\mathbf{V}_E+\mathbf{V}_{di}+\mathbf{V}_{pol}+V_{\parallel i}\mathbf{b}\right) - \nabla_\parallel\left(\chi_{\parallel i}\nabla_\parallel T_i\right)\\ + \frac{5e}{2}\nabla\cdot\left[p_i\left(\frac{\mathbf{b}}{B}\times\nabla T_i\right)\right] + 2\frac{m_e}{m_i}\frac{n}{\tau_e}\left(T_i-T_e\right) = s_{T_i}+S^{\mathrm{n}}_{T_i} \qquad (1.37)\end{aligned}$$

where the respective source terms in the r.h.s.:

$$S^{\mathrm{n}}_{T_e} = n_{\mathrm{n}}\nu_{\mathrm{iz}}\left[-E_{\mathrm{iz}} - \frac{3}{2}T_e + \frac{3}{2}m_e\mathbf{V}_e\cdot\left(\mathbf{V}_e - \frac{4}{3}\mathbf{V}_{\mathrm{n}}\right)\right] - n_{\mathrm{n}}\nu_{\mathrm{en}}m_e\mathbf{V}_e\cdot\left(\mathbf{V}_{\mathrm{n}}-\mathbf{V}_e\right) \qquad (1.38)$$

$$S^{\mathrm{n}}_{T_i} = n_{\mathrm{n}}\left(\nu_{\mathrm{iz}}+\nu_{\mathrm{cx}}\right)\left[T_{\mathrm{n}} - T_i + \frac{1}{3}\left(V_{\parallel\mathrm{n}}-V_{\parallel i}\right)^2\right] \qquad (1.39)$$

account for interactions with the neutrals. The second equation, in particular, can be rewritten by evaluating the term $\nabla\cdot\mathbf{V}_{\mathrm{pol}}$ from the ion and electron continuity equations:

$$n\nabla\cdot\left(\mathbf{V}_E+\mathbf{V}_{di}+\mathbf{V}_{pol}+\mathbf{V}_{\mathrm{in}}+V_{\parallel i}\mathbf{b}\right) = -\mathbf{V}_{di}\cdot\nabla n - \frac{\mathrm{d}n}{\mathrm{d}t} \qquad (1.40)$$

where the terms $\mathbf{V}_{\mathrm{pol}}\cdot\nabla n$ and $\mathbf{V}_{\mathrm{in}}\cdot\nabla n$ are dropped because of the drift-reduced ordering, and

$$\frac{\mathrm{d}n}{\mathrm{d}t} = \frac{\mathrm{d}_e n}{\mathrm{d}t} + \left(V_{\parallel i}-V_{\parallel e}\right)\nabla_\parallel n \qquad (1.41)$$

Thus its final form will be:

$$\begin{aligned}\frac{3}{2}n\frac{\mathrm{d}T_i}{\mathrm{d}t} + T_i\nabla\cdot n\mathbf{V}_{de} + p_i\nabla\cdot\left(\mathbf{V}_E+V_{\parallel e}\mathbf{b}\right) - T_i\frac{j_\parallel}{en}\nabla_\parallel n - \nabla_\parallel\left(\chi_{\parallel i}\nabla_\parallel T_i\right) +\\ + \frac{5p_i}{2e}\left(\nabla\times\frac{\mathbf{b}}{B}\right)\cdot\nabla T_i + 2\frac{m_e}{m_i}\frac{n}{\tau_e}\left(T_i-T_e\right) = s_{T_i}+S^{\mathrm{n}}_{T_i} \qquad (1.42)\end{aligned}$$

1.3.5 Drift-reduced Braginskii equations

We recall the previously introduced cylindrical non-field-aligned coordinate system (R,φ,Z), where R is the distance from the axis of symmetry of the torus, Z is the vertical coordinate, and φ is the toroidal angle. Then, collecting all equations and rewriting them as explicit evolution equations for our observables of interest (density, vorticity, parallel velocities and temperatures) in the new coordinate system, the following system is recovered:

$$\frac{\partial n}{\partial t} = -\frac{1}{B}[\phi,n] + \frac{2}{eB}\left[C\left(p_e\right) - enC(\phi)\right] - \nabla_\parallel\left(nV_{\parallel e}\right) + s_n + \nu_{\mathrm{iz}}n_{\mathrm{n}} - \nu_{\mathrm{rec}}n \qquad (1.43)$$

$$\frac{\partial \Omega}{\partial t} = -\frac{1}{B}\nabla\cdot[\phi,\omega] - \nabla\cdot\left(V_{\parallel i}\nabla_\parallel\omega\right) + \frac{B\Omega_{ci}}{e}\nabla_\parallel j_\parallel + \frac{2\Omega_{ci}}{e}C\left(p_e+p_i\right) + \frac{\Omega_{ci}}{3e}C\left(G_i\right) - \frac{n_{\mathrm{n}}}{n}\nu_{\mathrm{cx}}\Omega \qquad (1.44)$$

$$\begin{aligned}\frac{\partial U_{\parallel e}}{\partial t} = -\frac{1}{B}\left[\phi,V_{\parallel e}\right] - V_{\parallel e}\nabla_\parallel V_{\parallel e} + \frac{e}{m_e}\left(\frac{j_\parallel}{\sigma_\parallel} + \nabla_\parallel\phi - \frac{1}{en}\nabla_\parallel p_e - \frac{0.71}{e}\nabla_\parallel T_e - \frac{2}{3en}\nabla_\parallel G_e\right) +\\ + \frac{n_{\mathrm{n}}}{n}\left(\nu_{\mathrm{en}}+2\nu_{\mathrm{iz}}\right)\left(V_{\parallel n}-V_{\parallel e}\right) \qquad (1.45)\end{aligned}$$

$$\frac{\partial V_{\parallel i}}{\partial t} = -\frac{1}{B}\left[\phi, V_{\parallel i}\right] - V_{\parallel i}\nabla_\parallel V_{\parallel i} - \frac{1}{m_i n}\nabla_\parallel\left(p_e + p_i\right) - \frac{2}{3m_i n}\nabla_\parallel G_i + \frac{n_\mathrm{n}}{n}\left(\nu_\mathrm{iz} + \nu_\mathrm{cx}\right)\left(V_{\parallel n} - V_{\parallel i}\right) \quad (1.46)$$

$$\begin{aligned}\frac{\partial T_e}{\partial t} =& -\frac{1}{B}\left[\phi, T_e\right] - V_{\parallel e}\nabla_\parallel T_e + \frac{2}{3}T_e\left[0.71\frac{\nabla_\parallel j_\parallel}{en} - \nabla_\parallel V_{\parallel e}\right] + \frac{4}{3}\frac{T_e}{eB}\left[\frac{7}{2}C\left(T_e\right) + \frac{T_e}{n}C(n) - eC(\phi)\right] + \\ &+ \nabla_\parallel\left(\chi_{\parallel e}\nabla_\parallel T_e\right) + s_{T_e} - \frac{n_\mathrm{n}}{n}\nu_\mathrm{en}m_e\frac{2}{3}V_{\parallel e}\left(V_{\parallel n} - V_{\parallel e}\right) - \frac{4}{3}\frac{m_e}{m_i}\frac{1}{\tau_e}\left(T_e - T_i\right) + \\ &+ \frac{n_\mathrm{n}}{n}\nu_\mathrm{iz}\left[-\frac{2}{3}E_\mathrm{iz} - T_e + m_e V_{\parallel e}\left(V_{\parallel e} - \frac{4}{3}V_{\parallel n}\right)\right] \end{aligned} \quad (1.47)$$

$$\begin{aligned}\frac{\partial T_i}{\partial t} =& -\frac{1}{B}\left[\phi, T_i\right] - V_{\parallel i}\nabla_\parallel T_i + \frac{4}{3}\frac{T_i}{eB}\left[C\left(T_e\right) + \frac{T_e}{n}C(n) - eC(\phi)\right] - \frac{10}{3}\frac{T_i}{eB}C\left(T_i\right) + \\ &+ \frac{2}{3}T_i\left[\left(V_{\parallel i} - V_{\parallel e}\right)\frac{\nabla_\parallel n}{n} - \nabla_\parallel V_{\parallel e}\right] + \nabla_\parallel\left(\chi_{\parallel i}\nabla_\parallel T_i\right) + s_{T_i} + \frac{4}{3}\frac{m_e}{m_i}\frac{1}{\tau_e}\left(T_e - T_i\right) + \\ &+ \frac{n_\mathrm{n}}{n}\left(\nu_\mathrm{iz} + \nu_\mathrm{cx}\right)\left[T_n - T_i + \frac{1}{3}\left(V_{\parallel n} - V_{\parallel i}\right)^2\right] \end{aligned} \quad (1.48)$$

The above equations are coupled to the Poisson and Ampère equations discussed earlier:

$$\nabla\cdot\left(n\nabla_\perp\phi\right) = \Omega - \frac{\nabla_\perp^2 p_i}{e} \quad (1.49)$$

$$\left(\nabla_\perp^2 - \frac{e^2\mu_0}{m_e}n\right)V_{\parallel e} = \nabla_\perp^2 U_{\parallel e} - \frac{e^2\mu_0}{m_e}nV_{\parallel i} + \frac{e^2\mu_0}{m_e}\bar{j}_\parallel \quad (1.50)$$

where $\Omega = \nabla\cdot\boldsymbol{\omega} = \nabla\cdot\left(n\nabla_\perp\phi + \nabla_\perp p_i/e\right)$ is the scalar vorticity, while $U_{\parallel e} = V_{\parallel e} + e\psi/m_e$ is the sum of the electron inertia and the electromagnetic induction contributions. In the system of equations the following operators have been introduced:

- the $\mathbf{E}\times\mathbf{B}$ convective term:
$$\left[\phi, f\right] = \mathbf{b}\cdot\left(\nabla\phi\times\nabla f\right)$$
- the curvature operator:
$$C(f) = \frac{B}{2}\left(\nabla\times\frac{\mathbf{b}}{B}\right)\cdot\nabla f$$
- the parallel gradient, which includes the electromagnetic flutter contribution:
$$\nabla_\parallel f = \mathbf{b}\cdot\nabla f + \frac{1}{B}\left[\psi, f\right]$$
- the perpendicular Laplacian:
$$\nabla_\perp^2 f = \nabla\cdot\left[\left(\mathbf{b}\times\nabla f\right)\times\mathbf{b}\right]$$

given f a general scalar function.

Additionally, we define externally imposed sources in the density and temperature equations, s_n and s_T, which are analytical and toroidally uniform functions of the poloidal magnetic flux $\psi(R,Z)$,

$$s_n = s_{n0}\exp\left(-\frac{\left(\psi(R,Z) - \psi_n\right)^2}{\Delta_n^2}\right)$$

$$s_T = \frac{s_{T0}}{2}\left[\tanh\left(-\frac{\psi(R,Z) - \psi_T}{\Delta_T}\right) + 1\right]$$

where ψ_n and ψ_T are flux surfaces located inside the separatrix.

The gyroviscous terms are defined as:

$$G_i = -\eta_{0i}\left[2\nabla_\parallel V_{\parallel i} + \frac{1}{B}C(\phi) + \frac{1}{enB}C\left(p_i\right)\right] \tag{1.51}$$

$$G_e = -\eta_{0e}\left[2\nabla_\parallel V_{\parallel e} + \frac{1}{B}C(\phi) - \frac{1}{enB}C\left(p_e\right)\right] \tag{1.52}$$

where $\eta_{0i} = 0.96nT_i\tau_i$ and $\eta_{0e} = 0.73nT_e\tau_e$.

Before moving on to the discussion of the implementation of the numerical implementation of the model just recovered, we would discuss an important additional approximation that is not only relevant for the code itself, but also for all the analytic derivations present in this thesis: the large aspect ratio approximation.

1.3.6 Differential operators in the large-aspect-ratio approximation

Most of the analytic derivations and the numerical implementation of the above model will make use of the large aspect ratio approximation [9]. It will particularly affect the differential operators previously introduced, as it simplifies greatly their analytic expressions.

Introducing the same (R, φ, Z) coordinate system previously discussed, the toroidally symmetric equilibrium magnetic field is written in terms of the poloidal magnetic flux ψ, as:

$$\mathbf{B} = RB_\varphi\nabla\varphi + \nabla\varphi\times\nabla\psi \tag{1.53}$$

where $\psi = \psi(R, Z)$ is itself toroidally symmetric.

In order to perform our approximation, we recall that the magnetic field is decomposed as:

$$\mathbf{B} = B_R\mathbf{e}_R + B_Z\mathbf{e}_Z + B_\varphi\mathbf{e}_\varphi = \mathbf{B}_p + B_\varphi\mathbf{e}_\varphi \tag{1.54}$$

with $\mathbf{e}_R$, $\mathbf{e}_Z$ and $\mathbf{e}_\varphi$ the basis vectors.

Then the large aspect ratio expansion will be performed in terms of the parameters $\epsilon \sim r/R_0 \ll 1$ and $\delta \sim B_p/B_\varphi \ll 1$, where r is the minor radius and the implicit assumption is that the poloidal component of the magnetic field is smaller than the toroidal one. Additionally one assumes a safety factor at the midplane $q \sim \epsilon/\delta$ of order unity. Leading order terms in ϵ and δ will be retained in our expansions.

We start by noticing that, at zeroth-order in ϵ and δ, the modulus of the magnetic field is constant:

$$\frac{B^2}{B_0^2} = \frac{B_R^2}{B_0^2} + \frac{B_Z^2}{B_0^2} + \frac{B_\varphi^2}{B_0^2} = \frac{B_\varphi^2}{B_0^2} + O\left(\delta^2\right) = 1 + O\left(\epsilon, \delta^2\right) \tag{1.55}$$

with B_0 the modulus of the tmagnetic field taken at the tokamak magnetic axis. This will be particularly useful in the next chapter, when the need will arise of the definition of normalization parameters.

Then, given a scalar function f, one can proceed to expand all the previously mentioned operators in ϵ and δ.

In particular, the Poisson brackets take the form:

$$\begin{aligned}
[\phi, f] &= \mathbf{b}\cdot\nabla\phi\times\nabla f = \\
&= \mathbf{b}\cdot\left[\left(\partial_R\phi\mathbf{e}_R + \partial_Z\phi\mathbf{e}_Z + \frac{1}{R}\partial_\varphi\phi\mathbf{e}_\varphi\right)\times\left(\partial_R f\mathbf{e}_R + \partial_Z f\mathbf{e}_Z + \frac{1}{R}\partial_\varphi f\mathbf{e}_\varphi\right)\right] = \\
&= \frac{1}{R}\frac{B_R}{B}\left(\partial_\varphi\phi\partial_Z f - \partial_Z\phi\partial_\varphi f\right) + \frac{1}{R}\frac{B_Z}{B}\left(\partial_R\phi\partial_\varphi f - \partial_\varphi\phi\partial_R f\right) + \frac{B_\varphi}{B}\left(\partial_Z\phi\partial_R f - \partial_R\phi\partial_Z f\right)
\end{aligned} \tag{1.56}$$

which, normalising poloidal lengths in terms of the reference ion sound Larmor radius, ρ_{s0}, and toroidal lengths in terms of the tokamak major radius, R_0 to obtain a dimensionless form, gives:

$$[\phi, f] = \frac{\rho_{s0}}{R}\frac{B_R}{B}\left(\partial_\varphi\phi\partial_Z f - \partial_Z\phi\partial_\varphi f\right) + \frac{\rho_{s0}}{R}\frac{B_Z}{B}\left(\partial_R\phi\partial_\varphi f - \partial_\varphi\phi\partial_R f\right) + \frac{B_\varphi}{B}\left(\partial_Z\phi\partial_R f - \partial_R\phi\partial_Z f\right) =$$
$$= \frac{B_\varphi}{B}\left(\partial_Z\phi\partial_R f - \partial_R\phi\partial_Z f\right) + O(\epsilon,\delta) \tag{1.57}$$

as $B_Z/B \sim B_R/B \sim \delta$ and $\rho_{s0}/R \sim \rho_{s0}/R_0 \ll r/R_0 \sim \epsilon$.

Neglecting local current (i.e., assuming $\nabla \times \mathbf{B} = 0$), the curvature operator can be expanded in ϵ and δ as:

$$C(f) = \frac{B}{2}\left(\nabla \times \frac{\mathbf{b}}{B}\right)\cdot\nabla f =$$
$$= \frac{1}{2B}\left(\frac{B_\varphi}{B^2}\partial_Z B^2\partial_R f - \frac{B_\varphi}{B^2}\partial_R B^2\partial_Z f\right) + O(\epsilon,\delta) \tag{1.58}$$

The poloidal derivatives $\partial_Z B^2$ and $\partial_R B^2$ are given by:

$$\frac{\partial_Z B^2}{B_0^2} = \frac{\partial}{\partial Z}\left(\frac{R_0}{R}\right)^2 + O\left(\delta^2\right) = 0 + O\left(\delta^2\right) \tag{1.59}$$
$$\frac{\partial_R B^2}{B_0^2} = \frac{\partial}{\partial R}\left(\frac{R_0}{R}\right)^2 + O\left(\delta^2\right) = -2\frac{R_0^2}{R^3} + O\left(\delta^2\right) = -\frac{2}{R} + O\left(\epsilon,\delta^2\right) \tag{1.60}$$

where we use $B_\varphi^2/B_0^2 = R_0^2/R^2 = 1 + O(\epsilon)$. Finally, maintaining only the leading order terms in ϵ and δ, the curvature operator, normalised to $1/\left(R_0\rho_{s0}\right)$, becomes:

$$C(f) = \frac{B_\varphi}{B_0}\partial_Z f + O(\epsilon,\delta)$$

The parallel gradient is normalised to $1/R_0$ and, in dimensionless units, is given by:

$$\nabla_\parallel f = \mathbf{b}\cdot\nabla f = \rho_*^{-1}\left(\frac{B_R}{B}\partial_R f + \frac{B_Z}{B}\partial_Z f + \frac{B_\varphi}{B}\frac{\rho_{s0}}{R}\partial_\varphi f\right) =$$
$$= \partial_Z\psi\partial_R f - \partial_R\psi\partial_Z f + \frac{B_\varphi}{B_0}\partial_\varphi f + O(\epsilon,\delta) \tag{1.61}$$

where $B_R = \partial_Z\psi/R, B_Z = -\partial_R\psi/R$.

Lastly, the perpendicular laplacian can be recovered as:

$$\nabla_\perp^2 f = \nabla\cdot\left[\frac{1}{B^2}(\mathbf{B}\times\nabla f)\times\mathbf{B}\right] = \frac{1}{B^2}\nabla\cdot[(\mathbf{B}\times\nabla f)\times\mathbf{B}] - \frac{\nabla B^2}{B^4}\cdot[(\mathbf{B}\times\nabla f)\times\mathbf{B}] \tag{1.62}$$

The second term on the right-hand side of (1.62) is one order ϵ smaller than the first one, which can be written in cylindrical coordinates as:

$$(\mathbf{B}\times\nabla f)\times\mathbf{B} = \left(B_Z^2\partial_R f - B_Z B_R\partial_Z f - \frac{B_R B_\varphi}{R}\partial_\varphi f + B_\varphi^2\partial_R f\right)\mathbf{e}_R$$
$$+ \left(B_\varphi^2\partial_Z f - \frac{B_Z B_\varphi}{R}\partial_\varphi f - B_Z B_R\partial_R f + B_R^2\partial_Z f\right)\mathbf{e}_Z$$
$$+ \left(\frac{B_R^2}{R}\partial_\varphi f - B_\varphi B_R\partial_R f - B_\varphi B_Z\partial_Z f + \frac{B_Z^2}{R}\partial_\varphi f\right)\mathbf{e}_\varphi \tag{1.63}$$

and expanded in ϵ and δ,

$$(\mathbf{B} \times \nabla f) \times \mathbf{B} \simeq \frac{B_\varphi^2}{B^2} \partial_R f \mathbf{e}_R + \frac{B_\varphi^2}{B^2} \partial_Z f \mathbf{e}_Z + O(\epsilon, \delta) \tag{1.64}$$

Thus, the leading order terms can be expressed as:

$$\nabla_\perp^2 f = \partial_{RR}^2 f + \partial_{ZZ}^2 f + O(\epsilon, \delta) \tag{1.65}$$

which gives the final expression for the last of our basic operators defined in the system of equations.

Now that we have the full physical apparatus, we can proceed to describe the practical tools we have used to study the phenomenon, starting from the most important one: the simulation code itself.

Chapter 2

The methodology: numerical tools and general notation

Now that the main physical background has been clarified, what remains to be discussed is the details of the general methodology which will be employed.

The present chapter is divided in three sections: the first one will recall the previously introduced physical model and will delve into the details of the implementation of the simulation code, GBS, and the possible approximations which will take place; the second section will illustrate the simulation data that has been examined in our post-processing code, so to have a comprehensive description of the subset of the parameter space we will be working in; the third one specifies some details about the notation that will be used throughout the present thesis, so to have it clear and fixed for the analytic derivations that will follow.

2.1 The GBS Code

GBS (*Global Braginskii Solver*) is a first-principles, three-dimensional, flux-driven, global, turbulence code that evolves the drift-reduced Braginskii equations.

The GBS code was initially developed to study plasma turbulence in basic plasma devices [24]. The very first version evolved the two-dimensional plasma dynamics in the plane perpendicular to the magnetic field [25], but was later extended to include the direction parallel to the magnetic field. In 2012, a new version of GBS was developed to simulate plasma turbulence in the scrape-off layer of tokamak devices in limited magnetic configurations [26], in which an electrostatic model in the cold ion limit was considered, along with a specific approximation which allowed to simplify the numerical implementation of the divergence of the polarisation current (the Boussinesq approximation, which we will discuss in detail later). A second version of GBS was developed in 2016 [27], where the physical model was improved by adding the ion temperature dynamics and electromagnetic effects. The Boussinesq approximation was relaxed and the plasma model was coupled to a self-consistent kinetic neutral model, leading to the first plasma turbulence simulations of the Scrape-Off Layer that self-consistently include the coupling to the neutral dynamics. Subsequently, a non-field-aligned coordinate system was introduced in GBS to simulate complex magnetic geometries including one or more X-points and a third version of the code was reported in 2018, leading to the first GBS simulation of a diverted geometry [28]. The second-order numerical scheme was improved to a fourth-order finite difference scheme, with a domain with circular poloidal cross-section that avoided the core region.

Finally, a new version of the code appeared in 2022 [24], which significantly improved the previous by introducing a rectangular poloidal cross-section which included the core region, encompassing the whole plasma volume and avoiding an artificial boundary with the core. The core region is present in the simulations, as previously stated, but core dynamics are not correctly reproduced as they would

be outside the regime of validity of the aforementioned physical model: its function is to avoid the artificial boundary conditions at the separatrix which would not retain the core-edge-SOL turbulence interplay, that is found to play a key role in determining the plasma dynamics of the tokamak boundary. A cartesian system of coordinates was chosen, and the new domain allowed for more flexibility on the choice of the magnetic configuration, which could now be loaded from an equilibrium reconstruction or a Grad-Shafranov solver, making room for more exotic magnetic geometries (specifically, Snowflake divertor configurations). A significant speed-up was achieved by implementing a new iterative solver for the Poisson and Ampère equations, therefore allowing for efficient electromagnetic simulations that avoid the use of the Boussinesq approximation.

The present thesis considers data from simulations run employing this last version of the code, used to describe the turbulence in the boundary region of diverted tokamaks.

2.1.1 GBS equations

The physical model described in the previous chapter (Eqs. 1.43 - 1.48) is implemented in GBS in dimentionless form ([9, 27]), that is:

$$\begin{aligned}
\frac{\partial n}{\partial t} =& -\frac{\rho_*^{-1}}{B}[\phi, n] + \frac{2}{B}\left[C\left(p_e\right) - nC(\phi)\right] - \nabla_\parallel\left(nV_{\parallel e}\right) + D_n\nabla_\perp^2 n + D_{n,\parallel}\nabla_\parallel^2 n \\
&+ s_n + \nu_{\mathrm{iz}} n_{\mathrm{n}} - \nu_{\mathrm{rec}} n \qquad (2.1)\\
\frac{\partial \Omega}{\partial t} =& -\frac{\rho_*^{-1}}{B}\nabla\cdot[\phi,\omega] - \nabla\cdot\left(V_{\parallel i}\nabla_\parallel\omega\right) + B^2\nabla_\parallel j_\parallel + 2BC\left(p_e + \tau p_i\right) \\
&+ \frac{B}{3}C\left(G_i\right) + D_\Omega\nabla_\perp^2\Omega - \frac{n_{\mathrm{n}}}{n}\nu_{\mathrm{cx}}\Omega + D_{\Omega,\parallel}\nabla_\parallel^2\Omega \qquad (2.2)\\
\frac{\partial U_{\parallel e}}{\partial t} =& -\frac{\rho_*^{-1}}{B}\left[\phi, V_{\parallel e}\right] - V_{\parallel e}\nabla_\parallel V_{\parallel e} + \frac{m_i}{m_e}\left(\nu j_\parallel + \nabla_\parallel\phi - \frac{1}{n}\nabla_\parallel p_e - 0.71\nabla_\parallel T_e - \frac{2}{3n}\nabla_\parallel G_e\right) \\
&+ D_{V_{\parallel e}}\nabla_\perp^2 V_{\parallel e} + \frac{n_{\mathrm{n}}}{n}\left(\nu_{\mathrm{en}} + 2\nu_{\mathrm{iz}}\right)\left(V_{\parallel n} - V_{\parallel e}\right) + D_{V_{\parallel,e},\parallel}\nabla_\parallel^2 V_{\parallel,e} \qquad (2.3)\\
\frac{\partial V_{\parallel i}}{\partial t} =& -\frac{\rho_*^{-1}}{B}\left[\phi, V_{\parallel i}\right] - V_{\parallel i}\nabla_\parallel V_{\parallel i} - \frac{1}{n}\nabla_\parallel\left(p_e + \tau p_i\right) - \frac{2}{3n}\nabla_\parallel G_i \\
&+ D_{V_{\parallel i}}\nabla_\perp^2 V_{\parallel i} + \frac{n_{\mathrm{n}}}{n}\left(\nu_{\mathrm{iz}} + \nu_{\mathrm{cx}}\right)\left(V_{\parallel n} - V_{\parallel i}\right), \qquad (2.4)\\
\frac{\partial T_e}{\partial t} =& -\frac{\rho_*^{-1}}{B}\left[\phi, T_e\right] - V_{\parallel e}\nabla_\parallel T_e + \frac{2}{3}T_e\left[0.71\frac{\nabla_\parallel j_\parallel}{n} - \nabla_\parallel V_{\parallel e}\right] - 2.61\nu n\left(T_e - \tau T_i\right) \\
&+ \frac{4}{3}\frac{T_e}{B}\left[\frac{7}{2}C\left(T_e\right) + \frac{T_e}{n}C(n) - C(\phi)\right] + \nabla_\parallel\left(\chi_{\parallel e}\nabla_\parallel T_e\right) + D_{T_e}\nabla_\perp^2 T_e \\
&+ s_{T_e} + \frac{n_{\mathrm{n}}}{n}\nu_{\mathrm{iz}}\left[-\frac{2}{3}E_{\mathrm{iz}} - T_e + m_e V_{\parallel e}\left(V_{\parallel e} - \frac{4}{3}V_{\parallel n}\right)\right] \qquad (2.5)\\
\frac{\partial T_i}{\partial t} =& -\frac{\rho_*^{-1}}{B}\left[\phi, T_i\right] - V_{\parallel i}\nabla_\parallel T_i + \frac{4}{3}\frac{T_i}{B}\left[C\left(T_e\right) + \frac{T_e}{n}C(n) - C(\phi)\right] - \frac{10}{3}\tau\frac{T_i}{B}C\left(T_i\right) \\
&+ \frac{2}{3}T_i\left[\left(V_{\parallel i} - V_{\parallel e}\right)\frac{\nabla_\parallel n}{n} - \nabla_\parallel V_{\parallel e}\right] + \nabla_\parallel\left(\chi_{\parallel i}\nabla_\parallel T_i\right) + D_{T_i}\nabla_\perp^2 T_i + s_{T_i} \\
&+ 2.61\nu n\left(T_e - \tau T_i\right) + \frac{n_{\mathrm{n}}}{n}\left(\nu_{\mathrm{iz}} + \nu_{\mathrm{cx}}\right)\left[T_n - T_i + \frac{1}{3}\left(V_{\parallel n} - V_{\parallel i}\right)^2\right] \qquad (2.6)
\end{aligned}$$

where the dynamical variables are normalised in the following way:

- perpendicular lengths are normalised to the reference ion sound Larmor radius, ρ_{s0};
- parallel lengths are normalised to the tokamak major radius, R_0;

- time is normalised to R_0/c_{s0}

where c_{s0} is the reference sound speed $c_{s0} = \sqrt{T_{e0}/m_i}$ and $\rho_{s0} = c_{s0}/\Omega_{ci}$, $\Omega_{ci} = q_i B_0/m_i$ the ion cyclotron frequency.

The numerical diffusion terms, $D_f \nabla_\perp^2 f$, $D_f \nabla_\parallel^2 f$, are added for numerical stability.

The observables of interest of the system are themselves normalised:

- the density n is normalised to the reference value n_0, taken at the separatrix;
- the electron and ion temperatures, T_e and T_i, are normalised to the reference values T_{e0} and T_{i0} (taken again at the separatrix);
- the electron and ion parallel velocities, $V_{\parallel e}$ and $V_{\parallel i}$, are normalised to the reference sound speed c_{s0};
- the magnetic field is normalised to its modulus B_0 at the tokamak magnetic axis;
- the electrostatic potential, ϕ, is normalised to T_{e0}/e;
- the magnetic flux function ψ is normalised to $\rho_{s0} B_0$;

Lastly, we defined the remaining dimensionless parameters that regulate the system dynamics, which are:

- the normalised ion sound Larmor radius, $\rho_* = \rho_{s0}/R_0$,
- the ion to electron reference temperature ratio, $\tau = T_{i0}/T_{e0}$,
- the normalised electron and ion parallel thermal conductivities,

$$\chi_{\parallel e} = \left(\frac{1.58}{\sqrt{2\pi}} \frac{m_i}{\sqrt{m_e}} \frac{(4\pi\epsilon_0)^2}{e^4} \frac{c_{s0}}{R_0} \frac{T_{e0}^{3/2}}{\lambda n_0} \right) T_e^{5/2}$$

  and

$$\chi_{\parallel i} = \left(\frac{1.94}{\sqrt{2\pi}} \sqrt{m_i} \frac{(4\pi\epsilon_0)^2}{e^4} \frac{c_{s0}}{R_0} \frac{T_{e0}^{3/2} \tau^{5/2}}{\lambda n_0} \right) T_i^{5/2}$$

- the reference electron plasma $\beta, \beta_{e0} = 2\mu_0 n_0 T_{e0}/B_0^2$,
- the normalised Spitzer resistivity, $\nu = e^2 n_0 R_0 / \left(m_i c_{s0} \sigma_\parallel\right) = \nu_0 T_e^{-3/2}$, with

$$\sigma_\parallel = \left(1.96 \frac{n_0 e^2 \tau_e}{m_e} \right) n = \left(\frac{5.88}{4\sqrt{2\pi}} \frac{(4\pi\epsilon_0)^2}{e^2} \frac{T_{e0}^{3/2}}{\lambda \sqrt{m_e}} \right) T_e^{3/2}$$

  and

$$\nu_0 = \frac{4\sqrt{2\pi}}{5.88} \frac{e^4}{(4\pi\epsilon_0)^2} \frac{\sqrt{m_e} R_0 n_0 \lambda}{m_i c_{s0} T_{e0}^{3/2}}$$

where λ is the Coulomb logarithm.

This system of equations is again paired with the normalised Poisson and Ampère equations (**??**), which take the form:

$$\nabla \cdot (n \nabla_\perp \phi) = \Omega - \tau \nabla_\perp^2 p_i \tag{2.7}$$

$$\left(\nabla_\perp^2 - \frac{\beta_{e0}}{2} \frac{m_i}{m_e} n \right) V_{\parallel e} = \nabla_\perp^2 U_{\parallel e} - \frac{\beta_{e0}}{2} \frac{m_i}{m_e} n V_{\parallel i} + \frac{\beta_{e0}}{2} \frac{m_i}{m_e} \bar{j}_\parallel \tag{2.8}$$

Solving these last equations entail solving two sparse linear systems at each step, which can be very time-consuming and therefore could require additional simplifications to make the system more efficient.

The differential operators are implemented in GBS in the large aspect ratio approximation, which in normalised units and cartesian coordinates (x, z, y) corresponds to:

$$[\phi, f] = sign(B_0)\left(\partial_y\phi\partial_x f - \partial_x\phi\partial_y f\right) \tag{2.9}$$
$$C(f) = sign(B_0)\partial_y f \tag{2.10}$$
$$\nabla_\parallel f = \partial_y\psi\partial_x f - \partial_x\psi\partial_y f + sign(B_0)\partial_z f \tag{2.11}$$
$$\nabla^2_\perp f = \partial^2_{xx} f + \partial^2_{yy} f \tag{2.12}$$

where the parameter $sign(B_0)$ is introduced to indicate the toroidal magnetic field direction. It is conventionally set to be +1 in the Reversed (unfavourable for H-mode access) cases and -1 in the Forward (favourable for H-mode access) ones. It corresponds to the normalised version of the B_ϕ/B parameter in front of each of the expressions derived for the differential operators in the large aspect ratio approximation discussed in the previous chapter. Furthermore, one can perform the same ordering on some additional operators that appear implicitly in the system (2.1 - 2.6): the parallel laplacian, $\nabla^2_\parallel f$, the curvature of the parallel gradient, $C\left(\nabla_\parallel f\right)$, and the parallel gradient of the curvature, $\nabla_\parallel[C(f)]$. In dimensionless units:

- the parallel laplacian is given by:

$$\begin{aligned}\nabla^2_\parallel f = &\left(\partial_y\psi\partial^2_{xy}\psi - \partial_x\psi\partial^2_{ZZ}\psi\right)\partial_x f + \left(\partial_x\psi\partial^2_{xy}\psi - \partial_y\psi\partial^2_{xx}\psi\right)\partial_y f \\ &+ \left[\left(\partial_y\psi\right)^2\partial^2_{xx} f + \left(\partial_x\psi\right)^2\partial^2_{yy} f - 2\partial_y\psi\partial_x\psi\partial^2_{xy} f\right] \\ &+ 2sign(B_0)\partial_y\psi\partial^2_{xz} f - 2sign(B_0)\partial_x\psi\partial^2_{yz} f + \partial^2_{zz} f + O(\epsilon, \delta)\end{aligned}$$

- the curvature of the parallel gradient by:

$$C\left(\nabla_\parallel f\right) = sign(B_0)\left(\partial_{yy}\psi\partial_x f + \partial_y\psi\partial_{xy} f - \partial_{xy}\psi\partial_y f - \partial_x\psi\partial_{yy} f\right) + \partial_{yz} f + O(\epsilon, \delta)$$

- the parallel gradient of the curvature by:

$$\nabla_\parallel[C(f)] = sign(B_0)\partial_y\psi\partial_{xy} f - sign(B_0)\partial_x\psi\partial_{yy} f + \partial_{yz} f + O(\epsilon, \delta)$$

Equations (2.1 - 2.8) are paired with generalised Bohm-Chodura sheath boundary conditions at the magnetic pre-sheath [29]. The same set of boundary conditions is applied to the walls not containing strike points, with the exception of the condition on the potential, which is set to $\phi = \Lambda T_e/e$, $\Lambda = \Lambda_0 - \sqrt{1 + T_i/T_e}$ as the Poisson equation would be ill-defined if Neumann boundary conditions were set at the four walls of the domain.

From now on Eqs. (2.1 -2.8) will be referred to as *GBS equations* and will be meant in the normalised formulation, unless explicitly stated otherwise. All quantities of interest will similarly be considered as normalised.

2.1.2 Boussinesq approximation

One approximation that is taken into consideration many tokamak boundary turbulence simulations is the Boussinesq one (see [30, 28, 26, 9]). It consists in neglecting the spatial and time dependency of the density in the polarisation velocity component of the Poisson equation, i.e.:

$$\nabla\cdot(n\nabla_\perp\phi) \simeq n\nabla^2_\perp\phi$$

This greatly simplifies the numerical treatment of the Poisson equation (Eq. 2.7), as it takes the form:

$$\nabla_\perp^2 \phi = \omega - \tau \nabla_\perp^2 T_i$$

and the vorticity equation (Eq. 2.2) reduces to:

$$\frac{\partial \omega}{\partial t} = -\frac{\rho_*^{-1}}{B}[\phi, \omega] - V_{\parallel i}\nabla_\parallel \omega + \frac{B^2}{n}\nabla_\parallel j_\parallel + \frac{2B}{n}C\left(p_e + p_i\right) + \frac{B}{3n}C\left(G_i\right) + D_\omega \nabla_\perp^2 \omega - \frac{n_\mathrm{n}}{n}\nu_{cx}\omega$$

While it is a useful approximation since it reduces the computational time, recasting the term in the Poisson equation into a constant Laplacian instead of needing to be recomputed at each time, but it does not necessarily hold in general, especially in edge simulations, as steep density gradients can appear across the separatrix and in general in the Scrape-Off Layer ([9]).

We take into account the possible effect of this approximation by comparing the results of simulations run taking it into account and others which do not, making the appropriate considerations in each case to account for the physical consequences of such an approximation for the phenomenon we are examining.

2.2 Simulation data

Having defined what the general simulation tool looks like, we can now take a look at the specific simulations taken in exam.

In the present thesis simulation data run using GBS has been employed, and has been analysed through the post-processing tools present in the `gbspy` library, from which routines were taken and modified to accommodate our particular cases of interest.

Our dataset is comprised of 19 simulations in total, divided into 3 categories depending on the magnetic geometry taken into account (Table 2.1):

1. Snowflakes
2. Single Nulls [7]
3. Single Nulls (Divrec [31])

Of these, 9 are 3D simulations and 8 are 2D, that is are run considering only one poloidal plane for the evolution of the system. The latter will entail a higher coefficient for the spurious perpendicular diffusion terms, as they mimic the effect of turbulence.

For each specific magnetic configuration we will have both the case for forward toroidal magnetic field (labelled as "Forward B") and reversed toroidal magnetic field (assumed as default), with the only exception of the 3D Snowflake Single Null, which does not have a respective Forward case. The magnetic configurations (two cases for each type) are shown in Fig. 2.1, in which the time and toroidally averaged electric potential heatmap is shown, with the separatrix highlighted in white. The outer divertor leg is highlighted in black, as we will focus our analysis on that particular region for most of the present thesis.

Out of the whole dataset, some particular cases are important to highlight:

- there are 4 simulations (2 Snowflakes and 2 Single Nulls (Divrec)) which are run considering the Boussinesq approximation (§2.1.2), labelled accordingly;
- there are 2 simulations (denoted with η_0), in which we consider a temperature dependent Spitzer thermal conductivity ($\chi_{\parallel,e} = \eta_0 T_e^{5/2}\mathbb{I}[T_e < 1] + \eta_0 \mathbb{I}[T_e \geq 1]$); for all others, the thermal conductivity will be taken as constant;

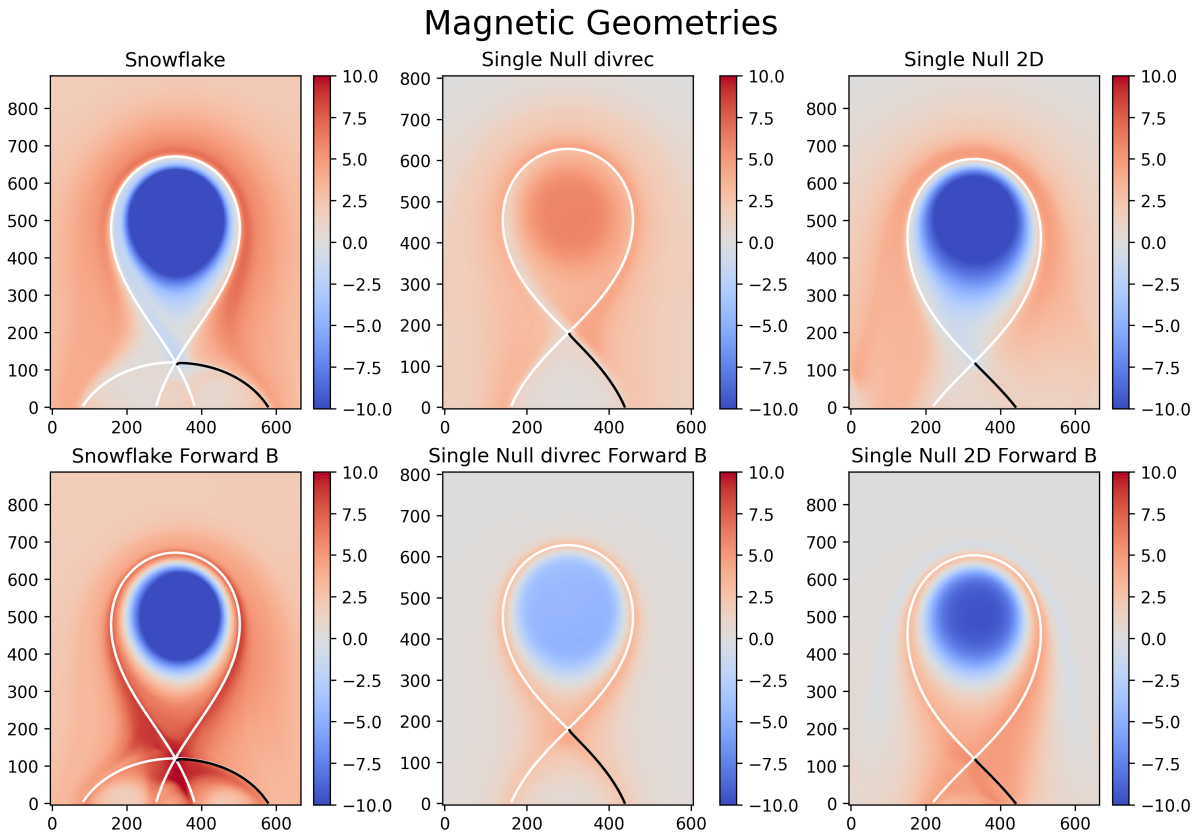

Figure 2.1: Magnetic Configurations
Time and toroidally averaged electric potential for the given magnetic geometries. The separatrix is highlighted in white and the outer divertor leg in black. Time averages were performed over 10 time units.

- there are 5 simulations which are run using a much lower mass ratio (the first 4 Snowflakes and the 3D Snowflake Single Null), which is expected to help achieving larger time steps; even though the presented mass ratio is unphysical, they represent an interesting comparison to determine the role of this parameter in the verification of some important relations;

- correspondingly, there are 2 Snowflake simulations labelled as "Reloaded", which are obtained using an accurate mass ratio starting from the results of the 3D Snowflake simulations, and thus are run for much less time.

All the information is summarised in Table 2.1. For the numerical values of the parameters not specified there we refer to Table 1 in Appendix A.

Now it is possible to make some preliminary considerations about the parameter range we find ourselves in.

The first parameter to be examined is the Spitzer resistivity, as we are interested in the electric potential profile along the outer divertor leg and the latter is heavily influenced by the former. If we consider the full expression for the resistivity previously defined:

$$\nu = \nu_0 T_e^{-3/2}$$

we can see the profile of the Spitzer resistivity along the leg. From Fig. 2.2 we can see two very important things:

- The range of values do not seem to change significantly from reversed to forward B cases (it stays within the same order of magnitude, when not nearly the same);

simulation (labels)	B_t	**inv. norm. ion sound Larmor radius** (ρ_*^{-1})	**mass ratio** (m_i/m_e)	**resistivity** (ν_0)
Snowflakes				
Snowflake with Boussinesq	Reversed	700	200.0	0.2
Snowflake with Boussinesq Fw B	Forward	700	200.0	0.2
Snowflake	Reversed	700.0	400.0	0.2
Snowflake Fw B	Forward	700.0	400.0	0.2
Snowflake 2D	Reversed	500.0	1836.0	0.1
Snowflake 2D Fw B	Forward	500.0	1836.0	0.1
Snowflake Reloaded	Reversed	700.0	1836.0	0.1
Snowflake Reloaded Fw B	Forward	700.0	1836.0	0.1
Single Nulls				
Single Null	Reversed	700.0	200.0	0.4
Single Null 2D	Reversed	700.0	1836.0	0.1
Single Null 2D Fw B	Forward	700.0	1836.0	0.1
Single Nulls (Divrec)				
Single Null Divrec	Reversed	500.0	1836.0	0.1
Single Null Divrec Fw B	Forward	500.0	1836.0	0.1
Single Null Divrec η_0	Reversed	494.0	1836.0	0.08
Single Null Divrec η_0 Fw B	Forward	494.0	1836.0	0.08
Single Null Divrec with Boussinesq	Reversed	500.0	1836.0	0.1
Single Null Divrec with Boussinesq Fw B	Forward	500.0	1836.0	0.1
Single Null Divrec 3D	Reversed	500.0	1836.0	0.1
Single Null Divrec 3D Fw B	Forward	500.0	1836.0	0.1

Table 2.1: simulation parameters

- the only normalised Spitzer resistivity parameter ν_0 that is significantly higher than the others is that of the 3D Single Null case, which could affect the results.

Another parameter of interest for the system are the diffusion coefficients for temperature and density. While the parallel thermal diffusion (thermal conductivity) is indeed present in the physical model, the parallel diffusion for the density and the perpendicular diffusion in both cases are introduced only for numerical stability, but nevertheless affect the data, as they are especially significant in the 2D simulations. In these cases, in fact, the perpendicular diffusion terms are meant to reproduce the effect of turbulent transport, which would not be present otherwise. The parallel transport terms are also larger, as the 2D simulations are more numerically stable and thus can handle them.

Lastly, we want to comment on the inverse normalised ion sound Larmor radius of our simulations. We will consider one large enough to allow us to use all of the corresponding approximations (drift ordering), while still considering small devices (we are in the 500-700 range for ρ_*^{-1}, where the one expected for ITER is in the order of 10^4).

2.3 A brief digression on notation

As the following chapters contain many analytic derivations, we thought it necessary to specify the main conventions that will be used throughout the present thesis, so as to make the reading more fluid; when necessary, additional notation conventions may be added.

Since most of the analysis will focus on the profiles along the divertor leg (Fig. 2.1), we start by defining properly our domain of interest. Given a field line in the full 3D domain following the path along the separatrix which connects the outer target to the X-point, we consider its projection onto

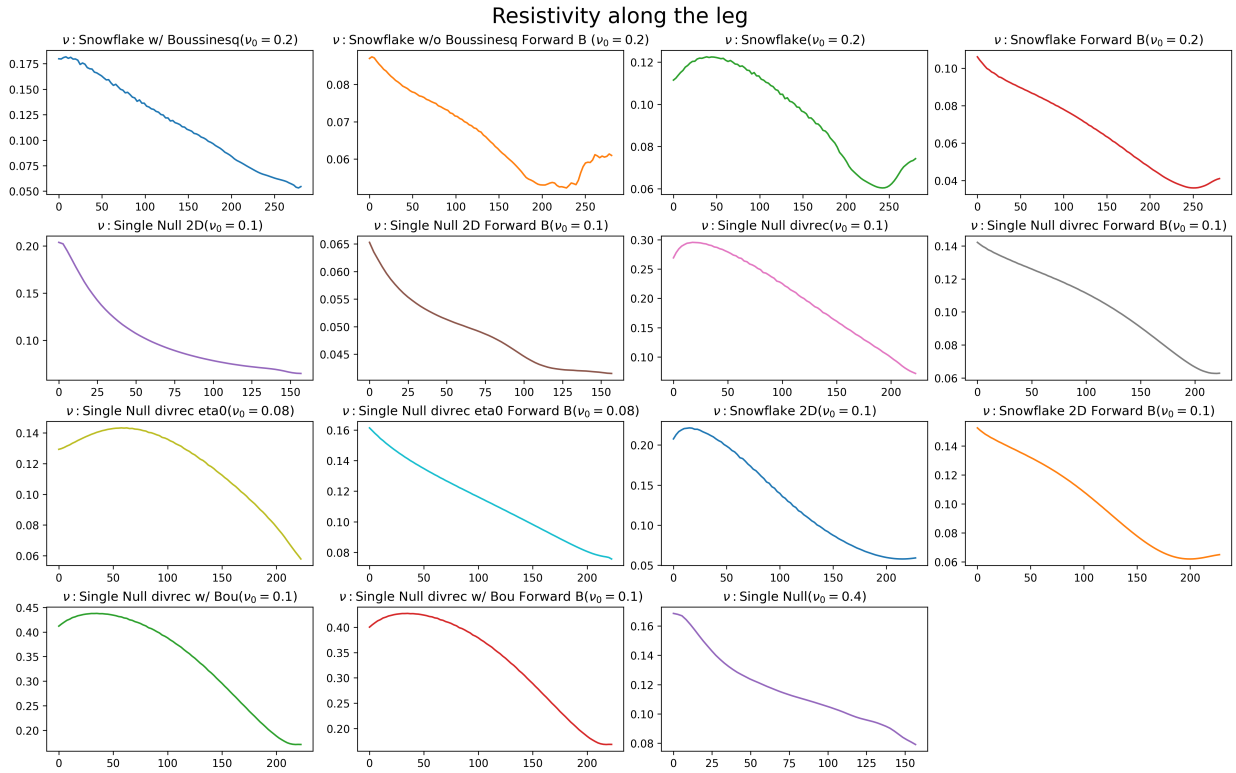

Figure 2.2: Spitzer resistivity profiles along the outer divertor leg
The Spitzer resistivities are plotted against the poloidal projection coordinate σ. The x-labels are omitted because of spatial constraints.

the poloidal cross-section. Given a cartesian coordinate system (x, z, y), we take a parametrisation $\sigma(x, y)$ of such projection, assumed to be such that lengths are expressed in normalised $[\rho_0]$ (ion sound Larmor radius) units. The parallel coordinate is defined as:

$$s(\sigma) := \int_{\text{target}}^{\sigma} \frac{1}{|B_{pol}|} d\sigma$$

which is now a parametrisation of the original field line, representing the connection length in normalised $[R_0]$ (major radius) units. Thus the magnetic geometry is incorporated in the definition of the parallel coordinate.

2.3.1 Differential operators

We proceed to rewrite the GBS differential operators in terms of the parametrisation we have obtained for the curve. That is, given the poloidal magnetic flux function ψ, one starts by defining the parallel and perpendicular directions of the poloidal projections of the flux surfaces, indicated respectively by $\nabla^T\psi$ and $\nabla\psi$. In the large aspect ratio approximation and in axisymmetric configurations, for any given field f, the corresponding poloidal gradients associated to these directions can be defined as:

$$\tilde{\partial}_{\parallel} f := \frac{1}{|B_{pol}|} \left(\partial_y \psi \partial_x f - \partial_x \psi \partial_y f\right) = \frac{1}{|B_{pol}|} \nabla_{\parallel} f$$
$$\tilde{\partial}_{\perp} f := \frac{1}{|B_{pol}|} \left(\partial_x \psi \partial_x f + \partial_y \psi \partial_y f\right) = \frac{1}{|B_{pol}|} \nabla_{\perp} f$$

where the last gradients are now meant to be understood as the actual GBS differential operators parallel and perpendicular to the flux surfaces and thus rescaled in terms of the connection length. In

all the following we will consider the gradients with the $\sim$ superscript ($\tilde{\partial}_{\parallel,\perp}$) indicating the lengths in the poloidal projection parametrisation and the ones without ($\partial_{\parallel,\perp}$) following the parametrisation along the field lines (i.e., considering the $1/|B_{pol}|$ factor). Moreover since as previously stated most of the analysis will focus on the profiles along the divertor leg Fig 2.1, we will equivalently denote the parallel gradient as:

$$\partial_s f := -\partial_\parallel f \simeq -\nabla_\parallel f$$

where s is the previously defined parallel coordinate. The minus sign is due to the fact that the parallel gradient is defined in GBS as going in the *X-point* $\rightarrow$ *target* direction, while it's more convenient to consider the opposite direction in our analysis, since it is easier to measure most quantities of interest at the target and thus initial conditions are well defined there.

2.3.2 Integration paths

Analogously to the case of differential operators, we have the need to define what it means to *integrate* in our particular framework.

In particular we consider that, given a field f and a parametrisation σ of the poloidal projection of the divertor leg, we define the integral along the leg in the following way:

$$\int_{leg} f(s)ds = \int_{\text{target}}^{\text{X-pt}} \frac{1}{|B_{pol}|} f(\sigma)d\sigma$$

where s is the previously defined parallel coordinate. All integrals are considered to be along field lines, thus with a scaling of $1/|B_{pol}|$ due to the curve parametrisation, and will be considered to be taken in the direction *target* $\rightarrow$ *X-point*, as above.

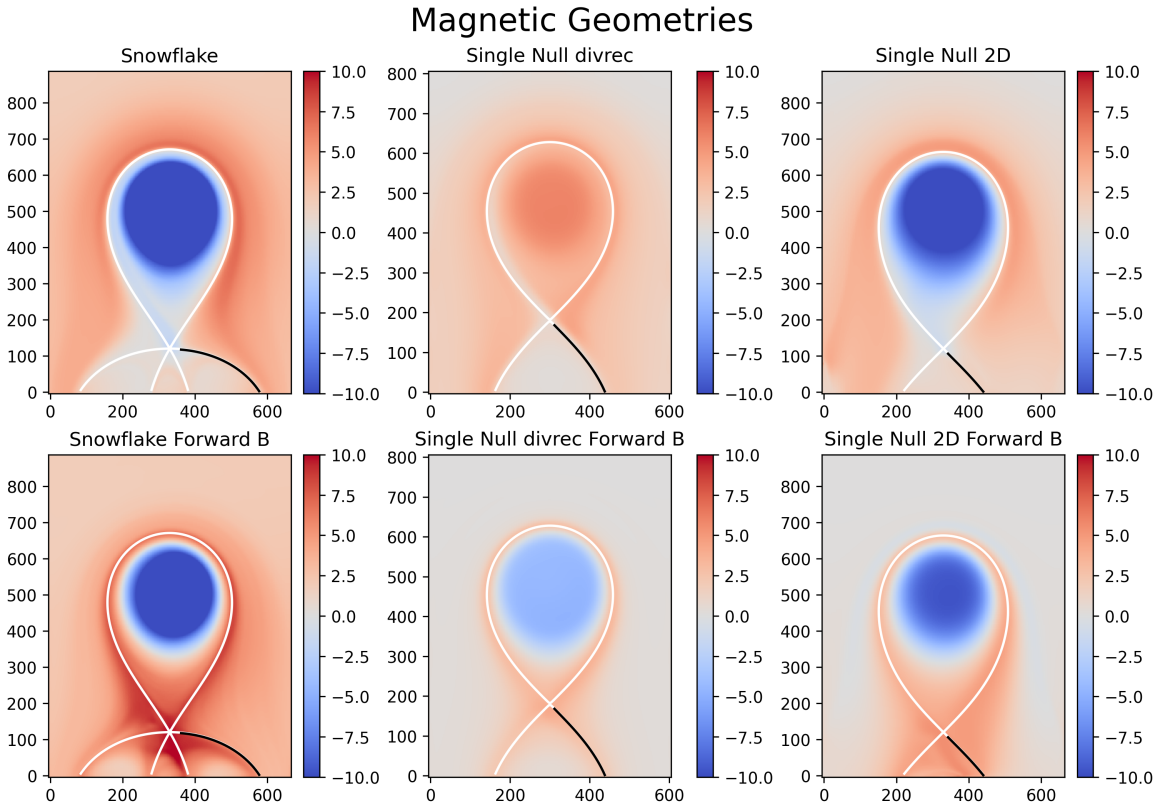

Figure 2.3: Magnetic Configurations: cutoffs

Due to the way we define the parallel coordinate s, it diverges at the X-point: we will thus consider a cutoff parameter (Fig. 2.3) when evaluating it in the code, as we only have complete information about the points in the poloidal plane, but we would have only few sparse data points as we get closer to the X-point. The corresponding cutoff parameter will be smaller for the Single Null cases than in the Snowflake one, as we have a stronger flux expansion in the latter (due to the fact that $|B_{pol}| \sim |\boldsymbol{r} - \boldsymbol{r}_{X-pt}|^2$ in Snowflake configurations, rather than the $|B_{pol}| \sim |\boldsymbol{r} - \boldsymbol{r}_{X-pt}|$ law we have in Single Null configurations close to the X-point). In practice, the value is chosen so to exclude the last n poloidal points recovered from the routine `get_line` from the `gbspy` library, with $n = 10$ in the Snowflake cases, $n = 5$ in the Single Nulls: it is chosen so that the parallel coordinate stays within the same order of magnitude for the two cases ($s \in (30, 40)$ range for SF, $(10, 20)/(20, 30)$ for SN). It will affect some of the numerical fits, making them more informative, as otherwise there would be skewed results as they would be fit on points accumulated at the beginning of the line. The particular choice of this cut-off does not affect the theoretical model, as what we are ultimately interested in is not the description of the profiles *exactly* at the X-point, but rather in its vicinity.

Chapter 3

Integrating the electric potential along the divertor leg: Ohm's law

Now that all the theoretical and computational tools that will be employed in this analysis have been properly described, we can proceed to present the obtained results.

As anticipated, the aim of the present thesis is to investigate the potential structures forming around the X-point. In order to do so we try to find a description of the potential profile along the outer divertor leg (Fig. 2.1). In particular, we start from previously developed analysis and try to improve on those results to recover a more informative description of the phenomenon.

3.1 Previous results for the potential profile along the divertor leg

The formation of a potential structure around the X-point has been observed in experimental devices, and has been investigated in [20] using 2D simulations run with SOLPS-ITER. As previously mentioned, a scaling relation involving the values of density, temperature and potential at the target and at the X-point was obtained. In order to do so, the following simplifying assumptions were made:

1. a simplified geometry (straight divertor leg) is considered;
2. gradients are assumed to be constant along the integration paths (divertor leg), so that all the profiles of interest are linear;
3. flux expansion is assumed to be constant along the leg.

Considering sheath boundary conditions at the target and the parallel electron momentum balance in the form of a generalised version of Ohm's law:

$$E_{\parallel} = \eta_{\parallel} j_{\parallel} - \frac{\nabla_{\parallel} p_e}{e n_e} - 0.71 \frac{\nabla_{\parallel} T_e}{e}$$

the mechanism that is assumed to drive the potential well/hill formation in reversed/forward magnetic field conditions is the Pfirsch-Schlüter current:

$$\begin{aligned} j_{\parallel} &= j^{PS} + j^{\parallel,XP} \\ j^{PS} &= \mp \frac{2p}{B_t^0 R_0} \frac{L_{XP}}{\lambda_j} \left| \frac{B}{B_\theta} \right| \cos\alpha \end{aligned} \tag{3.1}$$

where α is the pitch angle of the leg, R_0 is the major radius, B_t^0 is the toroidal field at the midplane, B_θ is the poloidal field, L_{XP} and λ_j are respectively the width and the height of a closed volume extending from target to X-point in the private flux region where the parallel current doesn't change

sign. The Pfirsch-Schlüter current is defined as the part of the parallel current which closes the diamagnetic current (i.e., cancels its non-divergence-free component), while the other component of the parallel current would represent charge sharing between the divertor legs due to asymmetries in the temperature or density; the latter is assumed to be null.

This allowed to recover a scaling relation between potential, density and temperature:

$$\frac{e\delta\phi}{T_e^{XP}} \approx \frac{2en_e^{XP}\eta_\parallel}{B_t^0}\frac{L_{XP}^2}{\lambda_j R_0}\left|\frac{B}{B_\theta}\right|^2 \cos\alpha + 1.71 = \\ = m\cdot\frac{n_e^{XP}}{(T_e^t)^{3/2}} + 1.71,$$

where the superscripts t, XP represent the values measured at the target and the X-point respectively, m is the proportionality constant and $\delta\phi = \phi^t - \phi^{XP}$. The predicted results were compared to Single Null configurations run in 2D [18], although the simulations include drift effects not previously included in SOLPS-ITER, and they show good agreement with the data in the reversed case, but the effect is overestimated by a factor 2-3 in the forward case.

The simplifying assumptions previously discussed allowed to recover a model which gives an interesting description of the phenomenon, although it relies on the measurement of quantities at X-point, which is experimentally difficult to obtain. Additionally, it was observed in GBS simulations that the potential well/hill effect seemed to be of larger magnitude in the case of Snowflake divertor configurations compared to single null configurations at similar parameters, leading one to wonder about the effect of the magnetic geometry, which is not considered in the previous paper.

The goal would be to expand on the ideas presented here, by including:

- drift effects, as they are more relevant in GBS simulations;
- flux expansion effects, as the hill/well effect has been observed to be much stronger in the Snowflake simulations.

We moreover want to only consider quantities measured at the target, which would be easier to obtain experimentally.

3.2 Ohm's law

We consider, analogously to the procedure in [20], a generalised version of Ohm's law along the leg, which in the stationary case is recovered from the parallel electron velocity equation:

$$\frac{\partial U_{\parallel,e}}{\partial t} = -\frac{\rho_*^{-1}}{B}[\phi, V_{\parallel,e}] - V_{\parallel,e}\nabla_\parallel V_{\parallel,e} + \boxed{\frac{m_i}{m_e}\left(+\nabla_\parallel\phi + \nu j_\parallel - \frac{1}{n}\nabla_\parallel p_e - 0.71\nabla_\parallel T_e - \frac{2}{3n}\nabla_\parallel G_e\right)} + D_{V_{\parallel,e}}\nabla_\perp^2 V_{\parallel,e} \tag{3.2}$$

By assuming quasi-steady case and considering that the term associated to $\frac{m_i}{m_e}$ to be dominating and thus needing to be set to zero to maintain the balance, a relation between the terms within the frame is obtained, setting the potential along the leg (Fig. 2.3)

Such a balance is recovered in the differential case at a relative level, that is rescaling by the maximal term:

$$0 \simeq \sum_j \tilde{a}_j, \quad \tilde{a}_i := \frac{a_i}{\max_j\{|a_j|\}}$$

and $\{a_j\}_j$ are the terms in the r.h.s. of the equation. One finds an agreement within 10% for the simulations with realistic mass ratio (§2.2), as can be seen in Fig. 3.1. The reason why a relative

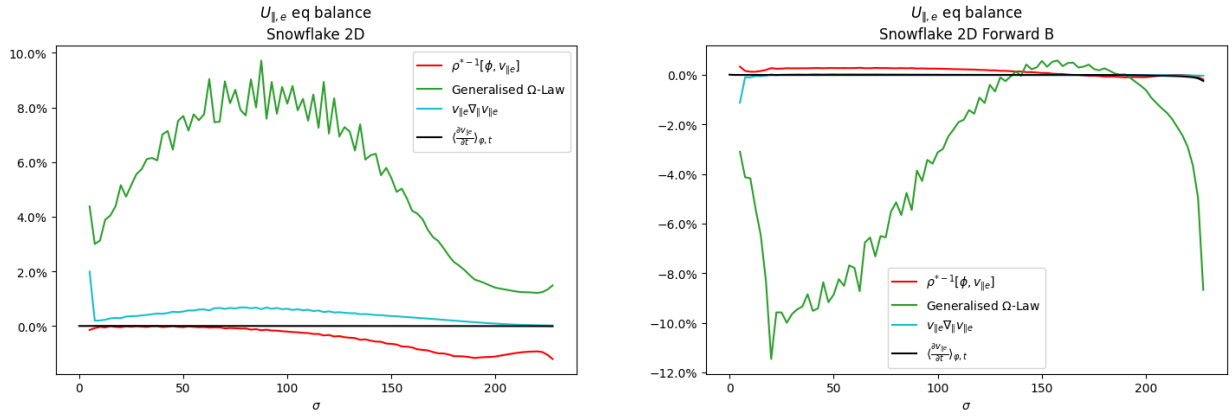

(a) Reversed B **(b)** Forward B

Figure 3.1: Relative Balance for the $U_{\parallel,e}$ equation
The terms in the labels correspond to those in Eq. (3.2), where the "Generalised Ohm's Law" corresponds to the framed term and the l.h.s. is considered time and poloidaly averaged.

balance is considered is mainly to reduce the effect of the fluctuations and of the interpolation error as the profile is taken along the leg. Moreover the balance is verified in the integral case, with a good agreement in all cases.

Therefore one can now set:

$$-\nabla_\parallel \phi \simeq \nu j_\parallel - \frac{1}{n}\nabla_\parallel p_e - 0.71\nabla_\parallel T_e - \frac{2}{3n}\nabla_\parallel G_e \tag{3.3}$$

$$\Rightarrow \phi\Big|_{leg} \simeq \int_{leg} \left[\nu j_\parallel - \frac{1}{n}\nabla_\parallel p_e - 0.71\nabla_\parallel T_e - \frac{2}{3n}\nabla_\parallel G_e\right] ds =$$

$$\simeq \int_{\text{target}}^{\text{X-pt}} \left[\nu j_\parallel - \frac{1}{n}\nabla_\parallel p_e - 0.71\nabla_\parallel T_e - \frac{2}{3n}\nabla_\parallel G_e\right] \frac{1}{|B_{pol}|} d\sigma$$

as we are ultimately interested in integrating the potential profile along the divertor leg (§2.3).

In doing so a couple of observations can be made about the terms present in the balance, especially comparing the differential and the integral cases for forward versus reversed magnetic configurations. First of all, it seems that, contrary to [20]'s prediction, the terms setting the potential profile in the forward and reversed case are different: in the reversed case the dominating term is the one associated to the parallel current, whereas the dominating ones in the forward case are the thermoelectric currents. This is not due to a possible difference in the resistivities, as they do not differ much in the reverse versus forward cases (§2.2). What is however observed is a sign switch between the two cases, as predicted in the aforementioned paper, as is shown in Fig. 3.2. Lastly we note that the gyroviscuous term $\frac{2}{3n}\nabla_\parallel G_e$ is non-zero only very close to the target in the differential formulation, and is therefore negligible at an integral level since, given λ_{G_e} the length of the support of $\nabla_\parallel G_e$, in the integral formulation we would obtain a term of the order $O\left(\lambda_{G_e}\nabla_\parallel G_e/|B_{pol}|\right) \ll 1$, as the connection length scaling $1/|B_{pol}| \ll 1$ in this region (Fig. 3.3).

Given that a trend in the behaviour of the potential in our cases seems to emerge, we want now to proceed to study more in depth the individual terms making up the equation. In particular our goal would be to find a description for them in terms of other GBS-evolved quantities which could be measured at the target (e.g. density, electron temperature).

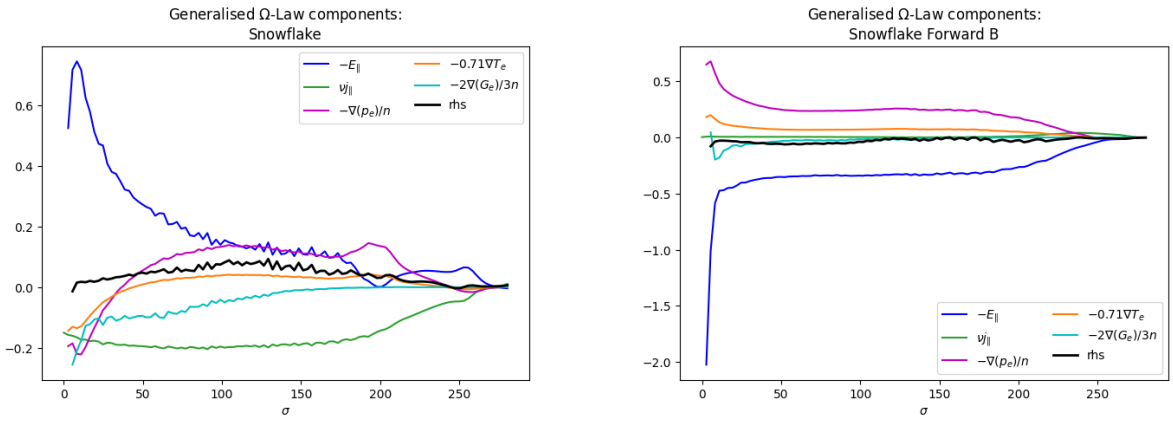

(a) Reversed B **(b)** Forward B

Figure 3.2: Generalised Ohm's law components
The components of the generalised Ohm's law have been plotted against the poloidal parallel coordinate σ. The term denoted as "rhs" is the sum of all of the components of Eq. (3.3)

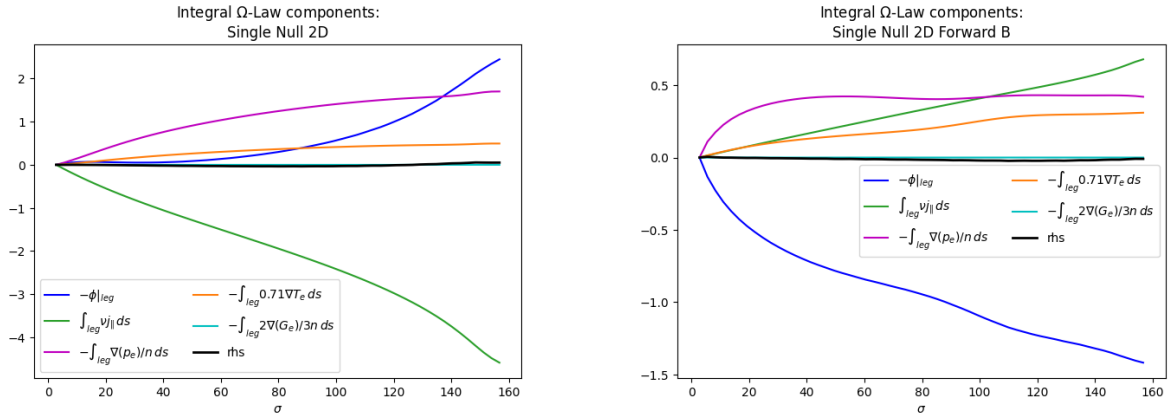

(a) Reversed B **(b)** Forward B

Figure 3.3: Integral Generalised Ohm's law

3.3 Parallel current closure

Taking an approach akin to that in [20], one can try to find a closure for the parallel current in terms of the other currents present in the Scrape-Off Layer. The way this balance is achieved is through the vorticity equation.
The normalised vorticity equation in GBS is given by:

$$\frac{\partial \Omega}{\partial t} = -\frac{\rho_*^{-1}}{B}\nabla\cdot[\phi,\boldsymbol{\omega}] - \nabla\cdot\left(V_{\parallel i}\nabla_\parallel\boldsymbol{\omega}\right) + B^2\nabla_\parallel j_\parallel + 2BC(p_e+\tau p_i) + \\ + \frac{B}{3}C(G_i) + D_\Omega\nabla_\perp^2\Omega + D_{\Omega,\parallel}\nabla_\parallel^2\Omega$$

which, in the Boussinesq approximation (§2.1.2), reduces to:

$$\frac{\partial \omega}{\partial t} = -\frac{\rho_*^{-1}}{B}[\phi,\omega] - V_{\parallel i}\nabla_\parallel\omega + \frac{B^2}{n}\nabla_\parallel j_\parallel + \frac{2B}{n}C(p_e+p_i) + \\ + \frac{B}{3n}C(G_i) + D_\omega\nabla_\perp^2\omega + D_{\omega,\parallel}\nabla_\parallel^2\omega$$

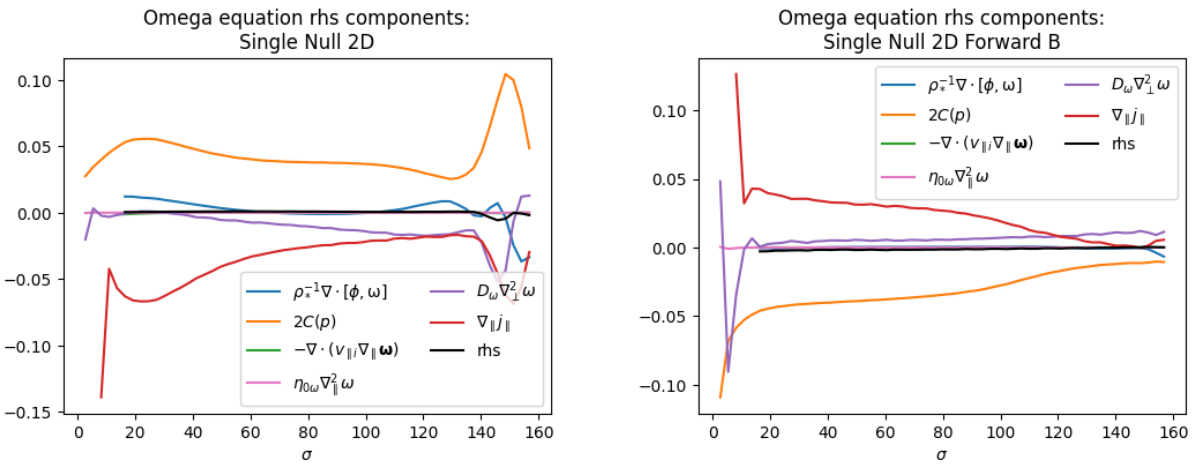

(a) Reversed B **(b)** Forward B

Figure 3.4: Vorticity Equation
The different components of the vorticity equation are represented in the reversed and forward case. The perpendicular diffusion terms, although large, are not considered in the determination of the dominant terms as they are considered to be spurious (§2.2).

The terms highlighted in colour are the dominating ones, as one can see in differential form in Fig. 3.4 and in integral form in Fig. 3.5; then, in a steady state scenario, the equation is reduced to:

$$\nabla_\parallel j_\parallel \simeq -\frac{2}{B}C(p_e+\tau p_i)+\frac{\rho_*^{-1}}{B^3}\nabla\cdot[\phi,\boldsymbol{\omega}] \qquad \text{(without Boussinesq)}$$

$$\nabla_\parallel j_\parallel \simeq -\frac{2}{B}C(p_e+p_i)+n\frac{\rho_*^{-1}}{B^3}[\phi,\omega] \qquad \text{(with Boussinesq)}$$

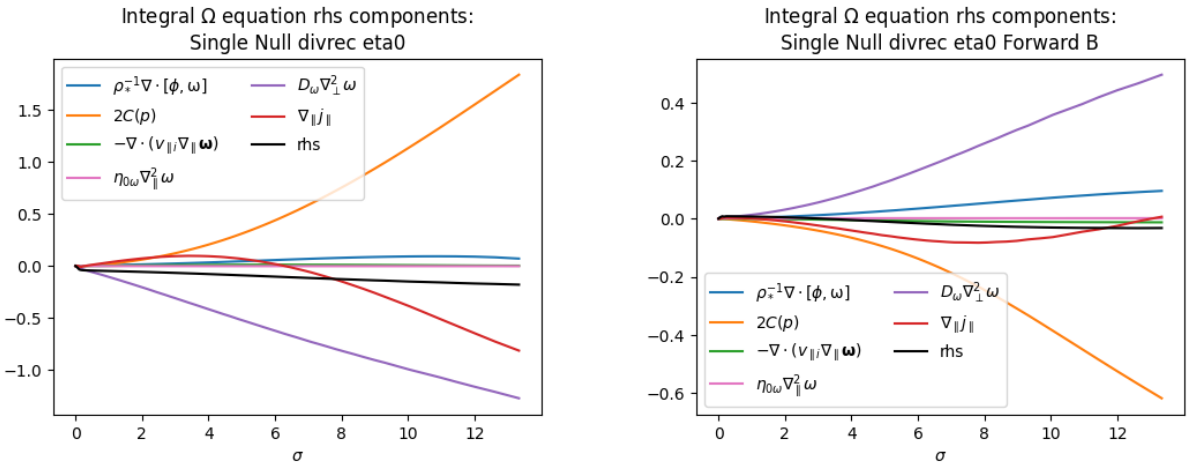

(a) Reversed B **(b)** Forward B

Figure 3.5: Integral Vorticity Equation

They represent, respectively, the terms associated to divergence of the $E\times B$ (first one in red), the parallel (the one in green), and the diamagnetic (second one in red) drift velocities.

Thus, in the same spirit as [20], the terms that cancel out in divergence form are assumed to be equal when integrated, so that one can substitute the parallel current term in Ohm's Law with the

corresponding integrated terms, e.g. in the case without the Boussinesq approximation:

$$j_{\parallel}\Big|_{leg} = -\int_{leg} \nabla_{\parallel} j_{\parallel} ds \simeq \int_{leg} \Big[2C(p_e + \tau p_i) - \rho_*^{-1} \nabla \cdot [\phi, \omega]\Big] ds$$

where the fact that in normalised GBS units $B = 1$ has been considered.

Spurious diffusion terms, which are present for numerical stability, will be considered separately.

Now that a satisfactory description for the parallel current, which is then removed from our system of equations, the aim is to find an appropriate description for the density and the temperature profiles along the leg, as they become the only remaining unknowns in Ohm's law: as we will see, this will prove to be a less than trivial matter.

Chapter 4

Density and Temperature profiles: the refined two-point model

4.1 GBS equations for n and T_e and the two-point model

We start by empirically observing that, at least at a first approximation, there seems to be a scaling relation between the density and the electron temperature profiles along the divertor leg, as shown in a few examples in Fig. 4.1. This is shown to hold up to a 10% precision when considering the same fitting procedure for points on different flux surfaces around the leg area (Fig. 4.2).

Our first attempt to explain this behaviour stems from the normalised GBS equations for the density and the electron temperature:

$$\begin{aligned}\frac{\partial n}{\partial t} =& -\frac{\rho_*^{-1}}{B}[\phi, n] + \frac{2}{B}\big[C(p_e) - nC(\phi)\big] - \nabla_\parallel(nv_{\parallel,e}) + D_n\nabla_\parallel^2 n + D_{n,\perp}\nabla_\perp^2 n + S_n \\ \frac{\partial T_e}{\partial t} =& -\frac{\rho_*^{-1}}{B}[\phi, T_e] + \frac{4T_e}{3B}\left[\frac{7}{2}C(T_e) + \frac{T_e}{n}C(n) - C(\phi)\right] - \nabla_\parallel(T_e v_{\parallel,e}) + \frac{2}{3}0.71T_e\frac{\nabla_\parallel j_\parallel}{n} + \frac{T_e}{3}\nabla_\parallel v_{\parallel,e} + \\ &+ \nabla_\parallel(\chi_{\parallel,e}\nabla_\parallel T_e) + D_{T_e,\perp}\nabla_\perp^2 T_e + S_{T_e} \end{aligned} \tag{4.1}$$

where, as usual, the neutral interactions have been neglected.

While in principle the study of these equations along the leg is the most complete description one has of these profiles, what is instead interesting iS what these two equations have in common, as they have similar terms appearing due to similar structures of the conservation laws they come from (§1.3.2).

The naïve approach would be to try and apply the so called *two-point model* ([10], [6]): this model considers a simplified case in which perpendicular dynamics and magnetic field variations can be neglected, obtaining a 1D description relating quantities at an upstream location (which in our case of interest would be at the X-point) to one downstream (e.g. the target). Given $\lambda_\perp$ the length scale of variation in the direction perpendicular to the magnetic field and $L_\parallel$ the characteristic length in the parallel direction, the key assumption can be written as:

$$\mathbf{V}_\perp \ll \frac{\lambda_\perp}{L_\parallel}\mathbf{V}_\parallel$$

where $\mathbf{V} = \mathbf{V}_\perp + \mathbf{V}_\parallel$ is the average velocity defined as in (§1.3.1) and is decomposed into its perpendicular and parallel components. The perpendicular scale of variation of the magnetic field L_b is also assumed to be small $L_b \ll L_\parallel$, which would be equivalent to considering a straight field line. This assumptions, combined with energy conservation laws, allow to derive scaling relations of the quantities involved, in particular in the two fundamental limits (*sheath limited*, *conduction-limited*). We find this description to be insufficient in our particular case, as the power-law dependencies recovered

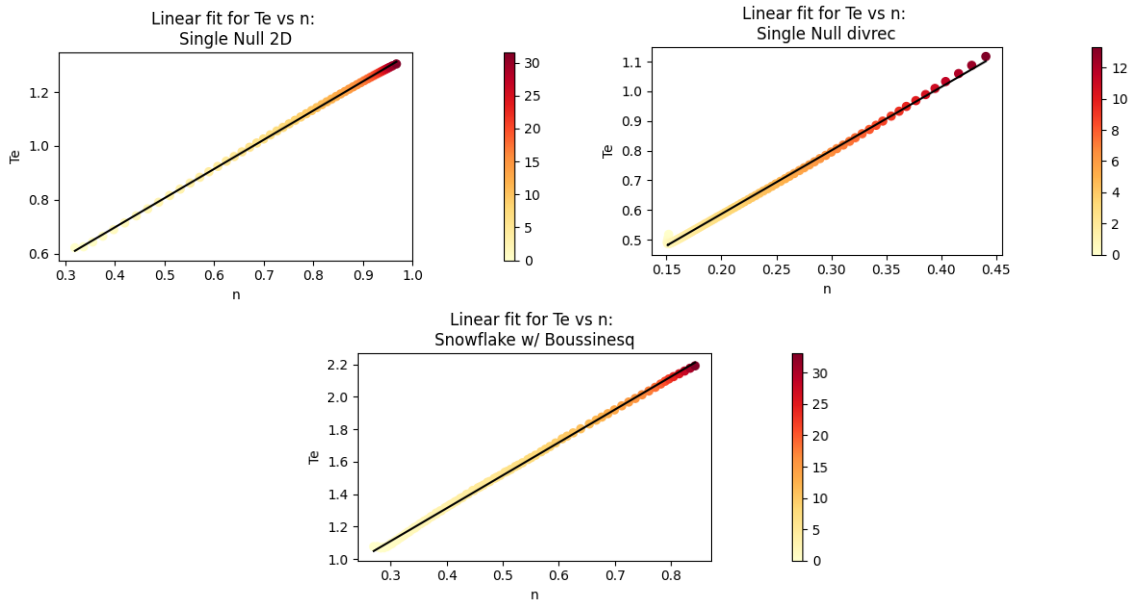

Figure 4.1: n **vs** T_e **scaling**
n vs T_e scaling for different magnetic geometries. The corresponding parallel coordinate is shown in the colorbar on the side.

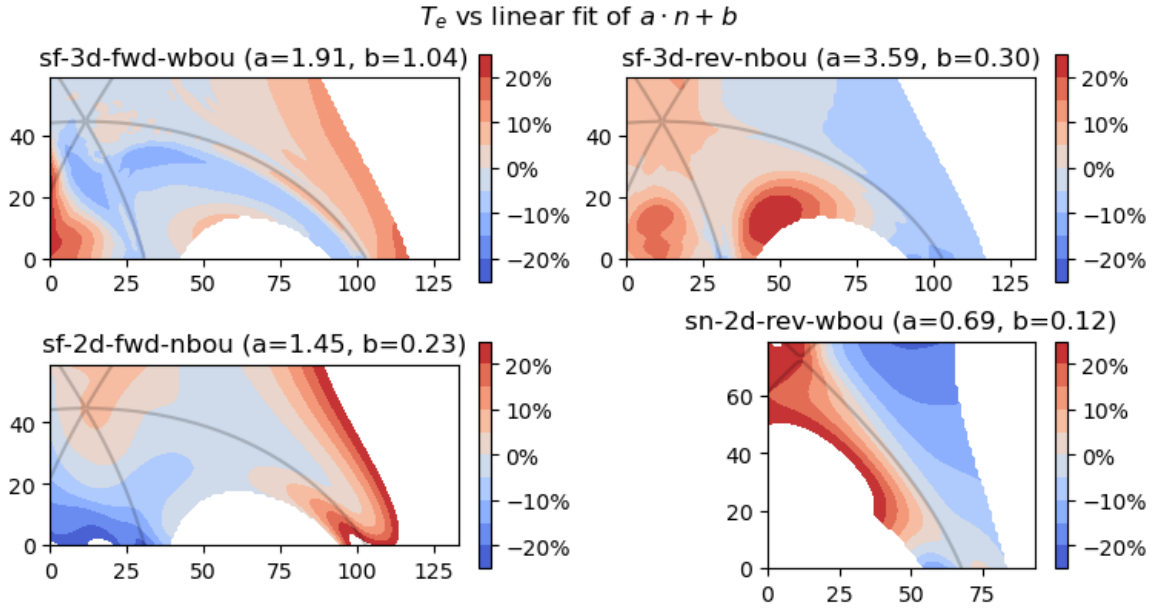

Figure 4.2: n **vs** T_e **scaling: area around the leg**
T_e is compared to a linear fit of the type $an + b$ by estimating the relative error around the leg area in different configurations. Labels are abbreviated as such: "sf" = *Snowflake*, "sn" = *Single Null (Divrec)*, "fwd" = *Forward B*, "rev" = *Reversed B*, "wbou/nbou" = *with/without Boussinesq approximation.*

for the density and temperature in terms of the parallel coordinate do not match the ones shown in the data (Fig. 4.4), as one would expect a power $\delta = 2/7, 0$ in the respective limits for $n(s) - n_t \propto s^\delta$. This could be due to the fact that the first hypothesis for the application of such a simplified model fails in our case because of drift-ordering ([6], chapter 5.5).

Note that, additionally, the two equations do not present the same functional form in the dominant

terms. Given a sequence of differential operators $\{D_i\}_{i=0}^m$ and corresponding coefficients $\{\alpha_i\}_{i=0}^m$, one could try to write the two equations in the same form as:

$$\frac{\partial n}{\partial t} = \left[\sum_{i=0}^{m} \alpha_i D_i\right] n + r_n$$
$$\frac{\partial T_e}{\partial t} = \left[\sum_{i=0}^{m} \alpha_i D_i\right] T_e + r_{Te}$$

where the remainder terms r_n, r_{Te} are expected to be negligible with respect to the others. That is however shown not to be the case, as one can see in Fig. 4.3: the terms that differ between the two equations are found to be non-negligible along the leg.

One has to take a different approach in order to recover information from the system. In particular a refinement of the *two point model* will be considered: the perpendicular dynamics will be approximated, but not neglected, in order to obtain a simplified, but nevertheless informative, description.

(a) n equation

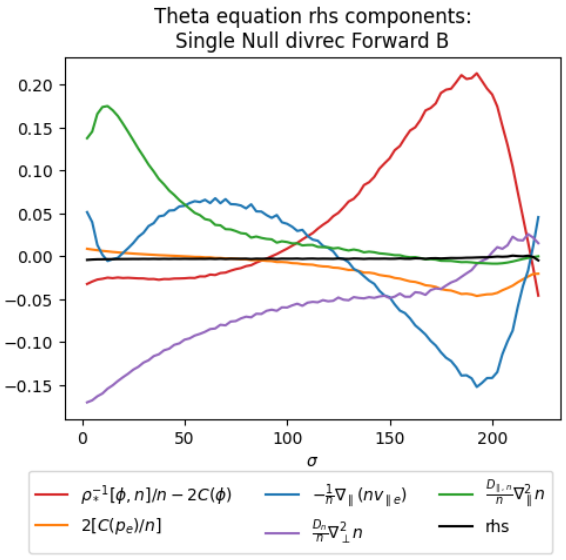

(b) T_e equation

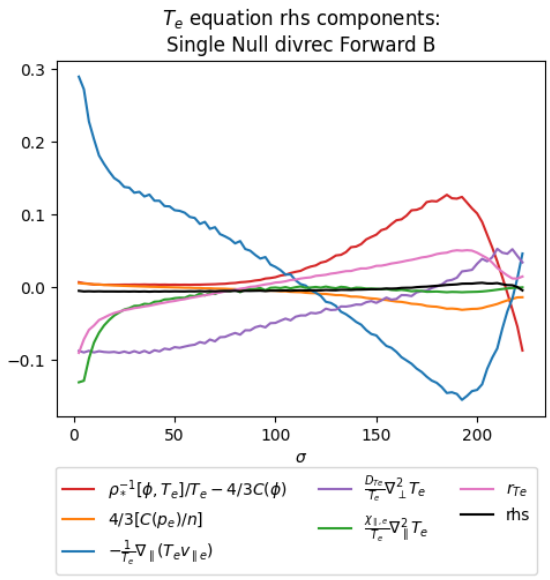

Figure 4.3: n vs T_e equation comparison
The n and T_e equations are compared in logarithmic form (dividing both sides by n and T_e respectively, with $\Theta = \log n$). The term r_{Te} is given by the remaining components of the temperature equation after the common ones are removed, and it is shown not to be negligible

4.2 Refined two-point model

Such an approach is taken in [32], as a refined version of the two-point model is derived starting from the same drift-reduced Braginskii equations (§1.3.2) implemented in GBS, in the particular case of a limited SOL. The predicted results are validated against GBS simulation data. The model estimates the electron temperature drop along a field line from a region far from the limiter to the limiter plates and is obtained by balancing the parallel and perpendicular transport of plasma and heat.

The configuration studied in [32] differs in many aspects from our cases: namely, it considers a limited configuration and takes into account plasma-neutral interaction. Nevertheless, what makes it worth exploring for our particular case is its key idea: the simplification of perpendicular dynamics.

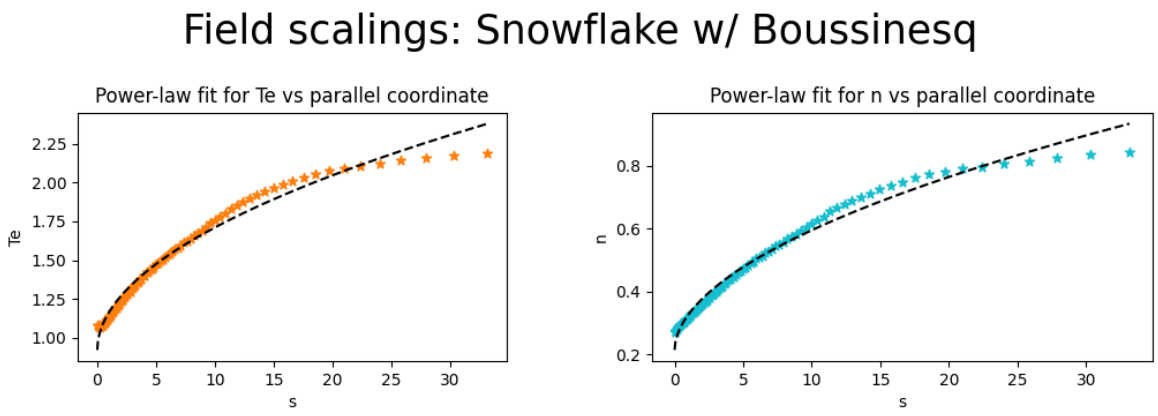

Figure 4.4: Power-law fits for the n and T_e profiles
Power laws of the type $f(s) = bs^a + c$, $f \in \{n, T_e\}$ (black dotted lines) were fitted over the profiles of n and T_e (scattered data points). The resulting exponents in this case were $a_{Te} = 0.512$, $a_n = 0.531$.

All of the contributions which participate in perpendicular transport (e.g. $E \times B$ and diamagnetic transport) are collected into what are defined as *perpendicular source terms*, which are then considered to be independent from the parallel dynamics. Such an approach is powerful since, by making assumptions about the newly defined *source* terms, one does not have to worry about the specifics of each contribution, but just focus on modelling their overall effect.

In the aforementioned paper the authors then proceed to make assumptions about the behaviour of the distribution of the perpendicular source terms independently such that it is possible to integrate the relevant profiles directly. The integration is performed in two steps:

1. rewriting the density and temperature equations in terms of the perpendicular source terms, simplifying all of the negligible terms in order to recover the simplest possible parallel equations;

2. recasting them into a conservation law for density and heat such that one of the profiles can be recovered given the other.

We exploit this same line of reasoning, taking care to adapt the derivation as the assumptions vary, in order to greatly simplify the description of the perpendicular dynamics.

4.2.1 Parallel equations

Following a derivation analogous to [32], one starts from the normalised GBS equations for density (Eq. 2.1) and electron temperature (Eq. 2.5) in the absence of neutrals, which through algebraic manipulation are rewritten as:

$$\begin{cases} \dfrac{\partial n}{\partial t} + \nabla_\parallel (n v_{\parallel,e}) - D_n \nabla_\parallel^2 n = S_{n,\perp} \\ \dfrac{\partial T_e}{\partial t} + \nabla_\parallel (T_e v_{\parallel,e}) - \left[\dfrac{T_e}{3} \nabla_\parallel v_{\parallel,e} \right] - \nabla_\parallel (\chi_{\parallel,e} \nabla_\parallel T_e) = S_{T_e,\perp} \end{cases} \tag{4.2}$$

where the perpendicular source terms are defined as:

$$S_{n,\perp} = -\frac{\rho_*^{-1}}{B}[\phi, n] + \frac{2}{B}\big[C(p_e) - nC(\phi)\big] + D_{n,\perp}\nabla_\perp^2 n + S_n \tag{4.3}$$

$$S_{T_e,\perp} = -\frac{\rho_*^{-1}}{B}[\phi, T_e] + \frac{4T_e}{3B}\left[\frac{7}{2}C(T_e) + \frac{T_e}{n}C(n) - C(\phi)\right] + D_{T_e,\perp}\nabla_\perp^2 T_e + \frac{2}{3}0.71 T_e \frac{\nabla_\parallel j_\parallel}{n} + S_{T_e} \tag{4.4}$$

(the term $\nabla_\parallel j_\parallel$ can be considered as a perpendicular source term as a closure for it involving in curvature operators and Poisson brakets has been found(§3.3)).

Note that the spurious diffusion terms are neglected in [32], whereas they are kept as optional in the post-processing routines.

The key difference with the previous approach is that in one case we collect terms with the same functional form and then expect the remainder terms to be negligible with respect to the common ones, whereas in this case we collect components with the same functional form only for the parallel direction and then observe heuristically the behaviour of the other collected *source* terms, not necessarily expecting them to be negligible.

4.2.2 Scaling relation between n and T_e

The first consequence of the new form of the equations in (4.2) is that it could justify the scaling relation heuristically observed for n and T_e, as one finds that:

- the perpendicular source terms are found to exhibit similar profiles along the leg (Fig. 4.5);
- Eqs.(4.3-4.4) exhibit similar structures, as the term in the square bracket is observed to be small compared to the others.

Thus the following relation will be employed in the subsequent discussion:

$$T_e \simeq \gamma(n + T_0) \sim \gamma n \tag{4.5}$$

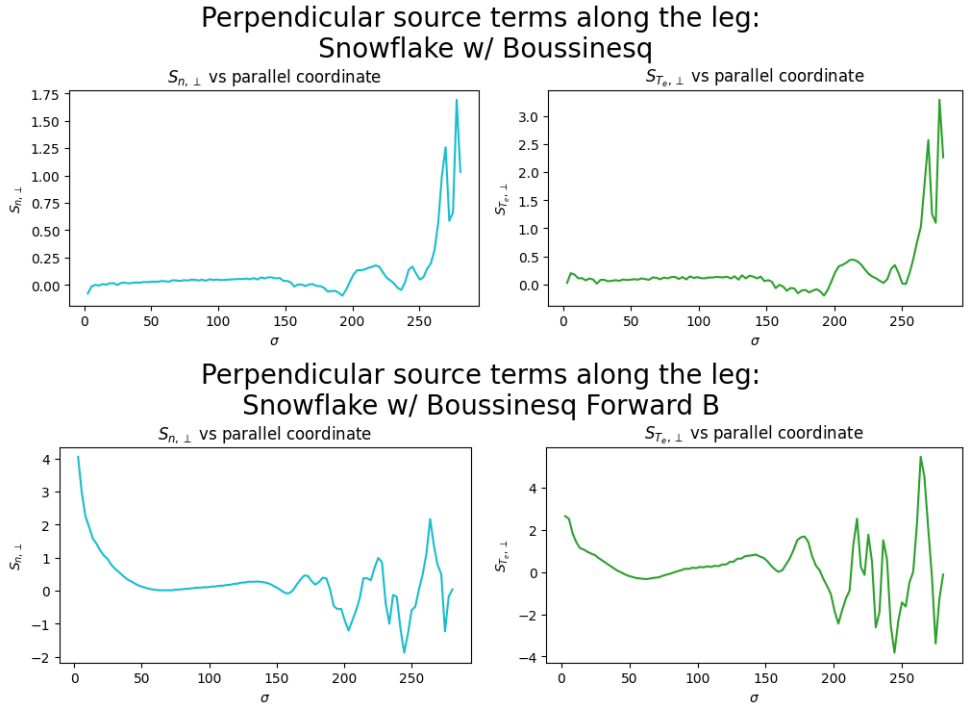

Figure 4.5: Perpendicular source terms
$S_{n,\perp}$ and $S_{Te,\perp}$ were plotted against the poloidal parallel coordinate σ. Similar profiles were observed for the source terms both in reversed and in forward B configurations.

Moreover, this will allow considering only one of the two equations of the system (4.2), as it would be overdetermined otherwise. The density equation is chosen for this purpose.

4.3 Perpendicular source terms

A slightly different approach has been used, compared to [32], when it comes to the perpendicular source terms. That is, instead of making assumptions about their general distributions along the leg as is done in the paper, we decide to approximate the perpendicular dynamics instead.

In particular the approximation of the perpendicular gradients is done by considering the profiles to be of exponential decay type (Fig. 4.6), and therefore rewriting their perpendicular gradients as:

$$f(\zeta) \simeq f_0 e^{-\zeta/\lambda_f}$$
$$\Rightarrow \partial_\perp f \simeq -\frac{f}{\lambda_f}$$

where f could be either n or T_e, ζ is the poloidal perpendicular coordinate (i.e. $\nabla\zeta = +\nabla\psi/|\nabla\psi|$), and λ_f is the characteristic perpendicular decay length of each field, for which an expression in terms of the parallel coordinate will be derived in the next section.

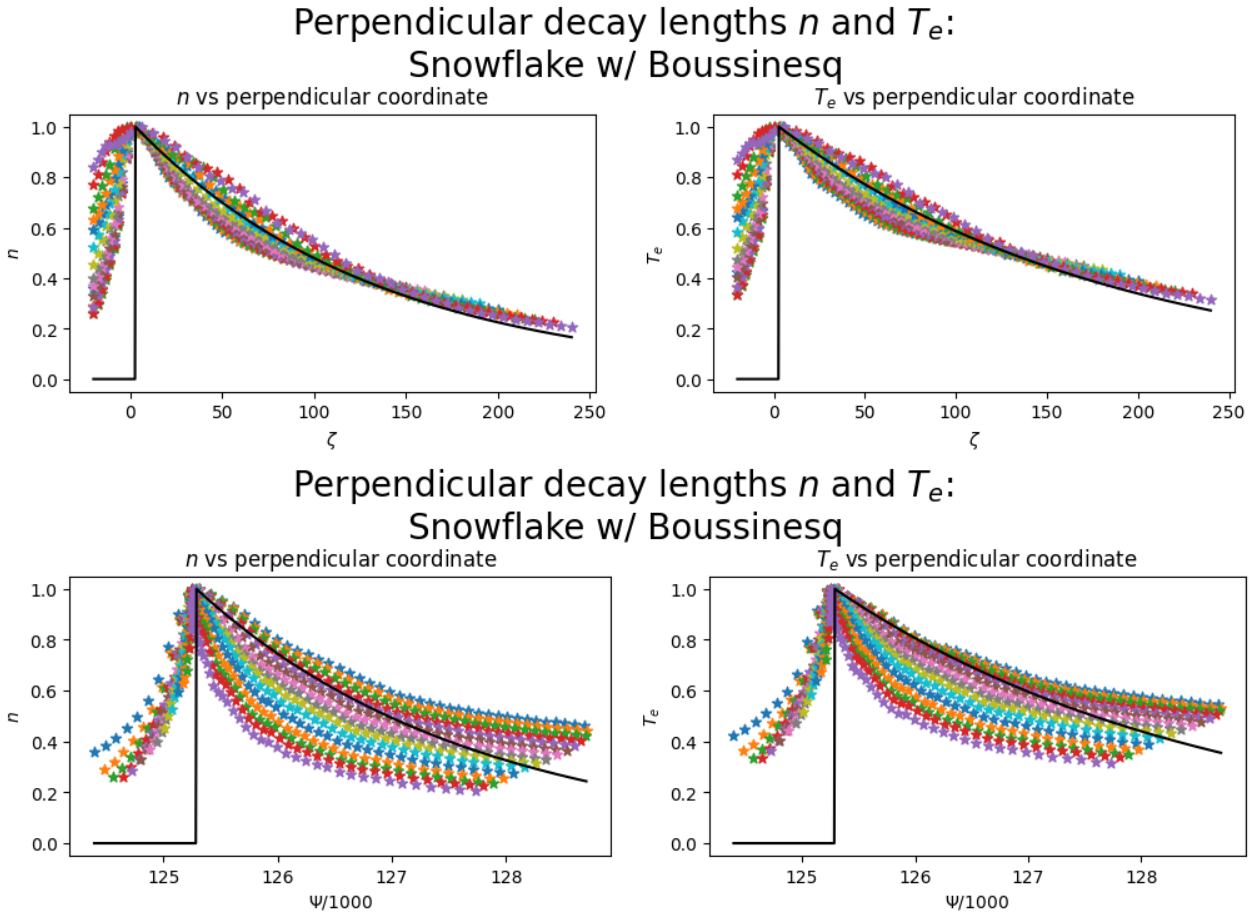

Figure 4.6: n vs T_e perpendicular profiles
The perpendicular profiles have been plotted in terms of the poloidal projection coordinate ζ and of the flux field ψ and normalised with respect to the values on the leg to make comparison easier in terms of exponential decay behaviour. To make the plots more readable the rescaled coordinate $\psi/1000$ was used. The solid black line corresponds to the average exponential decay fit on the different profiles, where 15 lines were selected for each.

A little more complex will be the approximation of the perpendicular gradients for the potential, as its perpendicular dynamics are more complex than in the previous case (Fig. 4.7). The same

approximation is considered:

$$\partial_\perp \phi \simeq -\frac{|\phi|}{\lambda_\phi}$$

this time considering as decay length the scale of variation of the abrupt raise/fall of the profile around the separatrix and allowing for negative values of the parameter to mimic the sign change in the different magnetic configurations.

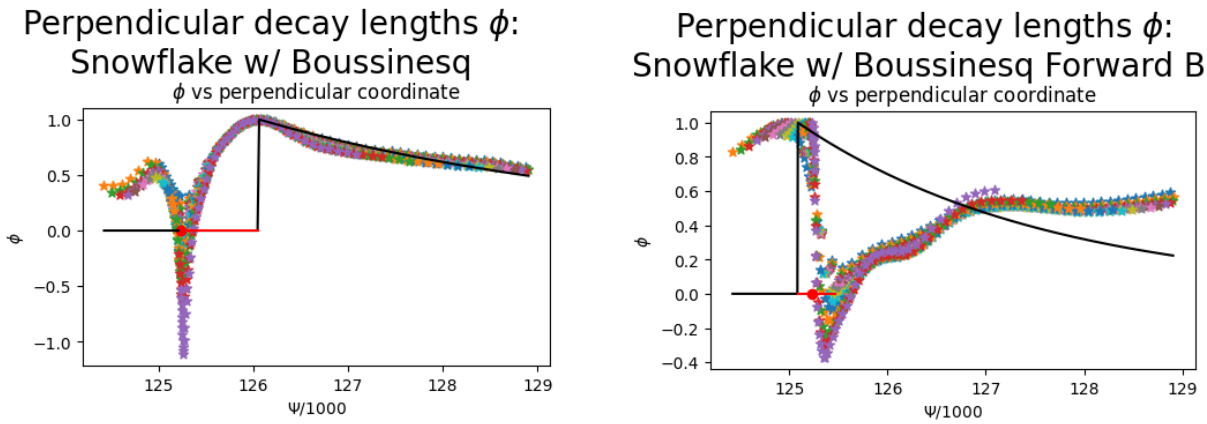

(a) Reversed B **(b)** Forward B

Figure 4.7: ϕ perpendicular profile
ϕ perpendicular profile in the magnetic flux coordinate ψ for reversed and forward B configurations. The red line at the bottom indicates the average length of the $\Delta\psi$ associated to the raise/fall in the profile, while the red dot represents the intersection with the divertor leg. The black line is an exponential decay fit akin to that of the previous case.

One proceeds to rewrite each term in the perpendicular source term as combinations of parallel and perpendicular gradients, which can be simplified as illustrated above.

In all of the following the large aspect ratio approximation and the axisymmetric case will be considered unless explicitly specified otherwise, which justifies the expression of the operator in terms of the previously defined poloidal gradients (§2.3).

Poisson brakets For the Poisson brakets one recovers the following:

$$\begin{aligned}
[\phi, n] &= \mathrm{sign}(B_0)\left(-\tilde{\partial}_\parallel \phi \tilde{\partial}_\perp n + \tilde{\partial}_\parallel n \tilde{\partial}_\perp \phi\right) = \\
&\simeq \frac{\mathrm{sign}(B_0)}{|B_{pol}|}\left(+\tilde{\partial}_\parallel \phi \frac{n}{\lambda_n} - \tilde{\partial}_\parallel n \frac{|\phi|}{\lambda_\phi}\right) = \\
&\simeq \frac{\mathrm{sign}(B_0)}{|B_{pol}|^2}\left(+\partial_\parallel \phi \frac{n}{\lambda_n} - \partial_\parallel n \frac{|\phi|}{\lambda_\phi}\right)
\end{aligned} \tag{4.6}$$

where the corresponding definitions of the perpendicular decay lengths for n and ϕ have been used.

Curvature terms For the curvature terms one obtains:

$$\begin{aligned}\frac{2}{B}[C(p_e) - nC(\phi)] &= \frac{2\,\mathrm{sign}(B_0)}{B}\partial_y p_e - \frac{2\,\mathrm{sign}(B_0)n}{B}\partial_y\phi = \\ &\overset{\dagger}{=} 2\,\mathrm{sign}(B_0)\frac{\partial_y\psi}{|B_{pol}|^2}(\partial_\perp pe - n\partial_\perp\phi) - 2\,\mathrm{sign}(B_0)\frac{\partial_x\psi}{|B_{pol}|^2}(\partial_\parallel pe - \partial_\parallel\phi) = \\ &\simeq \frac{2\,\mathrm{sign}(B_0)\partial_y\psi}{|B_{pol}|^2}\left[-\frac{p_e}{\lambda_{pe}} + n\frac{|\phi|}{\lambda_\phi}\right] - \frac{2\,\mathrm{sign}(B_0)\partial_x\psi}{|B_{pol}|^2}\left[\partial_\parallel pe - n\partial_\parallel\phi\right] = \\ &\simeq \frac{2\,\mathrm{sign}(B_0)\partial_y\psi}{|B_{pol}|^2}\left[-\frac{\gamma n^2}{\lambda_{pe}} + n\frac{|\phi|}{\lambda_\phi}\right] - \frac{2\,\mathrm{sign}(B_0)\partial_x\psi}{|B_{pol}|^2}\left[2\gamma n\partial_\parallel n - n\partial_\parallel\phi\right] \end{aligned} \tag{4.7}$$

using in $\overset{\dagger}{=}$ the fact that the vertical derivative can be rewritten in terms of parallel and perpendicular gradients as:

$$\partial_y f = \frac{\partial_y\psi}{|B_{pol}|^2}\partial_\perp f - \frac{\partial_x\psi}{|B_{pol}|^2}\partial_\parallel f \tag{4.8}$$

In addition, the perpendicular decay length for the pressure can be computed from those of temperature and density, as:

$$p_e = nT_e \Rightarrow \frac{1}{\lambda_{p_e}} = \frac{1}{\lambda_n} + \frac{1}{\lambda_{Te}} \tag{4.9}$$

4.3.1 Perpendicular decay length estimation

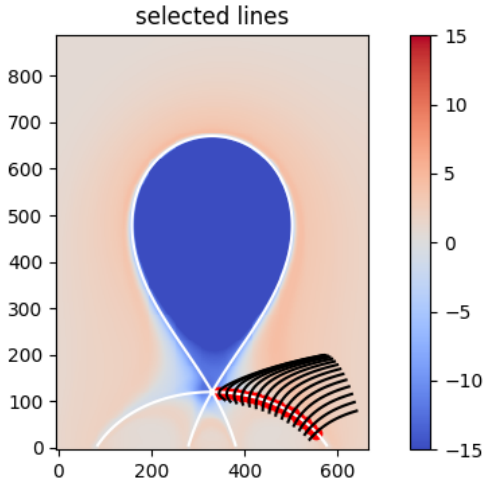

Figure 4.8: $\nabla\psi$ lines selected for the perpendicular profile estimation for the Snowflake case.

In order to recover the dependency of the perpendicular decay length from the parallel coordinate s (in connection length, R_0 units), a numerical approach has been taken, divided in multiple steps. We are interested in obtaining the λ_f's in perpendicular length $\zeta[\rho_0]$ units (namely $\lambda_{f,\zeta}(s)$), and in order to do so one can proceed in the following way:

1. estimate the λ_f's numerically in the magnetic potential coordinate ψ units (namely $\lambda_{f,\psi}(s)$), and observe their dependency on the parallel coordinate s;

2. use the chain rule to obtain the scaling from ψ to ρ_0 units, i.e.:

$$\frac{f}{\lambda_\psi} = \partial_\psi f = \partial_\psi \zeta \partial_\zeta f = \partial_\psi \zeta \frac{f}{\lambda_\zeta}$$
$$\Rightarrow \lambda_{f,\zeta}(s) = \lambda_{f,\psi}(s) \left(\frac{\partial \psi}{\partial \zeta}(0) \right)^{-1}$$

where the perpendicular coordinate has been fixed to $\zeta = 0$ at the intersection with the leg and ψ_0 corresponds to the value of the magnetic potential along the leg. In particular, by definition:

$$\frac{\partial \psi}{\partial \zeta}(0; s) = |\nabla \psi|(s)$$

3. approximate the perpendicular length scale along the leg using the analytic expressions of the recovered relations.

Now the estimation for λ_n, λ_{Te} and λ_ϕ have to be considered separately, as the perpendicular dynamics to be captured are fundamentally different.

n and T_e decay lengths

In order to recover the characteristic perpendicular decay lengths for n and T_e one fits an exponential decay function on the perpendicular profiles of the respective quantities evaluated at lines crossing points distributed along the divertor leg (Fig. 4.8).

An inverse dependency seems to be recovered for the λ_ψ with respect to the parallel coordinate:

$$\lambda_{n,\psi}(s) = \frac{a_n s + b_n}{s + c_n} \simeq \frac{d_n}{s} + a_n \tag{4.10}$$
$$\lambda_{Te,\psi}(s) = \frac{a_{Te} s + b_{Te}}{s + c_{Te}} \simeq \frac{d_{Te}}{s} + a_{Te} \tag{4.11}$$

as can be seen in Fig. 4.9.

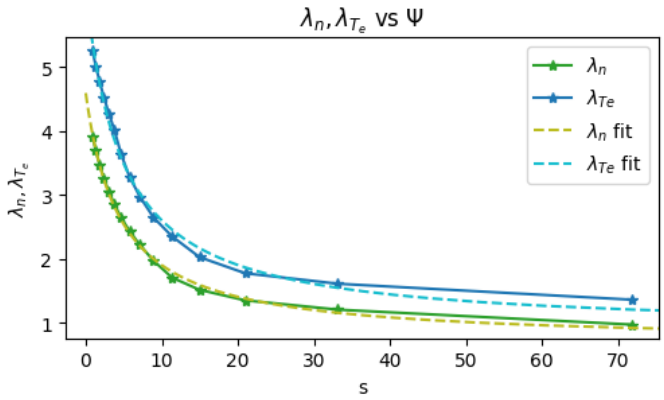

Figure 4.9: Perpendicular decay lengths: n and T_e
An inverse dependency has been fitted on the λ_f, $f \in \{n, T_e\}$ recovered for the profiles shown in Fig. 4.6. The λ_fs labels are in units of ψ and thus were rescaled by the same factor 1/1000.

In particular, for $s \to \infty$ one finds:

$$\frac{1}{\lambda_f} \underset{s \to \infty}{\sim} a_f = \text{const}, \quad f \in \{n, T_e\}$$

In particular for the pressure one can use the estimate:

$$\frac{1}{\lambda_{pe}} = \frac{1}{\lambda_{Te}} + \frac{1}{\lambda_n} \simeq \frac{\frac{d_n}{s} + \frac{d_{Te}}{s}}{\frac{d_n}{s}\frac{d_{Te}}{s}} \simeq \frac{s}{d_{pe}}$$

ϕ decay length

The definition of the perpendicular decay length for the electric potential will require a little more work.

As previously stated, the perpendicular dynamics of the potential is not simply an exponential decay, presenting a complex structure around the leg. What can be observed though is that in many cases one finds an abrupt raise/fall across the leg (taking the perpendicular coordinate) as seen in Fig. 4.7.

Nevertheless, we observe that the profile will relax for $\zeta \to \infty$, therefore the sharp gradient could reasonably be approximated using the ratio between the height of the jump (which is taken as proportional to the value of the field at the leg) and its width.

Thus the characteristic decay length of the potential is defined to be the one associated to such jump and it is allowed to change sign depending on the direction of the fall.

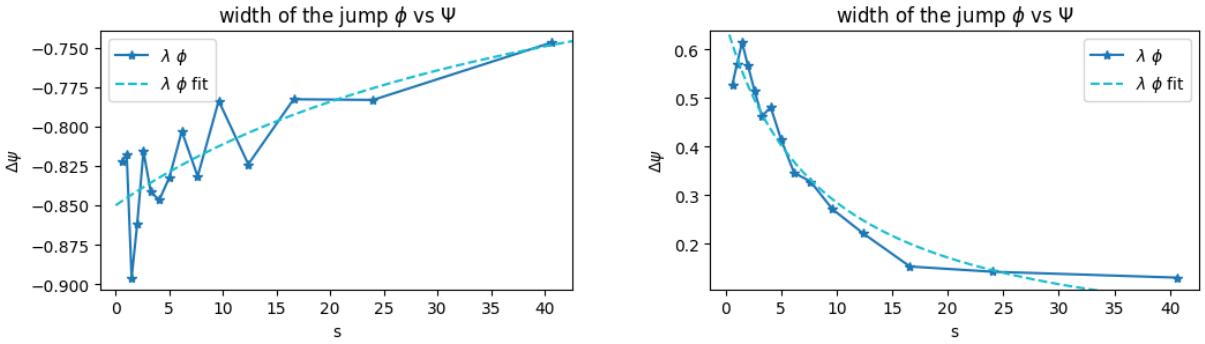

(a) Reversed B **(b)** Forward B

Figure 4.10: Perpendicular decay length: ϕ
Plot of $\lambda_\phi := \Delta\psi$ vs parallel coordinate, recovered for the profiles shown in Fig. 4.7. Analogously to the previous case, an inverse dependency is fitted over the profiles, labelled as "λ_ϕ fit".

In particular it is assumed, analogously to the previous case, $1/\lambda_\phi \underset{s\to\infty}{\sim}$ const.

4.3.2 Parallel density equation

By rewriting the source terms in terms of perpendicular decay lengths and substituting them into the 1^{st} equation of system (4.2) one obtains the following equation:

$$
\begin{aligned}
&v_{\parallel,e}\partial_\parallel n + n\partial_\parallel v_{\parallel,e} - D_n\partial_\parallel^2 n = \\
&= -\operatorname{sign}(B_0)\left[n\left(-\frac{\rho_*^{-1}}{|B_{pol}|^2}\partial_\parallel\phi\frac{1}{\lambda_n} - \frac{2\partial_y\psi}{|B_{pol}|^2}\frac{|\phi|}{\lambda_\phi} - \frac{2\partial_x\psi}{|B_{pol}|^2}\partial_\parallel\phi\right) - \partial_\parallel n\frac{\rho_*^{-1}}{|B_{pol}|^2}\frac{|\phi|}{\lambda_\phi} + \frac{2\partial_y\psi}{|B_{pol}|^2}\frac{\gamma n^2}{\lambda_{p_e}} + \frac{2\partial_x\psi}{|B_{pol}|^2}2\gamma n\partial_\parallel n\right] \\
&= -\frac{\operatorname{sign}(B_0)}{|B_{pol}|}\left[n\left(-\frac{\rho_*^{-1}}{|B_{pol}|}\partial_\parallel\phi\frac{1}{\lambda_n} - 2\cos\theta\frac{|\phi|}{\lambda_\phi} - 2\sin\theta\partial_\parallel\phi\right) + \partial_\parallel n\frac{\rho_*^{-1}}{|B_{pol}|}\frac{|\phi|}{\lambda_\phi} + 2\cos\theta\frac{\gamma n^2}{\lambda_{p_e}} + 4\sin\theta\gamma n\partial_\parallel n\right]
\end{aligned}
$$

where a $1/|B_{pol}|$ factor is collected in the r.h.s. and the components of the poloidal magnetic field are written in terms of the poloidal pitch angle θ:

$$\partial_x\psi = |\nabla\psi|\sin\theta \qquad , \qquad \partial_y\psi = |\nabla\psi|\cos\theta$$

where θ is defined as the angle in the poloidal plane between the vertical axis and $\nabla\psi$.

This last expression, through algebraic manipulation, can be written in the following form:

$$\alpha(s)\partial_\parallel n + \beta(s)n + \delta(s)n^2 + \eta(s)n\partial_\parallel n - D_n\partial_\parallel^2 n = 0 \tag{4.12}$$

with all coefficient functions defined by the corresponding terms in the above equation for simplicity of notation.

A differential equation has been recovered for the density, which in turn is found to be the only remaining unknown of the r.h.s. of Ohm's law: it is now time to gather all of our results into one system which will describe our two observables of interest (density and electric potential) along the divertor leg.

Chapter 5

The density-potential system

5.1 Ohm's law and final system

Substituting all of the obtained relations and the closures into the original formulation of Ohm's law (and considering for simplicity the case in which the Boussinesq approximation is absent) one obtains:

$$
\begin{aligned}
-\nabla_\parallel \phi = \nu j_\parallel - \frac{1}{n}\nabla_\parallel p_e - 0.71\nabla_\parallel T_e - \frac{2}{3n}\nabla_\parallel G_e = \\
\simeq \nu_0 T_e^{-3/2}\left[\int_{leg}\left[2C(p_e+\tau p_i) - \frac{\rho_*^{-1}}{B}\nabla\cdot[\phi,\omega]\right]ds + j_t\right] - \frac{1}{n}\nabla_\parallel p_e - 0.71\nabla_\parallel T_e - \frac{2}{3n}\nabla_\parallel G_e = \\
\overset{\dagger}{\simeq} \nu_0\gamma^{-3/2}n^{-3/2}\left[\int_{leg}\left[2C(p_e+\tau p_i) - \frac{\rho_*^{-1}}{B}\nabla\cdot[\phi,\omega]\right]ds + j_t\right] - \frac{\gamma\nabla_\parallel(n^2)}{n} - 0.71\gamma\nabla_\parallel n = \\
= \nu_0\gamma^{-3/2}n^{-3/2}\left[\int_{leg}\left[2C(p_e+\tau p_i) - \frac{\rho_*^{-1}}{B}\nabla\cdot[\phi,\omega]\right]ds + j_t\right] - 2.71\gamma\nabla_\parallel n = \\
= \nu_0\gamma^{-3/2}n^{-3/2}\left[\int_{leg}\left[2C(p_e+\tau p_i)\right] + j_t\right] + \Xi(s) - 2.71\gamma\nabla_\parallel n
\end{aligned}
\tag{5.1}
$$

where j_t is the value of the current at the target and in the step (†) the definition of ν, the scaling relation between n and T_e (Eq. 4.5) and the fact that the gyroviscuous term is negligible in the integral formulation (§3.2) have been considered, in the spirit of verifying Ohm's law at an integral level. Moreover in the last step the following term was defined:

$$
\Xi(s) := \begin{cases} -\nu_0\gamma^{-3/2}n^{-3/2}\displaystyle\int_0^s\left[\rho_*^{-1}\nabla\cdot[\phi,\omega]\right]ds & \text{(non-Boussinesq case)} \\ -\nu_0\gamma^{-3/2}n^{-3/2}\displaystyle\int_0^s\left[\rho_*^{-1}n\nabla[\phi,\omega]\right]ds & \text{(Boussinesq case)} \end{cases}
\tag{5.2}
$$

as not to treat it analytically, but to consider it separately.

Then, substituting the corresponding expressions for the curvature operators in (5.1) one gets:

$$
\begin{aligned}
-\nabla_{\parallel}\phi &= \nu_0\gamma^{-3/2}n^{-3/2}\int_{leg}\Big[2C(p_e+\tau p_i)\Big]ds+\nu_0\gamma^{-3/2}n^{-3/2}j_t+\Xi(s)-2.71\gamma\nabla_{\parallel}n= \\
&\simeq \nu_0\gamma^{-3/2}n^{-3/2}\int_{leg}\Big[2\,\mathrm{sign}(B_0)\Big(\frac{\partial_y\psi}{|B_{pol}|^2}\partial_{\perp}-\frac{\partial_x\psi}{|B_{pol}|^2}\partial_{\parallel}\Big)(pe+\tau pi)\Big]ds+\nu_0\gamma^{-3/2}n^{-3/2}j_t \\
&\quad +\Xi(s)-2.71\gamma\nabla_{\parallel}n= \\
&\simeq \nu_0\gamma^{-3/2}n^{-3/2}\int_{leg}\Big[2\,\mathrm{sign}(B_0)\Big(\frac{\partial_y\psi}{|B_{pol}|^2}\frac{(pe+\tau pi)}{\lambda_p}-\frac{\partial_x\psi}{|B_{pol}|^2}\nabla_{\parallel}(pe+\tau pi)\Big)\Big]ds+\nu_0\gamma^{-3/2}n^{-3/2}j_t+ \\
&\quad +\Xi(s)-2.71\gamma\nabla_{\parallel}n= \\
&\simeq \nu_0\gamma^{-3/2}n^{-3/2}\int_{leg}\Big[2\,\mathrm{sign}(B_0)\Big(\frac{\partial_y\psi}{|B_{pol}|^2}\frac{(\gamma n^2+\tau nT_i)}{\lambda_p}-\frac{\partial_x\psi}{|B_{pol}|^2}2\gamma n\nabla_{\parallel}n-\frac{\partial_x\psi}{|B_{pol}|^2}\nabla_{\parallel}(\tau pi)\Big)\Big]ds+ \\
&\quad +\nu_0\gamma^{-3/2}n^{-3/2}j_t+\Xi(s)-2.71\gamma\nabla_{\parallel}n= \\
&\simeq \nu_0\gamma^{-3/2}n^{-3/2}\int_{leg}\Big[2\,\mathrm{sign}(B_0)\Big(\frac{\partial_y\psi}{|B_{pol}|^2}\frac{\gamma(1+\tau\mu)n^2}{\lambda_p}-\frac{\partial_x\psi}{|B_{pol}|^2}2\gamma(1+\tau\mu)n\nabla_{\parallel}n\Big)\Big]ds+ \\
&\quad +\nu_0\gamma^{-3/2}n^{-3/2}j_t+\Xi(s)-2.71\gamma\nabla_{\parallel}n= \\
&= 2\nu_0(1+\tau\mu)\gamma^{-1/2}n^{-3/2}\int_{leg}\Big[\frac{\mathrm{sign}(B_0)}{|B_{pol}|}\Big(\frac{n^2\cos\theta}{\lambda_p}-2\sin\theta n\nabla_{\parallel}n\Big)\Big]ds+\nu_0\gamma^{-3/2}n^{-3/2}j_t+ \\
&\quad +\Xi(s)-2.71\gamma\nabla_{\parallel}n
\end{aligned}
\tag{5.3}
$$

using in the last step a scaling relation between the electron and ion temperature, with $T_i \simeq \mu T_e$.

Thus a system of equations for the density and the potential is obtained:

$$
\begin{cases}
\partial_s\phi = 2\nu_0(1+\tau\mu)\gamma^{-1/2}n^{-3/2}\displaystyle\int_{leg}\Big[\frac{\mathrm{sign}(B_0)}{|B_{pol}|}\Big(-\frac{n^2\cos\theta}{\lambda_p}+2\sin\theta n\partial_s n\Big)\Big]ds+\nu_0\gamma^{-3/2}n^{-3/2}j_t \\
\qquad +\Xi(s)+2.71\gamma\partial_s n \\
\\
-\alpha(s)\partial_s n+\beta(s)n+\delta(s)n^2-\eta(s)n\partial_s n-D_{\parallel,n}\partial_s^2 n=0
\end{cases}
\tag{5.4}
$$

which describes the full profiles of these observables along the divertor leg, given the initial conditions. What makes this result powerful is that the only information needed is that of the value of the observables at the target (where they could, in principle, be measured experimentally or imposed as boundary conditions [29]).

One can proceed to analyse the type of information this equation encompasses, in particular in regards of the potential structure we are interested in.

5.2 Simplified density profile

The first type of analysis would be to consider a simplification of the density profile in order to verify whether the model matches the predicted behaviour at least qualitatively, similarly to the one in [20]. The form of our system allows us to do so, as the potential equation only involves the density profile, and therefore could be extrapolated independently if one were to make hypothesis on the latter.

5.2.1 Linear density profile

For a start, the simplest possible case is taken, that is a linear density profile:

$$
n(s) = as + n_t \tag{5.5}
$$

and one replaces its expression in the equation for the potential in (5.4); moreover, a simplified geometry is considered, with a straight divertor leg (constant θ). Recall that $T_e \simeq \gamma(n + T_0)$, so that the electron temperature can be written itself as a linear profile:

$$T_e(s) = \gamma\left(n(s) + T_0\right) = \gamma\left(as + T_0 + n_t\right)$$

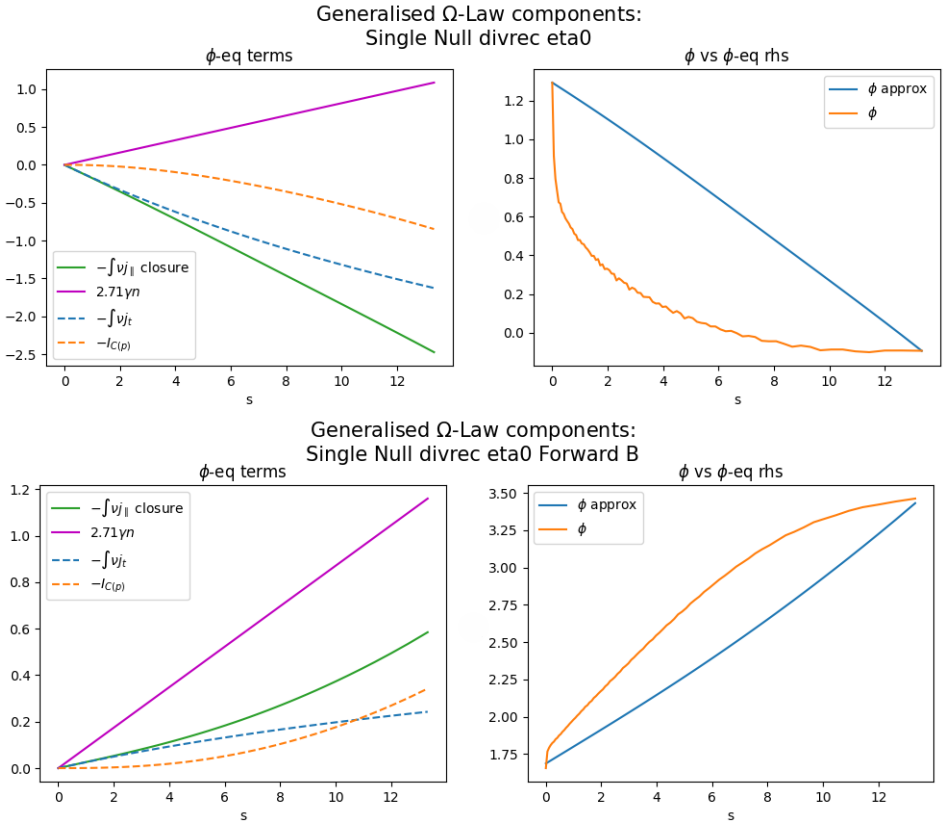

Figure 5.1: Integrated ϕ equation for linear n profile
The terms corresponding to the thermoelectric current and the one for the parallel current are labelled $2.71\gamma n$ and "$\int \nu j_\parallel$ closure" respectively, as in rest of the discussion; the second in particular is decomposed into the Pfirsch-Schlüter contribution ($I_{C(p)}$, as in Eq. 5.6) and the target current one ($\int \nu j_{\parallel,t}$). The term labelled "ϕ approx." is merely their sum and is compared to the real ϕ profile along the leg. $\theta = \pi/3$ was assumed along the leg.

Numerically integrating the equation (as it is sufficient to integrate the r.h.s., given the density profile), it seems to match the expected qualitative behaviour. One observes, in fact, both the predicted dominating terms in the forward/reversed B configurations (the thermoelectric and parallel currents, respectively) and the sign reversal of the potential (Fig. 5.1). The match is quantitatively better when the pitch angle profile is taken into account, by extrapolating it from the data (Fig. 5.2).

Analytically one can substitute the expression (5.5) into the first equation in (5.4), integrating and obtaining:

$$\begin{aligned}
&\phi(s) - \phi_t = \\
&= -2\nu_0(1+\tau\mu)\gamma^{-1/2}\int_0^s (as' + n_t + T_0)^{-3/2}\int_0^{s'}\left[\frac{\mathrm{sign}(B_0)}{|B_{pol}|}\left(\frac{(as''+n_t)^2\cos\theta}{\lambda_p(s'')} - 2\sin\theta a(as''+n_t)\right)\right]ds''ds' \\
&\quad + \int_0^s \nu_0\gamma^{-3/2}(as' + n_t + T_0)^{-3/2} j_t ds' + 2.71\gamma as = \\
&= I_{C(p)}(s) + \nu_0\gamma^{-3/2} j_t \frac{2}{a}\left(\frac{1}{\sqrt{n_t + T_0}} - \frac{1}{\sqrt{as + n_t + T_0}}\right) + 2.71\gamma as
\end{aligned} \tag{5.6}$$

where $I_{C(p)}$ is defined as the first double integral, due to the closure of the parallel current gradient, and the offset T_0 has been considered for the temperature-density scaling relation (4.5). In the following discussion the term associated to the parallel current contribution will be denoted as:

$$\int \nu j_{\parallel} ds := I_{C(p)} + \int \nu j_t ds$$

where $\nu = \nu_0 T_e^{-3/2}$ is the Spitzer resistivity and j_t is the parallel current at the target.

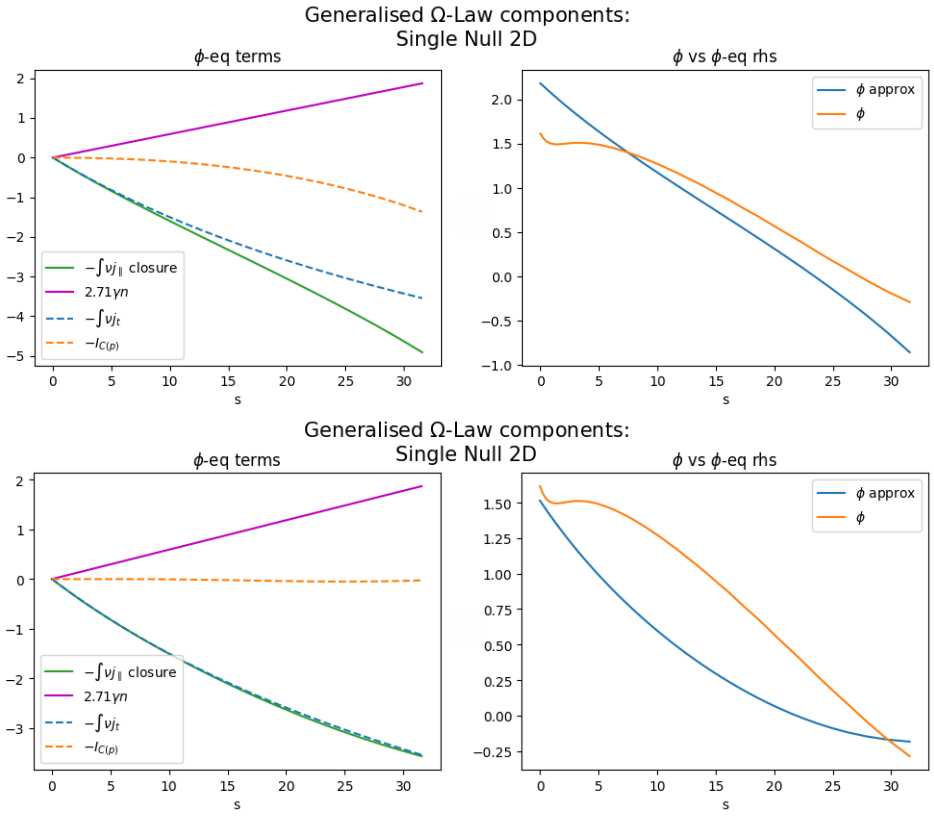

Figure 5.2: Integrated ϕ equation for linear n profile
The pitch angle θ profile has been extrapolated from the data in the bottom case, and is compared to the top case in which a constant $\theta = \pi/4$ was considered.

An analysis can be performed considering each contribution to our model. The first two terms are those associated to the parallel current term, of which the first one, $I_{C(p)}$, corresponds to the Pfirsch-Schlüter current in [20], as it corresponds to the closure of the parallel current gradient. It contains an implicit dependency on the sign of the toroidal magnetic field, which makes it be favourable to the magnetic structure (i.e., gives an overall negative contribution for the potential well cases, and a positive one for that of the potential hill ones). The second one is due to the initial value of the current at the target, and is usually significantly larger in magnitude in the reversed case (when it is always negative) rather than in the forward, to the point where it is the one setting the potential structure in the reversed cases. The last contribution, associated with the thermoelectric currents, has constant sign, and is the one setting the potential in the forward cases.

In order to obtain a scaling law, one can consider the following approximations:

- a straight divertor leg ($\theta = const$)

- a simple inverse dependency for the perpendicular decay length of $\lambda_{pe,\psi} \sim \frac{d_{pe}}{s}$ (§4.3.1)

- an exponential dependency of the parallel coordinate on the poloidal length, that is: $s(\sigma) \simeq c_1 e^{c_2 \sigma}$, with σ the length of the poloidal projection of the leg, so to mimic the divergence of the connection length at the X-point. Given the definition of s (§2.3), this gives a dependency of the type $1/|B_{pol}| \propto s$, so that the second term in the integral can be rewritten as:

$$2\frac{\text{sign}(B_0)}{|B_{pol}|}\sin\theta a(as+n_t) \simeq 2\frac{\text{sign}(B_0)}{B_t}\sin\theta a(as+n_t)s, \quad B_t = \text{const}$$

This way the following scaling law for the potential is obtained:

$$\begin{aligned}\phi(s)-\phi_t &\simeq \frac{2\nu_0(1+\tau\mu)\gamma^{-1/2}}{\sqrt{as+n_t+T_0}}\left(c_4 s^4+c_3 s^3+c_2 s^2+c_1 s+c_{1/2}\sqrt{as+n_t+T_0}+c_0\right)+\\ &\quad+\nu_0\gamma^{-3/2}j_t\frac{2}{a}\left(\frac{1}{\sqrt{n_t+T_0}}-\frac{1}{\sqrt{as+n_t+T_0}}\right)+2.71\gamma as\\ &\simeq -\text{sign}(B_0)\frac{2\nu_0(1+\tau\mu)\gamma^{-1/2}}{\sqrt{as+n_t+T_0}}\frac{a\cos\theta}{14 d_{pe}}s^4+\nu_0\gamma^{-3/2}j_t\frac{2}{a}\frac{1}{\sqrt{n_t+T_0}}+2.71\gamma as \end{aligned} \tag{5.7}$$

retaining only the highest power in the expression for the parallel current closure and the asymptotically constant term for the initial condition. The constants coefficients $c_4, c_3, c_2, c_1, c_{1/2}, c_0$ corresponding to the different powers of s appearing in the analytic expression for the integral can be shown to be of similar magnitudes, as they are derived from the expansion of a polynomial with coefficients of similar magnitude (a, n_t and $n_t + T_0$ are of the same order of magnitude), multiplied by common terms which are one order of magnitude apart ($\cos\theta/d_{pe} \sim \frac{1}{10} 2\sin\theta/B_t$); hence one can keep only the highest order in the parallel coordinate, as the parallel coordinate reaches values in the $10-15$ range for Single Nulls, $30-40$ for Snowflakes (refer to Appendix A for the definition of the other constants).

From the scaling relation one could extrapolate an explanation as to why the phenomenon seems to be more prominent in Snowflake configurations rather than in Single Nulls: the parallel coordinate is much larger in the Snowflake cases due to the much greater flux expansion, thus making the potential drop along the divertor leg much larger in unfavourable configurations. Moreover one can observe the effects of the two regulating parameters of the model, that is the resistivity ν_0 and the density condition at the target n_t. The former widens the magnitude of the $\Delta\phi$, although less in the forward B configurations as it is associated to the parallel current contribution $\int \nu j_\parallel ds$ which is not dominant; moreover, the curving of the potential associated to the Pfirsch-Schlüter current becomes more noticeable correspondingly, as it is proportional to ν_0 itself. The target condition n_t instead decreases the gap as it increases, more noticeably so in the reversed B case as it is associated with the dominant term.

The above result can be compared with the scaling law obtained in [20] (Eq. 3.1); in order to do so one has to reconsider the approximations taken into account, applied to our case. In particular, starting from the first equation in system (5.4):

- a constant flux expansion is considered, which entails:
  - a constant $1/|B_{pol}| \simeq 1/B_c$ along the leg;
  - constant $\lambda_f, \forall f \in \{n, T_e, p_e\}$, as they capture the dependency on flux expansion along the leg, thus:
$$\frac{1}{|B_{pol}|}\frac{1}{\lambda_{pe}(s)} \simeq \frac{1}{B_c}\frac{1}{\lambda_{pe}} = \text{const}$$
  - that the parallel coordinate s becomes simply a rescaling of the poloidal coordinate σ by a constant factor, as:
$$s = \int_0^\sigma \frac{1}{|B_{pol}|}d\sigma \simeq \int_0^\sigma \frac{1}{B_c}d\sigma = \frac{1}{B_c}\sigma$$

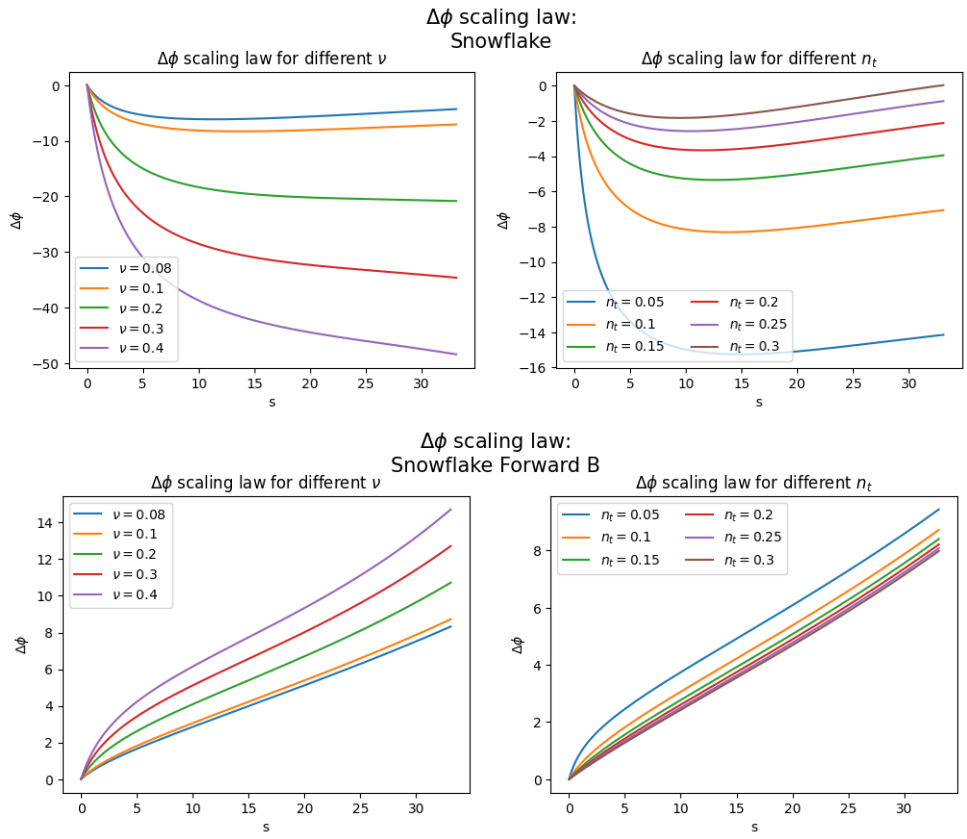

Figure 5.3: $\Delta\phi$ scaling law
Scaling law for the potential along the leg in the case of a simplified power-law density profile of the type: $n(s) = as + n_t$. Potential profiles are plotted for different resistivities (constant $n_t = 0.1$) and different value of density condition at the target (constant $\nu = 0.1$). The full expression for the component associated to the target current was used in order to have a $\Delta\phi = 0$ at the target: $\int \nu j_t = \nu_0 \gamma^{-3/2} j_t \frac{2}{a} \left(\frac{1}{\sqrt{n_t + T_0}} - \frac{1}{\sqrt{as + n_t + T_0}} \right)$.

- it considers linear profiles with negligible conditions at the target to approximate the gradients, so that one has $\nabla_s f \simeq f(s)/s, \forall f \in \{n, T_e, p_e, \phi\}$. In particular for the pressure this entails:

$$\frac{\partial_s p_e(s)}{n(s)} \simeq \frac{p_e(s)}{s} \frac{1}{n(s)} = \frac{n(s) T_e(s)}{s} \frac{1}{n(s)} = \frac{T_e(s)}{s} \simeq \partial_s T_e$$

  Thus, the thermoelectric current term $2.71\gamma\partial_s n \simeq 2.71\partial_s T_e$ turns into $1.71\partial_s T_e$, which integrated gives the required term $1.71 T_e(s)$;

- the resistivity is taken directly at the target and assumed to be constant, so that one can take it outside of the integration:

$$\nu \simeq \frac{\nu_0}{T_e(s)^{3/2}} \simeq \frac{\nu_0}{(T_e^t)^{3/2}}$$

- a null condition is considered at the target for the parallel current: $j_t \simeq 0$;

- the diamagnetic contribution in the argument of the double integral $I_{C(p)}$ is taken to be only perpendicular to the integration path, therefore neglecting the second term in the integration.

Substituting all of these hypothesis and rewriting everything in terms of the corresponding $n(s), T_e(s), T_e^t$

values to make the comparison with (3.1) easier, one recovers:

$$\phi(s) - \phi_t = -\operatorname{sign}(B_0)\frac{2\nu_0(1+\tau\mu)}{\lambda_{pe}B_c}\cos\theta\frac{n(s)T_e(s)}{(T_e^t)^{3/2}}s^2 + 1.71T_e(s)$$
$$\Rightarrow \frac{\phi(s)-\phi_t}{T_e(s)} = -\operatorname{sign}(B_0)2(1+\tau\mu)\frac{\nu_0\cos\theta}{\lambda_{pe}B_c}\frac{n(s)}{(T_e^t)^{3/2}}s^2 + 1.71$$

which, taking $s = s_{XP}$ (corresponding to L_{XP}/B_c) gives the required comparison.

Then one can examine each of the juxtaposed terms. First of all, the thermoelectric current contribution $j^W_{thm} = 1.71T_e(s)$ is smaller than the one one expects in direct comparison from (5.7), $j_{thm} = 2.71\gamma n(s) = 2.71T_e(s)$, by almost a factor 1.5, which could explain the fact that it was not considered dominant in the forward case. This could be due to the fact that a linear profile was assumed for the pressure, whereas it would be quadratic in our case, if one takes the other profiles to be linear. Second of all, the Spitzer resistivity is considered to be constant for the parallel current term $\int \nu j_\parallel ds$, which makes it remain much bigger in magnitude than in our case, as the temperature increases along the leg. This makes it dominant in the approximation but not in our model. Finally, the Pfirsch-Schlüter contribution $I_{C(p)}$ is observed to gain importance as $s \gg 1$ (that is, getting closer to the X-point). The term associated to the current at the target $\int \nu j_t ds$, not present in (3.1) as $j_t = 0$ is assumed, becomes constant, while the Pfirsch-Schlüter one increases proportionally to $1/|B_{pol}|$. Thus, the reason why it is not dominating in our data could be owed to the fact that we consider a large but finite s, for which the initial conditions for the current prevails up until very close to the X-point (Fig. 5.1).

5.2.2 General power-law density profile

One can proceed to consider a more general form for our density profile, that is using a power-law dependency: our density profiles are found to take a square root dependency in the data (Fig. 4.1); moreover, this could be compared to highly-recycling regimes (for which a square dependence is expected on the parallel coordinate).

We use a generalised power-law of the type:

$$n(s) = (as+b)^\omega \tag{5.8}$$

for general coefficients a, b and power ω.

Analytically one obtains, analogously to the previous case:

$$\begin{aligned}
&\phi(s) - \phi_t = \\
&= -2\nu_0(1+\tau\mu)\gamma^{-1/2}\int_0^s (as'+b)^{-3\omega/2}\int_0^{s'}\left[\frac{\operatorname{sign}(B_0)}{|B_{pol}|}\left(\frac{(as''+b)^{2\omega}\cos\theta}{\lambda_p(s'')} - 4a\omega\sin\theta(as''+b)^{2\omega-1}\right)\right]ds''ds' \\
&\quad + \int_0^s \nu_0\gamma^{-3/2}(as'+b)^{-3\omega/2}j_t ds' + 2.71\gamma\left((as+b)^\omega - b^\omega\right) = \\
&= I_{C(p)}(s) + \nu_0\gamma^{-3/2}j_t\frac{2}{a(3\omega-2)}\left(\frac{1}{b^{3\omega/2-1}} - \frac{1}{(as+b)^{3\omega/2-1}}\right) + 2.71\gamma\left((as+b)^\omega - b^\omega\right)
\end{aligned}$$

where the T_0 offset for the temperature-density scaling has been neglected for simplicity.

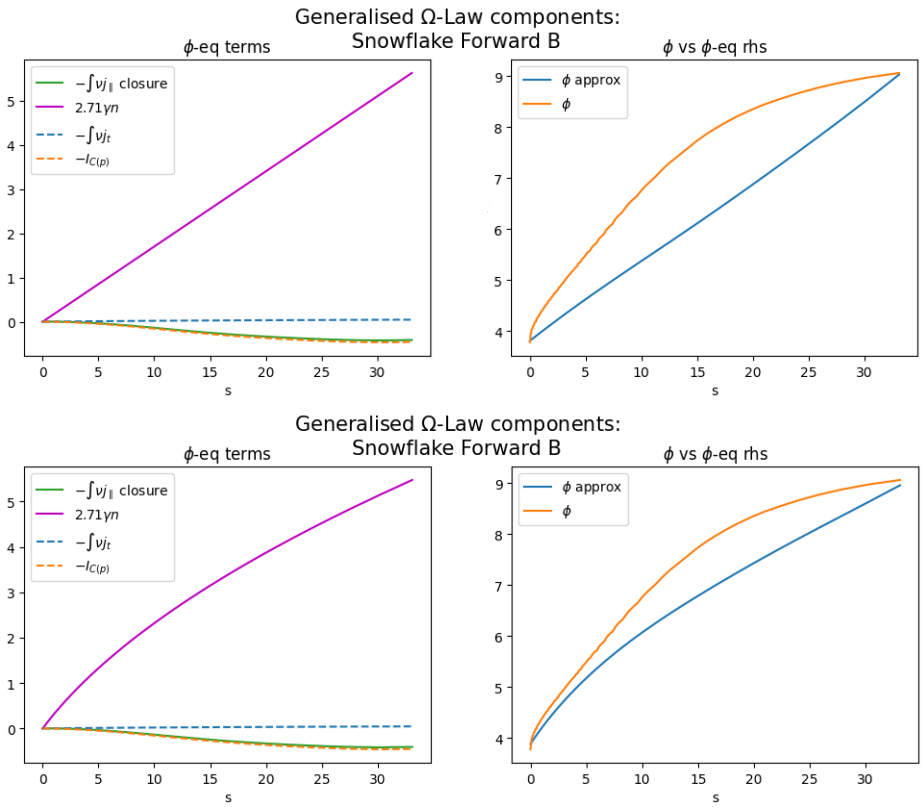

Figure 5.4: Integrated ϕ equation for power-law n profile
The ϕ profile is obtained using the simplified n ansatz for the same simulation. The top one corresponds to the linear density case, and it is compared to the bottom one, in which we consider a power law of the type: $n(s) = (as + b)^\omega, \omega = 1/2$.

This time a scaling law of the type:

$$\begin{aligned}\phi(s) - \phi_t \simeq & \frac{2\nu_0(1+\tau\mu)\gamma^{-1/2}}{(as+n_t)^{3\omega/2}}\left(c_{2\omega+3}(as+b)^{2\omega}s^3 + c_{2\omega+2}(as+b)^{2\omega}s^2 + c_{2\omega+1}(as+b)^{2\omega}s\ ...\right) + \\ & + \nu_0\gamma^{-3/2}j_t\frac{2}{a(3\omega-2)}\left(\frac{1}{b^{3\omega/2-1}} - \frac{1}{(as+b)^{3\omega/2-1}}\right) + 2.71\gamma\left((as+b)^\omega - b^\omega\right) \\ \simeq & -\operatorname{sign}(B_0)2\nu_0(1+\tau\mu)\gamma^{-1/2}\frac{\cos\theta}{d_{pe}}\frac{(as+b)^{\omega/2}s^3}{(1+\omega)(6+\omega)} + \\ & + \nu_0\gamma^{-3/2}j_t\frac{2}{a(3\omega-2)}\left(\frac{1}{b^{3\omega/2-1}} - \frac{1}{(as+b)^{3\omega/2-1}}\right) + 2.71\gamma\left((as+b)^\omega - b^\omega\right) \qquad (5.9)\end{aligned}$$

is recovered in the straight leg approximation and retaining again the highest order term for the integral, in analogy to the previous case. Note that the coefficient of the highest order term in $I_{C(p)}$, $c_{2\omega+3} = -\frac{\operatorname{sign}(B_0)}{(1+\omega)(6+\omega)}\frac{\cos\theta}{d_{pe}}$, coincides with the coefficient $c_4 = -\operatorname{sign}(B_0)\frac{\cos\theta}{14 d_{pe}}$ in the expansion for the case $\omega = 1$.

Note that in this case, compared to the linear density one, the $\Delta\phi$ decreases in absolute value in both magnetic configurations (reversed and forward B), but the contribution due to the Pfirsch-Schlüter closure $I_{C(p)}$ becomes appreciable earlier, as the potential starts curving more evidently.

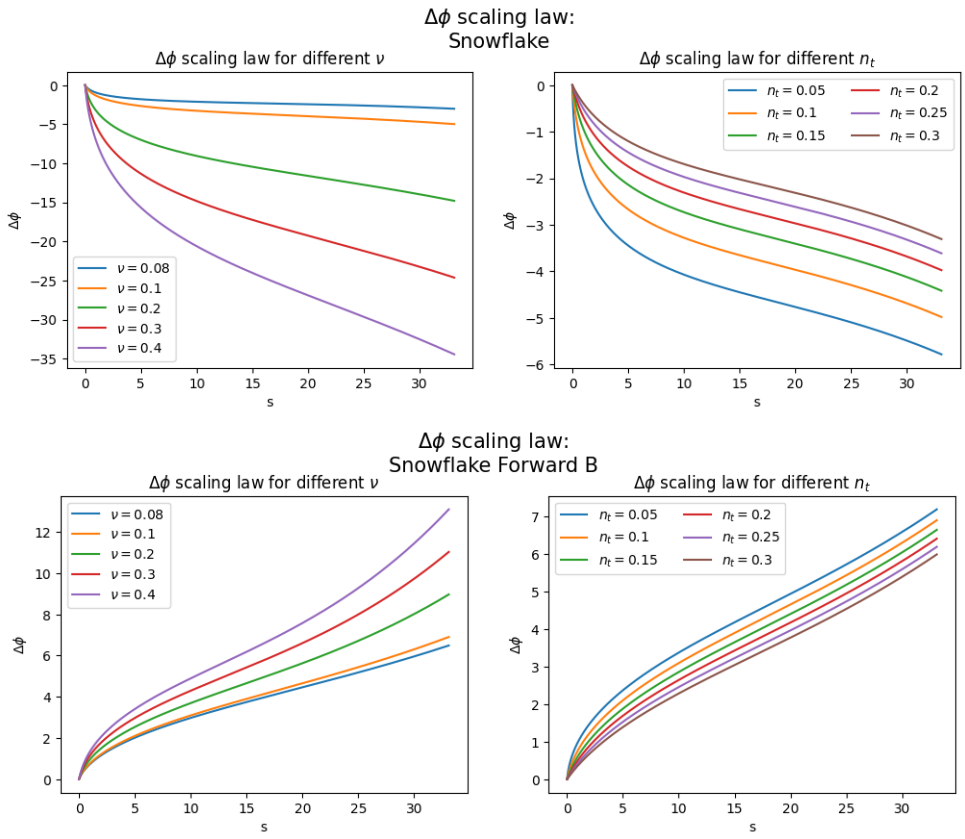

Figure 5.5: $\Delta\phi$ scaling law
Scaling law for the potential along the leg in the case of a simplified power-law density profile of the type: $n(s) = (as + b)^{\omega}, \omega = 1/2$. Potential profiles are plotted for different resistivities (constant $n_t = 0.1$) and different value of density condition at the target (constant $\nu = 0.1$).

5.3 Numerical integration

While the density equation in system (5.4) is not directly analytically integrable, it could however be investigated employing numerical tools.

One starts by defining the integration scheme for the density equation. To do so one rewrites the second equation in (5.4) as a system, defining the auxiliary field $m(s) := \partial_s n$:

$$\begin{cases} \partial_s^2 n = \partial_s m = \frac{1}{D_{\parallel,n}} \left[-\alpha(s)m + \beta(s)n + \delta(s)n^2 - \eta(s)nm \right] \\ \partial_s n = m \end{cases} \tag{5.10}$$

The code allows for both the straight leg approximation ($\theta = const$, given as an additional parameter) and to infer the variation of the pitch angle from the data (analogously to what was done for the simplified profile).

Then one can employ this scheme to gain different types of information about the system.

5.3.1 Simplified density profile: error estimation

An informative result which can be obtained by employing the numerical integration scheme is an estimate of the error for the previously used simplified density profile *ansatz*, as one could substitute the profiles obtained for ϕ and $\partial_s\phi$ into the equation for the density and consider the integration scheme in (5.10) to integrate the corresponding density profile along the leg. The result could be

compared to the real density profile, akin to what is done in the case of the potential, with the error estimate given by the relative mean absolute difference:

$$err = \mathbb{E}\left[\frac{|n_{est} - n_{real}|}{n_{real}}\right]$$

The deviation from our original model is instead evaluated from the relative average modulus of the l.h.s. of (4.12), that is defining a metric of the kind:

$$d(n_{est}, n_{real}) = \mathbb{E}\left[\frac{|-\alpha(s)\partial_s n_{est} + \beta(s) n_{est} + \delta(s) n_{est}^2 - \eta(s) n_{est}\partial_s n_{est} - D_{\|,n}\partial_s^2 n_{est}|}{n_{real}}\right]$$

In principle, one could aim at constructing a fixed point iteration by back-substituting the obtained density profile into the equation for the potential and proceeding iteratively until one obtains a distance from the profile within a certain threshold. The results can be seen in Figs. **??**.

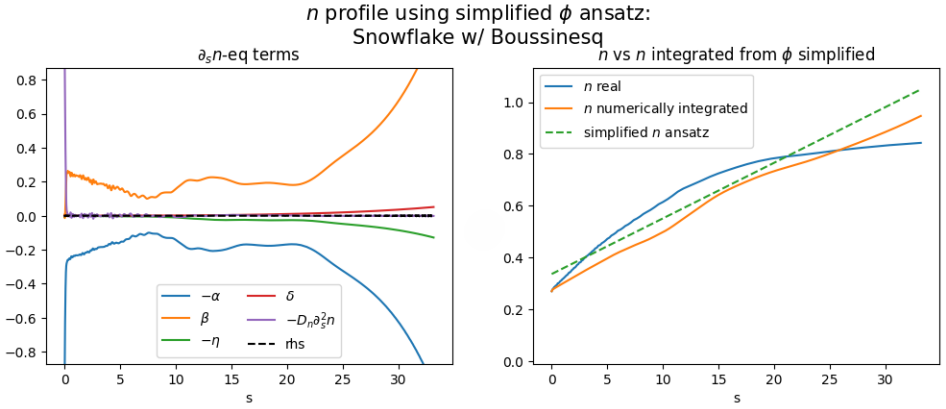

Figure 5.6: Simplified n profile: error estimation
As before, the pitch angle θ profile has been given as a datum. The ϕ profiles obtained for the linear density case were substituted into the corresponding terms for the density equation, integrating for n. The resulting approximation has been compared against the real profile. The term labelled as "r.h.s." in the left panel is the sum of all the components of the density equation.

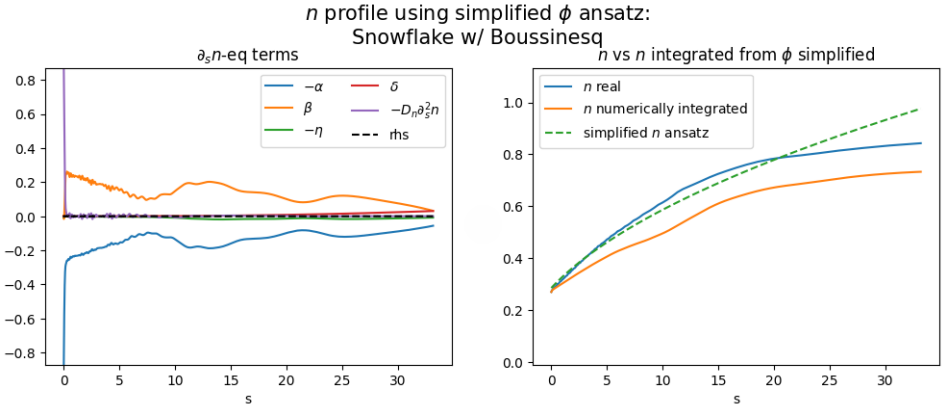

Figure 5.7: Simplified n profile: error estimation
The ϕ profiles obtained for the power-law density case, $n(s) \simeq (as + b)^{\omega}$, were substituted into the corresponding terms for the density equation, integrating for n. The resulting approximation for the case $\omega = 1/2$ has been compared against the real profile.

As the spurious parallel diffusion coefficient is quite small compared to the others, the presence of the $1/D_{\parallel,n}$ factor in the integration scheme could lead to numerical instabilities as it would make the r.h.s. of system (5.10) large. One solution could be to neglect the term, rewriting the system into a 1^{st} order equation and integrating it directly, that is using:

$$\begin{aligned} -\alpha(s)\partial_s n + \beta(s)n + \delta(s)n^2 - \eta(s)n\partial_s n = 0 \\ \Rightarrow \partial_s n = \frac{\beta(s)n + \delta(s)n^2}{\alpha(s) + \eta(s)n} \end{aligned} \tag{5.11}$$

and evolving the terms correspondingly (Fig. 5.8).

The reduced model shows more stability in some cases, as is expected since those correspond to small values of the spurious diffusion coefficient (see Table 1).

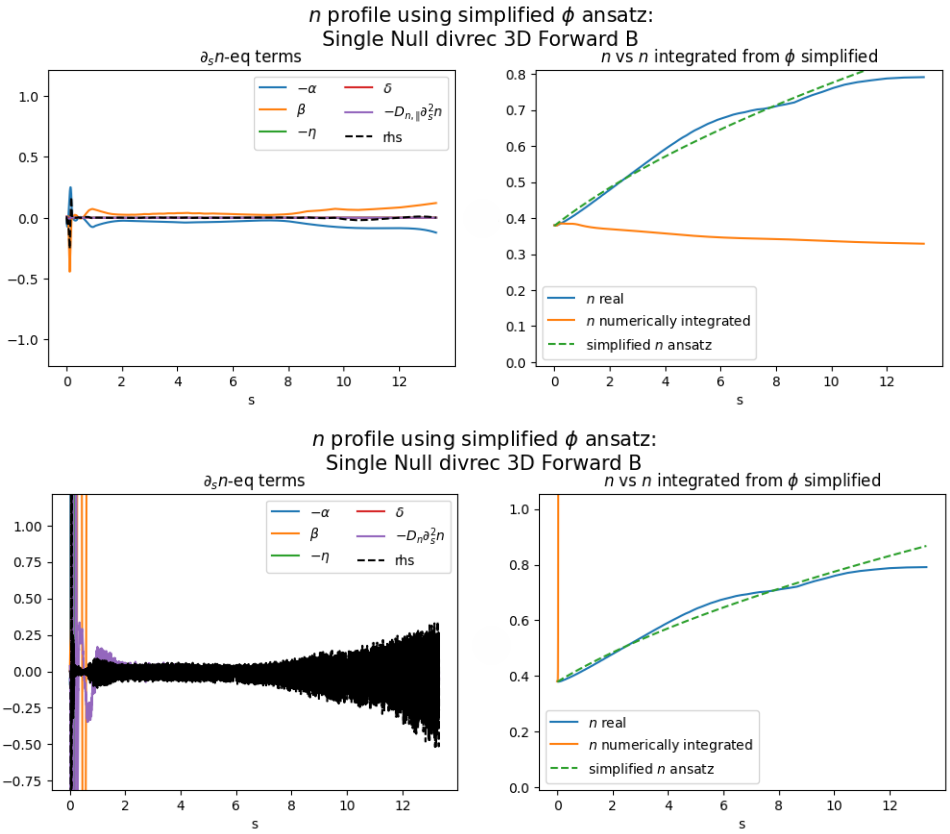

Figure 5.8: Simplified n profile: error estimation
The top panel shows how the ϕ profiles obtained for the power-law density case, $n(s) \simeq (as+b)^{\omega}$, were substituted into the corresponding terms for the reduced density equation (5.11), integrating for n. The resulting approximation for the case $\omega = 1/2$ has been compared against the real profile. The bottom panel shows the corresponding case for the full density equation, which is unstable.

5.3.2 Numerical integration scheme for the full density-potential system

One could then proceed to consider the full density-potential system. The numerical integration scheme is defined in the following way:

At each step $s_k = \sum_{i=1}^{k} h_i$:

1. update n_k using the system (5.10), where the r.h.s is computed using the potential ϕ_{k-1} and its parallel gradient $\partial_s \phi_{k-1}$ at the previous step and employing the RK45 scheme;

2. update ϕ_k using the obtained expression for n_k and numerically evaluating the integral term in (5.3).

In particular a composite trapezoidal rule will be employed for the integral in the r.h.s. of (5.3), $\tilde{I}_{C(p)} := \int_{leg} \left[\frac{\text{sign}(B_0)}{|B_{pol}|} \left(-\frac{n^2 \cos\theta}{\lambda_p} + 2 \sin\theta n \partial_s n \right) \right] ds$. It will allow to iteratively update its value at each step based on the previous time, instead of having to evaluate it at each time step, making the code more efficient. That is, at each step $s_k = \sum_{i=1}^{k} h_i$:

$$\tilde{I}_{C(p),k} \simeq \tilde{I}_{C(p),k-1} + \frac{(A_k + A_{k-1}) h_{k-1}}{2}$$

where $A_k = \frac{\text{sign}(B_0)}{|B_{pol}|_k} \left(-\frac{n_k^2 \cos\theta_k}{\lambda_{p,k}} + 2 \sin\theta_k n_k \partial_s n_k \right)$ is the argument of the integral at each step. Storing the values of the integral at each step one greatly reduces the computational time. Analogous considerations can be made for the second integral $I_{C(p),k}$ in the equation for ϕ_k. Additionally, a constant step size $h = 1e-4$ was considered, as it would allow to pre-compute the coefficients of interest instead of evaluating the contributions at each step. Some examples of the results are shown in Fig. 5.9.

The resulting profiles are subject to error propagation, as can be seen from the figures: this could be due to the integration error in the ϕ equation, which then propagates into the density equation step and so on. The scheme could be further improved in future works by considering either an adaptive step size (at the cost of a slower algorithm as pre-computed factors could not be employed) or more robust scheme for the numerical evaluation of the double integral in the second equation.

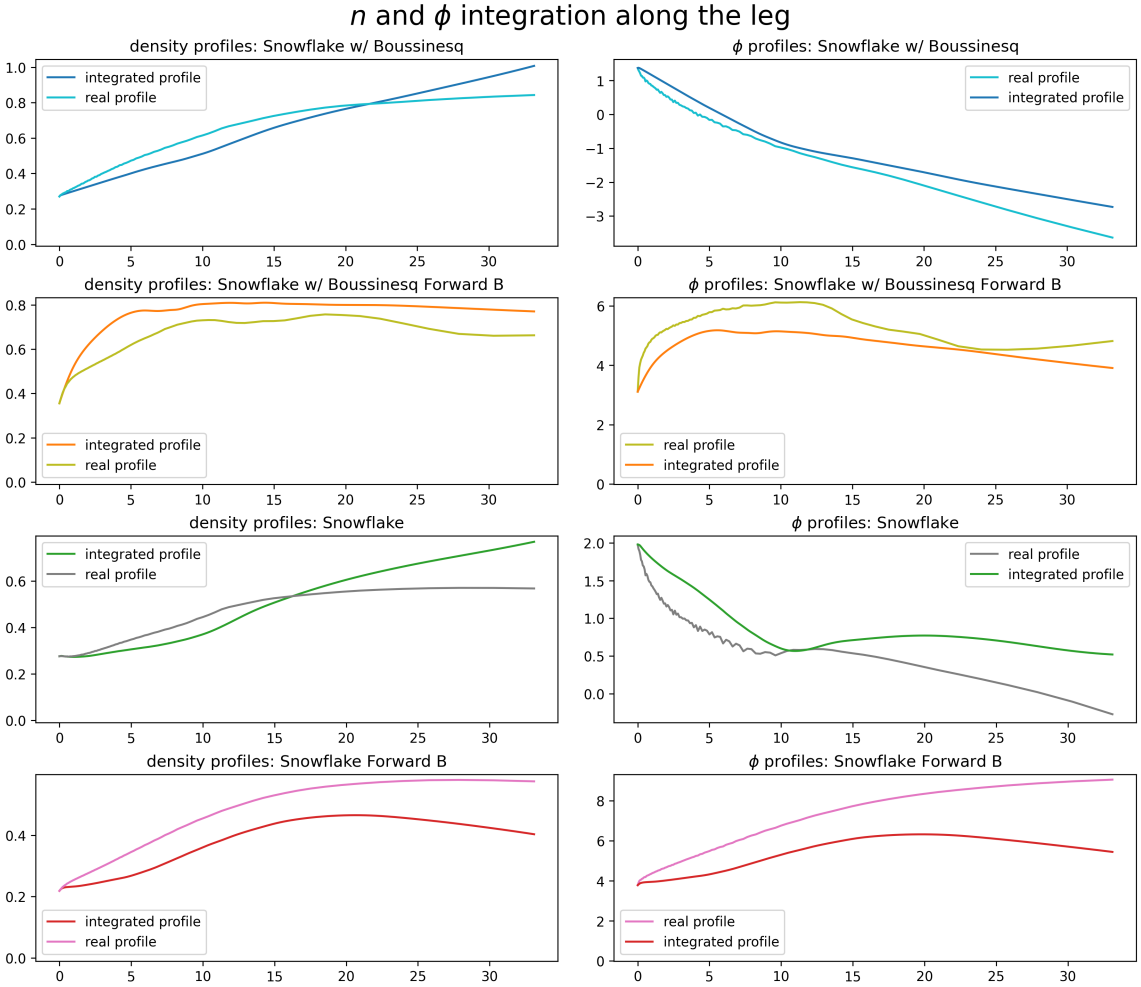

Figure 5.9: Numerical integration scheme for the full ϕ, n system
The ϕ-n system has been numerically integrated using the scheme described above and the results have been compared against the real profiles. The pitch angle θ profile has been extrapolated from the data. The x-labels are omitted due to spatial constraints.

Conclusions

The present analysis aims to find a description of the electric potential structure around the X-point in a tokamak in terms of the smallest number of fundamental observables of our system.

The starting point was a model obtained by [20] to describe the potential along the divertor leg. The resulting scaling law was obtained by applying some simplifying assumptions:

- simplified geometry (straight divertor leg);
- constant gradients along the integration path (divertor leg), so that all the profiles of interest are linear;
- constant flux expansion (broadening of the distance between adjacent flux surfaces) along the leg.

Additionally, the model was compared to simulation data obtained using a code, SOLPS-ITER, which works in regimes in which the drift effects were a lot less pronounced than in the code taken in exam in our case, and involved quantities both measured at the target and at the X-point.

Our work focused on expanding on this previous result. Using the drift-reduced Braginskii equations as a theoretical starting point and employing GBS simulation data as validation, the analysis was articulated in many steps. The first one was to find an equation to describe its profile along the outer divertor leg, the generalised Ohm's law, which was verified against simulation data and analysed in its different components. In particular a closure was found for the first of its components, associated to the parallel current, so as to recover an equation for the potential which only involved two fundamental fields, electron temperature and density, with the corresponding derivatives. The new variables of interest were then analysed and a simplified model was recovered to describe their profiles along the outer divertor leg, which in particular revealed a scaling relation between the electron temperature and density profiles. This approach entailed the approximation of the perpendicular dynamics through the definition of perpendicular length scales, which would relate perpendicular gradients to the quantities measured along the leg. Thus, an equation was obtained describing the evolution of the required fields along the leg. Finally the approximations recovered were substituted back into the original law, obtaining a coupled system of equations in the density and the electric potential. This final system was then analysed in specific regimes, where in particular some approximations where introduced for the density profile: a simple linear profile was considered at first, which allowed a direct comparison with the results in [20] as a scaling law was recovered which could be directly compared to the one obtained in the aformentioned paper; later, a more general power-law profile was considered, and a scaling law was recovered using the same approximations. The advantages that these last scaling laws presented in comparison to the previous result were numerous:

- although simplified geometries were taken in consideration, as a straight leg was assumed (as in [20]), the main features of the magnetic geometry were captured by the definition of the parallel coordinate itself, allowing to differentiate implicitly between the single null and snowflake cases;
- similarly, the effect of flux expansion was captured both by the definition of the parallel coordinate and of the characteristic perpendicular lengths;

- additionally, although in an approximated way, drift effects were taken into consideration, more than in the original result;
- lastly, the required conditions for the 1D model involved quantities measured at the target, which would be easier to obtain experimentally (or to set theoretically from the sheath boundary conditions).

Finally, numerical integration schemes were proposed, both to recover estimates for the error in the case of simplified density profiles and to integrate the full density-potential system. These last results leave room for further improvement: the first, as it could be used to defined iterative fixed-point schemes starting from simplified profiles and converging to the real ones; the second, as the current numerical integration scheme presents some numerical instabilities which could be later resolved by either employing adaptive schemes or more robust integration routines.

The road to controlled fusion is paved with many problems to be resolved, but just as many interesting solutions to each of them. Taming the power of the stars requires a lot of effort and imagination: the only way forward is to consider our contributions, however small they might be, as a function of the bigger picture, and keep hoping that one day our collective effort will bear its fruits. That is how humanity progresses, after all.

Appendix A: Tables and constants

The constants recovered in the scaling law in Chapter 5 (§5.2, Eq. 5.7) are:

$$
\begin{aligned}
c_4 &= -\operatorname{sign}(B_0)\frac{a\cos\theta}{14 d_{pe}} \\
c_3 &= -\operatorname{sign}(B_0)\frac{1}{210a^3}\left(-24a^3Ab - 28a^4B + 56a^3An_t\right) \\
c_2 &= -\operatorname{sign}(B_0)\frac{1}{210a^3}\left(48a^2Ab^2 + 56a^3bB - 112a^2Abn_t - 70a^3Bn_t + 70a^2An_t^2\right) \\
c_1 &= -\operatorname{sign}(B_0)\frac{1}{210a^3}\left(-192aAb^3 - 224a^2b^2B + 448aAb^2n_t + 280a^2bBn_t - 280aAbn_t^2\right) \\
c_{1/2} &= -\operatorname{sign}(B_0)\frac{1}{210a^3}\left(384Ab^{7/2} + 448ab^{5/2}B - 896Ab^{5/2}n_t - 560ab^{3/2}Bn_t + 560Ab^{3/2}n_t^2\right) \\
c_0 &= -\operatorname{sign}(B_0)\frac{1}{210a^3}\left(-384Ab^4 - 448ab^3B + 896Ab^3n_t + 560ab^2Bn_t - 560Ab^2n_t^2\right)
\end{aligned}
$$

where in the above equations one defines the following constants:

$$
\begin{aligned}
b &= n_t + T_0 \\
A &= \frac{\cos\theta}{d_{pe}} \\
B &= \frac{2\sin\theta}{B_t}
\end{aligned}
$$

simulation (labels)	**dimensions**	**Boussinesq approx.**	**simulation time** (t.u.)	**electron temperature cond.** ($\chi_{0,e}$)	**parallel density diff.** ($D_{n,\parallel}$)	**perp. temperature diff.** ($D_{Te,\perp}$)	**perp. density diff.** ($D_{n,\perp}$)
Snowflakes							
Snowflake with Bsq	3D	yes	158.7	1.0	1.0	12.0	12.0
Snowflake with Bsq Fw B	3D	yes	115.1	4.0	4.0	16.0	16.0
Snowflake	3D	no	94.9	2.0	2.0	16.0	16.0
Snowflake Fw B	3D	no	128.9	2.0	2.0	16.0	16.0
Snowflake 2D	2D	no	106.5	1.0	1.0	60.0	60.0
Snowflake 2D Fw B	2D	no	103.4	1.0	1.0	60.0	60.0
Snowflake Reloaded	3D	no	0.43	0.27	0.01	24.0	24.0
Snowflake Reloaded Fw B	3D	no	0.40	0.27	0.01	12.0	12.0
Single Nulls							
Single Null	3D	no	188.7	1.0	1.0	12.0	12.0
Single Null 2D	2D	no	233.4	1.0	1.0	60.0	60.0
Single Null 2D Fw B	2D	no	206.6	1.0	1.0	60.0	60.0
Single Nulls (Divrec)							
Single Null Divrec	2D	no	128.8	1.0	1.0	60.0	60.0
Single Null Divrec Fw B	2D	no	136.2	1.0	1.0	60.0	60.0
Single Null Divrec η_0	2D	no	95.2	13.55	0.01	60.0	60.0
Single Null Divrec η_0 Fw B	2D	no	91.6	13.55	0.01	60.0	60.0
Single Null Divrec with Bsq	2D	yes	55.3	1.0	1.0	60.0	60.0
Single Null Divrec with Bsq Fw B	2D	yes	57.3	1.0	1.0	60.0	60.0
Single Null Divrec 3D	3D	no	2.89	0.27	0.01	12.0	12.0
Single Null Divrec 3D Fw B	3D	no	2.39	0.27	0.01	12.0	12.0

Table 1: Simulation Parameters

Acknowledgements

I want to start by thanking my supervisors, without whom this thesis would have never been able to come to light: prof. Ricci, who decided to take a leap of faith with a foreign student and gave me the amazing opportunity to work in such a prestigious institution on a fascinating subject, and prof. Porcelli, who helped me actualise the project from within Politecnico. Thank you for believing in me.

I would like to thank my day-to-day supervisor, Louis, for all the immense help and patience he showed me in our months working together. Thank you for answering all of my questions and doubts. A special thank you also goes to Brenno and Davide, for helping me out during the very last month, allowing me to give my results a readable form.

A heartfelt thank you goes to the whole SPC team, for making me feel welcome even as an outsider: thank you for the warmth and for the memories, you opened my eyes to a whole new world, which I dream of being part of.

I would like to thank my family, who supported me through the arduous path I chose for myself: thank you for giving me the means and the support to pursue my dreams. I got my stubbornness from my grandparents and the hunger from my parents, and I could not be prouder of it. We are the proof that family can be chosen, and I stand by mine everyday: thank you for standing by yours. Thank you to my little sister, for teaching me how to be patient: I will try to make my studies less obscure and more understandable, just for you. A special thank you goes to my partner, Jafar, for supporting me through these hard years of university: thank you for believing in me, even when I doubted myself. Thank you for dreaming with me.

Finally, but not by order of importance, I would like to thank all of the friends I have met during this incredible journey: my high-school friends, for remaining by my side and growing together with me in spite of pursuing different paths in life; my friends at Politecnico, for enduring these hard years together, for reminding me to let loose every now and then; my friends at Collegio Carlo Alberto, for making the workload more bearable; the friends I met in Lausanne during both exchanges, who made it feel like a second home. Thank you for making all these years and these tears worth it.

Bibliography

[1] Encylcopaedia Britannica. *Nuclear binding energies*. 2012.

[2] Gorno. "Experimental study and interpretative modelling of the Power Exhaust in Configurations with Multiple X-Points in TCV". PhD thesis. EPFL, 2024.

[3] Chen. *Introduction to Plasma Physics and Controlled Fusion*. Springer, 2016.

[4] Waelbroek Hazeltine. *The framework of plasma physics*. Taylor & Francis, 2018.

[5] Ham et al. "Filamentary plasma eruptions and their control on the route to fusion energy". In: *Nature Reviews Physics* (2020).

[6] Militello. *Plasma Physics: an accessible guide to transport, detachment, and divertor design*. Springer, 2022.

[7] Giacomin et al. "Turbulence and flows in the plasma boundary of snowflake magnetic configurations". In: *Nucl. Fusion* (2020).

[8] Reimerdes et al. "Power distribution in the snowflake divertor in TCV". In: *Plasma Phys. Control. Fusion* (2013).

[9] Giacomin. "Turbulent transport regimes in the tokamak boundary". PhD thesis. EPFL, 2022.

[10] Stangeby. *The Plasma Boundary of Magnetic Fusion Devices*. Taylor & Francis, 2000.

[11] Ryutov. "Geometrical Properties of a "Snow-Flake" Divertor". In: *Physics of Plasmas* (2007).

[12] Ryutov et al. "A snowflake divertor: a possible solution to the power exhaust problem for tokamaks". In: *Plasma Phys. Control. Fusion* (2012).

[13] Reimerdes et al. "TCV experiments towards the development of a plasma exhaust solution". In: *Nucl. Fusion* (2017).

[14] Soukhanovskii et al. "Snowflake divertor configuration studies in national spherical Torus experiment". In: *Physics of Plasmas* (2012).

[15] Soukhanovskii et al. "Developing physics basis for the snowflake divertor in the DIII-D tokamak". In: *Nucl. Fusion* (2018).

[16] Ryutov et al. "The 'churning mode' of plasma convection in the tokamak divertor region". In: *Phys. Scr.* (2014).

[17] Schaffer et al. "$E \times B$ circulation at the tokamak divertor X-point". In: *Physics of Plasmas* (2001).

[18] Wensing et al. "Experimental verification of X-point potential well formation in unfavorable magnetic field direction". In: *Nuclear Materials and Energy* (2020).

[19] Chang et al. "X-point ion orbit physics in scrape-off layer and generation of a localized electrostatic potential perturbation around the X-point". In: *Physics of Plasmas* (2019).

[20] Wensing et al. "X-point potential well formation in diverted tokamaks with unfavorable magnetic field direction". In: *Nucl. fusion* (2020).

[21] Braginskii. “Transport Processes in a Plasma”. In: *Reviews of Plasma Physics* (1965).

[22] Zeiler et al. “Nonlinear reduced Braginskii equations with ion thermal dynamics in toroidal plasma”. In: *Physics of Plasmas* (1997).

[23] Zeiler. “Tokamak Edge Turbolence”. In: *IPP-Report* (1999).

[24] Giacomin et al. “The GBS code for the self-consistent simulation of plasma turbulence and kinetic neutral dynamics in the tokamak boundary”. In: *Journal of Computational Physics* (2022).

[25] Ricci et al. “High- and Low-Confinement Modes in Simple Magnetized Toroidal Plasmas”. In: *Phys. Rev. Lett.* (2008).

[26] Ricci et al. “Simulation of plasma turbulence in scrape-off layer conditions: the GBS code, simulation results and code validation”. In: *Plasma Phys. Control. Fusion* (2012).

[27] Halpern et al. “The GBS code for tokamak scrape-off layer simulations”. In: *Journal of Computational Physics* (2016).

[28] Paruta et al. “Simulation of plasma turbulence in the periphery of diverted tokamak by using the GBS code.” In: *Physics of Plasmas* (2018).

[29] Loizu et al. “Boundary conditions for plasma fluid models at the magnetic presheath entrance”. In: *Physics of Plasmas* (2012).

[30] Beadle et al. “Understanding the turbulent mechanisms setting the density decay length in the tokamak scrape-off layer”. In: *Journal of Plasma Physics* (2020).

[31] Giacomin et al. “Investigation of turbulent transport regimes in the tokamak edge by using two-fluid simulations”. In: *Journal of Plasma Physics* (2020).

[32] Wersal et al. “A comparison between a refined two-point model for the limited tokamak SOL and self-consistent plasma turbulence simulations”. In: *Plasma Phys. Control. Fusion* (2017).